PhD 2015

Design and fabrication of nanostructures for enhanced light absorption in silicon

SAGRARIO DOMÍNGUEZ

upna Universidad Pública de Navarra Nafarroako Unibertsitate Publikoa

DESIGN AND FABRICATION OF NANOSTRUCTURES FOR ENHANCED LIGTH ABSORPTION IN SILICON

Thesis for the degree of doctor at the Public University of Navarre

Sagrario Domínguez Fernández

Directors:

Dr. Jesús Pérez-Conde
Department of Physics
Public University of Navarre

Dr. Javier Bravo Larrea
Materials Deposition Area
CEMITEC

Tutor:

Dr. Julián Garrido Segovia
Department of Applied Chemistry
Public University of Navarre

Dr. Jesús Pérez-Conde, Department of Physics, Public University of Navarre.

Dr. Javier Bravo Larrea, Materials Deposition Area of CEMITEC.

Dr. Julian Garrido Segovia, Department of Applied Chemistry, Public University of Navarre.

We certify that the present work has been performed under our supervision in FideNa, CEMITEC and the Public University of Navarre by Sagrario Domínguez Fernández. It constitutes her thesis dissertation to obtain the PhD degree in the doctoral program of *Science and Industrial Technologies* at the *Public University of Navarre*. In compliance with the current legislation; we authorize the presentation of this dissertation signing the present certificate.

Pamplona, May, 2015

Jesús Pérez-Conde Javier Bravo Larrea Julián Garrido Segovia

upna Universidad Pública de Navarra Nafarroako Unibertsitate Publikoa

Recognitions

This work has been supported in part by the Department of Innovation, Enterprise and Employment Government of Navarre research grants IIM13156.RA1, IIQ14598.RI1 and IIB0671109.RS1.

The solar cell integration processes and part of the characterization have been done by the Photovoltaic Solar Energy Department of the National Renewable Energy Centre.

.

Acknowledgements

A todas las personas que han colaborado en esta tesis. A mis directores, Jesús Pérez-Conde y Javier Bravo, por guiarme todos estos años; y a mi tutor, Julián Garrido, por su ayuda en la recta final. A mis compañeros de FideNa y CEMITEC que han aportado más allá de lo científico. Especialmente a Ernesto Bravo por las oportunidades que me ha dado. A mis colegas del departamento de energía solar fotovoltaica de CENER.

To all the people who has participated in this work. To professor George Barbastathis and the 3D Optical Systems group for hosting me in my stay at MIT. To the people of the NSL at MIT. Especially to Tim Savas for his everyday help.

A las personas que, aunque no han participado directamente, han hecho que sea posible. A mis amigos, mis padres, mis hermanos, mis sobrinos y, muy especialmente, a mi marido, Javier.

upna Universidad Pública de Navarra Nafarroako Unibertsitate Publikoa

ABSTRACT

Nanostructures are being widely studied in the scientific community for many different applications because they present novel properties different from those observed in matter at the macroscale. For example, electromagnetic waves interact in an unusual way with periodic nanostructures with sizes in the order of magnitude of the wavelength. Structures with periods in the nanoscale can indeed manage light in the ultraviolet, visible and near infrared regions of the electromagnetic spectrum.

In this work, we use periodic nanostructures to control the optical properties of Si, since it is one of the most common elements in the world and also one of the most used materials in the industry. We focus on the light reflection at Si surface, which is an important limitation in optoelectronic devices nowadays.

This thesis is organized in two different parts. First, we present the optimization and fabrication of periodic nanostructures to maximize light absorption in photovoltaic cells. We have fabricated periodic structures on both polished and unpolished Si substrates, which have been successfully integrated in solar cells following standard industrial processes. In the second part, we explain the fabrication and optical characterization of ultrahigh aspect ratio nanocones for more broadband applications.

The main results presented in this thesis have been also published in the following articles:

1. S. Domínguez et al, "*Optimization of 1D photonic crystals to minimize the reflectance of silicon solar cells*," Photonics Nanostruct. - Fundam. Appl., vol. 10, no. 1, pp. 46–53, Jan. 2012.

2. S. Domínguez et al, "*Design, optimization and fabrication of 2D photonic crystals for solar cells*," Photonics Nanostruct. - Fundam. Appl., vol. 11, no. 1, pp. 29–36, Feb. 2013.

3. S. Dominguez et al, "*Simple fabrication of ultrahigh aspect ratio nanostructures for enhanced antireflectivity*," J. Vac. Sci. Technol. B, vol. 32, no. 3, p. 030602, May 2014.

4. I. Cornago et al, "*Periodic nanostructures on unpolished substrates and their integration in solar cells*," Nanotechnology, vol. 26, no. 9, p. 095301, Mar. 2015.

upna Universidad Pública de Navarra Nafarroako Unibertsitate Publikoa

INDEX

CHAPTER 1. INTRODUCTION

CHAPTER 2. CONTEXT AND OBJECTIVES

CHAPTER 3. MATERIAL AND METHOD

CHAPTER 4. RESULTS AND DISCUSSION

upna Universidad Pública de Navarra Nafarroako Unibertsitate Publikoa

CHAPTER 1. INTRODUCTION

1. INTRODUCTION TO NANOSTRUCTURES

1.1. HISTORICAL BACKGROUND

Nanotechnology is the manipulation of matter with at least one dimension sized from 1 to 100 nanometers [1]. This concept is very broad, and includes very diverse fields of science like chemistry, biology and physics.

The first ever concept of nanotechnology was presented in 1959 by the professor of physics Dr. Richard P. Feynman in his lecture "There is plenty of room at the bottom" given at an American Physical Society meeting at Caltech. In his talk, Feynman considered the possibility of direct manipulation of individual atoms as a more powerful form of synthetic chemistry than those used at the time [2]. Later on, the term "nanotechnology" was introduced by Norio Taniguchi in his talk "*On the Basic Concept of Nano-Technology*" at the International Conference on Industrial Production in Tokyo in 1974 [3] and by Eric Drexler in his book "*Engines of creation: The Coming Era of Nanotechnology"* in 1986 [4].

In the meantime, in the early 1980s, Gerd Binning and Heinrich Rohrer developed the scanning tunneling microscope at the IBM Zurich Research Laboratory. This microscope was the first instrument capable of imaging surfaces at the atomic level. Since then, many tools have been developed to observe matter at the nanoscale and to prove the influence of the arrangement of atoms and molecules at the nanoscale on the properties of matter.

All natural structures are built up from sub-structures in the nano-sized range that determine the properties and functionalities of materials. There are many examples of nanostructured materials present in nature with extraordinary properties such as the

lotus plant leaf, the moth eyes or the wings of butterflies. *Fig.1.1* shows one micrograph for each one of these examples.

The leaf of the lotus plant presents extraordinary wetting properties: a droplet touching its surface, instantly acquires a spherical shape, and even slight tilting causes it to roll off the leaf. Scanning electron microscope (SEM) images of these water-repellent bio-surfaces have revealed large structural diversity, with the common characteristic of roughness at both the micro-scale and the nano-scale (*Fig.1.1*.a) [5]. The eyes of the moth have exceptional broadband low reflectivity for the visible light so they can see much better than humans in dim or dark conditions. This excellent light-absorption is due to the very small pillar arrays on the surface of the moth eyes. The pillars have a hexagonal shape and are a few hundred nanometers tall and apart so they are smaller than the wavelength of light (*Fig.1.1*.b) [6]. In the case of the butterfly wings, their microstructured and nanostructured morphology (*Fig.1.1*.c) cause interference and diffraction of light leading to structural coloration and iridescence instead of the usual pigmentation [7].

Besides, there are a number of relatively famous examples of ancient human-made artefacts using nanocomposites, i.e. bulk materials mixed with nanoparticles to improve its properties, "accidentally". One example is the Lycurgus cup which is a Roman vessel from about AD 400 made from an impressive dichroic glass (*Fig.1.2*.a). The cup shows a different color depending on whether or not light is passing through it; red when lit from behind and green when lit from the front. In the late 1980s, analysis of the glass revealed the presence of diminute particles of silver-gold alloys, typically 50-100 nm in diameter, causing the dichroic effect [8]. Another example is the Maya Blue, which is an ancient blue pigment created by the ancient Maya in AD800 (*Fig.1.2*.b). Despite exposure to acids, alkalis, and chemical solvents, the color of the Maya Blue remains unaltered due to its structure at the nanoscale. The pigment is composed of a nanoporous palygorskite clay filled with indigo dye [9].

Nowadays, there is much research in progress all over the world to obtain new functions and properties of materials by controlling their configuration at the nano-scale. Benefits of nanotechnology are applied to many different fields such as medicine [10], energy [11], food [12], defense [13] and information technologies [14].

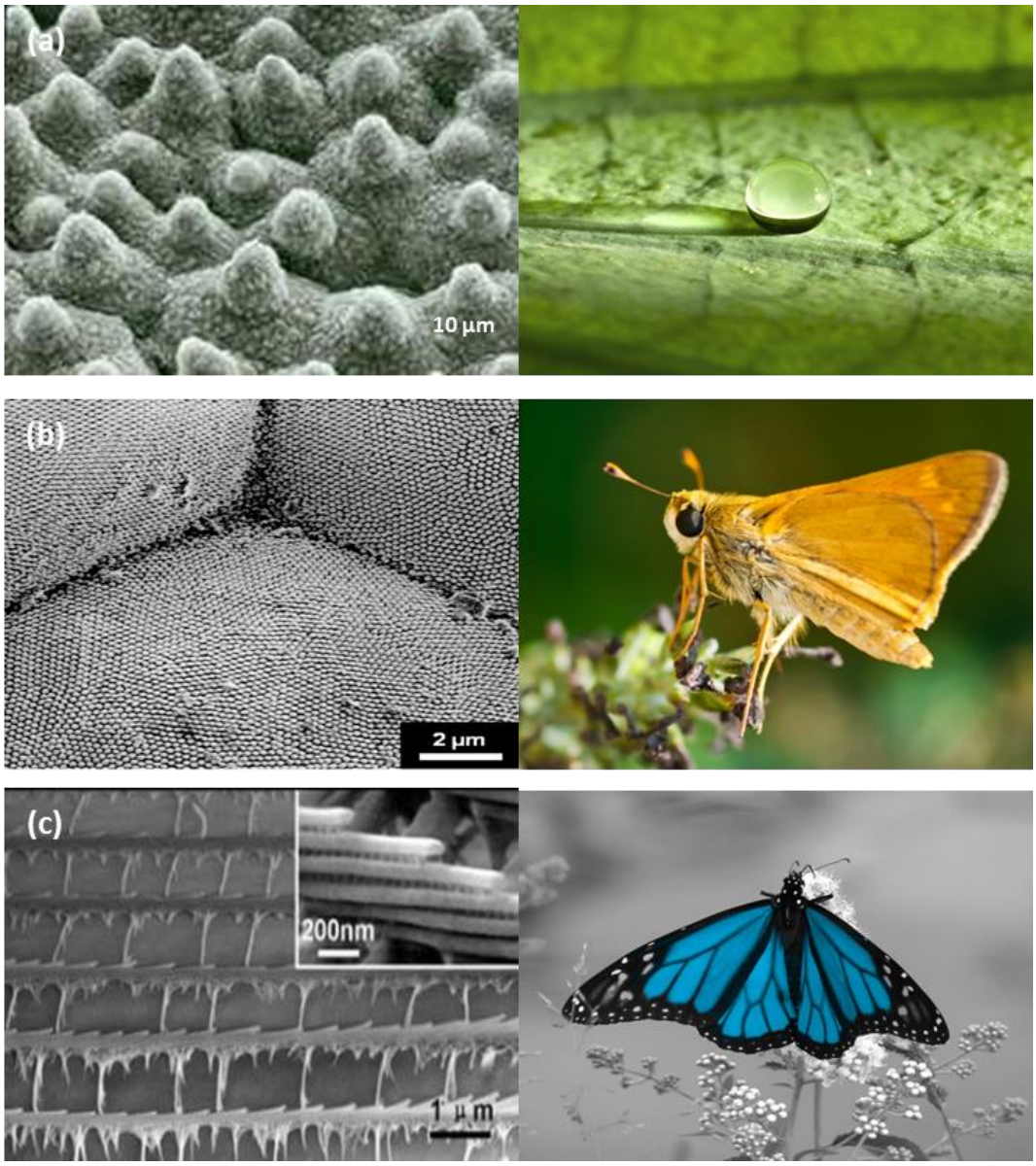

Fig.1.1. SEM micrographs of three examples of nanostructures present in the nature: the lotus leaf obtained from [15] *and* [16] *(a), the moth eyes obtained from*[17] *and* [18]*(b) and the butterfly wings reprinted from* [19] *and* [20]*.*

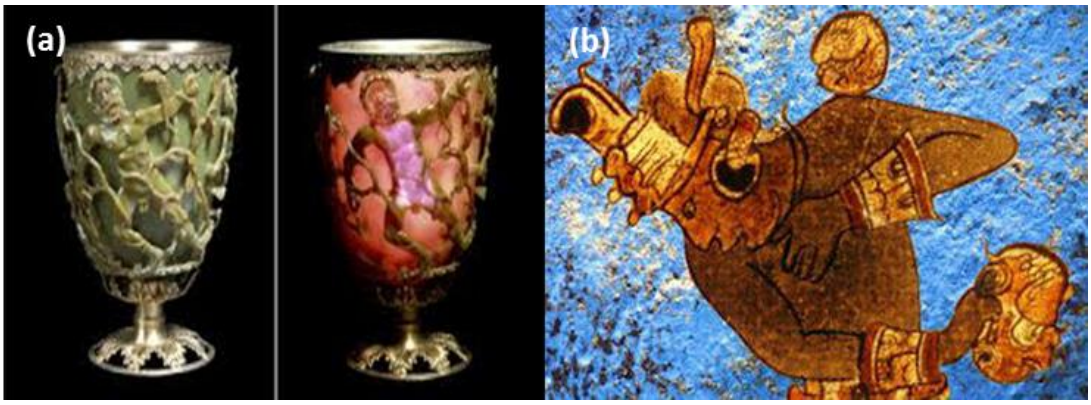

Fig.1.2.Two examples of nanostructured human creations: the Lycurgus cup (a) and the maya blue (b). Images reprinted from [21] *and* [22] *respectively.*

1.2. DEFINITION OF NANOSTRUCTURES IN THIS WORK

In general, a nanostructure can be defined as any structure with one or more dimensions measuring in the nanometer range. There are many different types of nanostructures. One classification could be done attending to the number of dimensions on the nanoscale. For example, quantum dots are considered to be zero-dimensional (0D), wires, rods and tubes one-dimensional (1D), quantum wells two-dimensional (2D) and nanoparticles three-dimensional (3D) [23].

In this work, nanostructures are referred as either periodic or random structures patterned at the surface of a bulk material. At least one dimension of these structures is in the nanoscale. When the nanostructures are periodic, they are also referred in this work as photonic crystals (PCs). These kinds of nanostructures are commonly used in optics and photonics due to their unique capabilities of manage light [24-26].

2. OPTICS AND PHOTONICS

2.1 INTRODUCTION

The electromagnetic (EM) spectrum extends from bellow the high wavelength used for modern radio communication to gamma radiation at the short wavelength and thereby covering wavelengths from thousands of kilometers down to a fraction of the size of an atom.

Optics is the science that studies the nature, properties and applications of light, which normally includes the infrared (IR), visible and ultraviolet (UV) regions of the EM spectrum (see *Table 1.1*).

Classic optics usually uses simplified models to study light. The simplest of these, geometric optics, treats light as a collection of rays that travel in straight lines and bend when they pass through or reflect from surfaces [26]. There are also more complex models like physical optics, which includes wave effects such as diffraction and interference, and quantum optics, which includes both the wave-like and particle-like properties of light [26].

Photonics is an engineering discipline concerning also the control of light or photons in the optical region of the EM spectrum (see *Table 1.1*). While optics often connotes fundamental research, photonics focuses on applied research and development. The term "photonic" emphasizes the fact that, besides the wave nature, light has also particle nature. While the wave nature determines light propagation, only the quantum nature is able to explain phenomena such as the photoelectric effect or the black body radiation [27].

Wave region	**Frequency**	**Wavelength**	**Devices**
Radio	KHz - MHz - GHz	Km - m - cm	Electronic devices
Microwave	1 GHz - 1 THZ	300 mm - 300 µm	Microwave devices
Optical	1 THz - 10 PHz	300 µm - 30 nm	Photonic devices
Infrared	1 THz-430 THz	300 µm - 700 nm	
Visible	430 THz - 750 THz	700 nm - 400 nm	
Ultraviolet	750 THz - 10 PHz	400 nm - 30 nm	
X-ray	10 PHz - 10 EHz	30 nm - 300 pm	
Gamma ray	10 EHZ and above	300 pm and shorter	

Table 1.1. Electromagnetic spectrum.

Interaction between light and mater is an important issue of study in both optics and photonics. This interaction becomes particularly interesting in the case of nanostructured materials since they have building blocks in the same scale as the wavelength of light and they can affect the direction, polarization or wavelength of its propagation controlling important phenomena such as reflection, refraction, transmission and absorption [25,29].

Interaction between light and nanostructures has been widely studied during the last decades due to its direct application fields like optic communications and photovoltaic (PV) [29]. In communications, the next-step change is to introduce photonics into on-chip devices, which requires miniaturized optical sources, circuits and detectors to encode and transmit data around the chip [31,32].

In the case of PV, efficient photon management schemes are crucial for improving the energy conversion efficiency of devices. The reduction of light reflection at the interface of solar cells is particularly interesting: the more photons absorbed the more energy will be obtained from the cell.

2.2 ANTI-REFLECTION THEORY

Refraction is the change in direction of an incident wave at an interface between two different media due to the change in refractive index (n). That change in direction is given by Snell's law:

$$n_1 \cdot sin\theta_i = n_2 \cdot sin\theta_r \quad (1.1)$$

where n_1 and n_2 and are the n of the two media, θ_i the angle of incidence and θ_r the angle of reflection.

Reflection is a particular case of refraction in which the wave returns into the medium from which it was originated. Both, refraction and refelction are schematically represented in *Fig.1.3*.

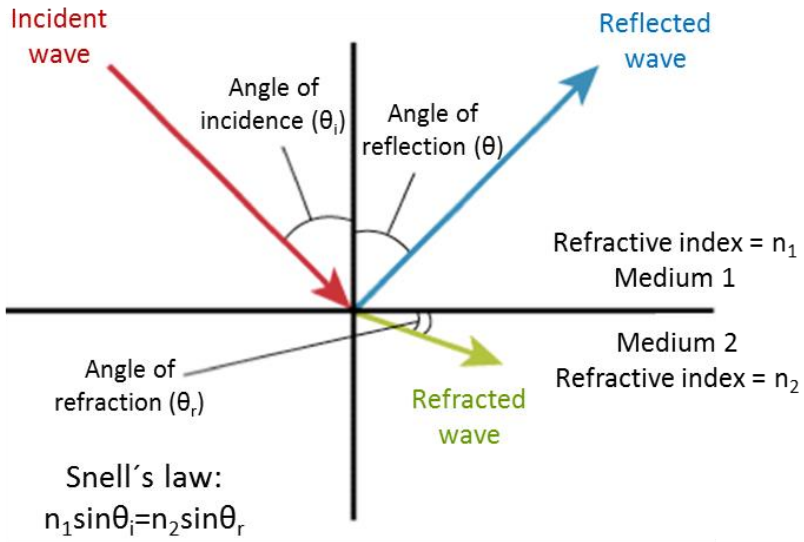

Fig.1.3. Representation of refraction and reflection at the interface of two media with different refractive index.

There are many applications such as lenses, displays or solar cells; where light passes through an interface, and no loss or reflection is desired. For this reason, much research has been done to find the perfect antireflection mechanism. This section summarizes some important approaches and theories used in the last decades.

2.2.1 Anti-reflective coatings

Historically, the first solutions considered to reduce the light reflection at an interface were based on antireflective coatings (ARCs) made from a material with an intermediate n between air (n=1) and the substrate.

The basic principle of an ARC can be explained with the wave optics. The idea is to reduce the reflection at an interface between two media by including an extra media, i.e. ARC, between them with an intermediate n. This simple scheme is represented in *Fig.1.4.*

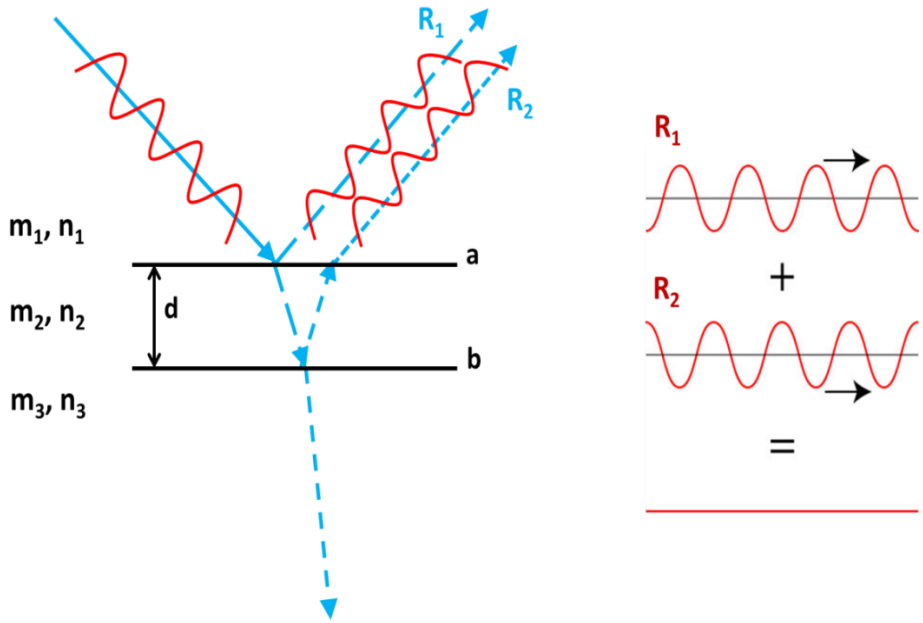

Fig.1.4. Schematic representation of a single layer coating system.

In the figure, a light wave traveling through three different media, m_1 (with $n = n_1$), m_2 (with $n = n_2$) and m_3 (with $n = n_3$) is represented. These three media, are disposed one immediately behind the other and *a* and *b* are the interfaces between $m_1 - m_2$ and $m_2 - m_3$ respectively. When light traveling through m_1 reaches the interface *a*, part of the light is reflected back to m_1 and the rest goes through m_2 to the interface *b*. At this point, again part of the light is reflected back to m_2 and the rest refracted to m_3. The light reflected into m_2, again reaches the interface a so part of this light is again refracted to m_1. Consequently there are two reflected waves in m_1 that interfere either constructively or destructively before they exit the surface *a*. Two requirements must be met for the exact cancellation of the reflected waves [32]:

$$\boldsymbol{n_2 = \sqrt{n_1 \cdot n_3}} \tag{1.2}$$

$$\boldsymbol{d = k \cdot \frac{\lambda}{4 \cdot n_2}} \tag{1.3}$$

where *d* is the thickness of m_2, λ the wavelength of light and *k* and odd integer.

Therefore, with the correct design of this ARC (*d* and *n*), it is possible to totally suppress reflection for a particular wavelength according to the design parameters.

ARC solutions were improved with the use of multiple layers. The idea was to achieve more broadband antireflection results with a sequence of materials having n varying stepwise from the n of the air to the n of the substrate. In 1964 Jacobson first analyzed and fabricated an optical multi-layer film with a gradual variation in n [33] and since then, the popularity of gradient n ARCs grew considerably among the scientists [35-38]. However, the availability of materials to match the design parameters and the instabilities and adhesion problems related to multi-stacks become a problem in these kind of solutions [36].

2.2.2 Sub-wavelength structures

An alternative to multilayer ARCs was to use sub-wavelength structures (SWS) to obtain materials with a gradual variation in n themselves. Different types of SWS have been studied including both periodic and aperiodic distributions. The key is to create a region with an intermediate *n* between the air and the substrate by mixing both materials at the sub-wavelength scale. In this way, the antireflective (AR) behavior is not restricted to a particular λ and broader band of matching is obtained. Different theories have been developed to analyze these kinds of structures for their use in different fields. Two of these theories are particularly interesting for light management: the diffraction grating theory and the effective medium theory (EMT).

2.2.2.1 Diffraction grating theory

A periodic SWS acts as a diffraction grating, splitting the light into several beams traveling in different directions named diffracted orders. However, if AR behavior is desired, diffraction should be avoided. The diffraction grating theory analyzes diffraction of light in periodic structures and is useful in the design of AR SWS to avoid diffractive losses.

The direction of the diffracted orders depends on the spacing of the grating and the light wavelength. The basic surface-relief grating diffraction geometry is shown in *Fig.1.5*. Grooves are periodically spaced in the x direction with period *p*, width *w* and height *h*.

As represented in *Fig.1.5*, when an EM plane wave reaches the grating, both forward diffraction and backward diffraction are produced. The angles of diffraction of the forward diffracted waves are given by the grating equation [38]:

$$\boldsymbol{f\lambda = p(sin\theta_i + sin\theta_f)} \tag{1.4}$$

Where f is the diffracted order, λ the free space wavelength, θ_i is the angle of incidence and θ_f is the angle of diffraction in the grating material of the fth - order forward diffracted wave.

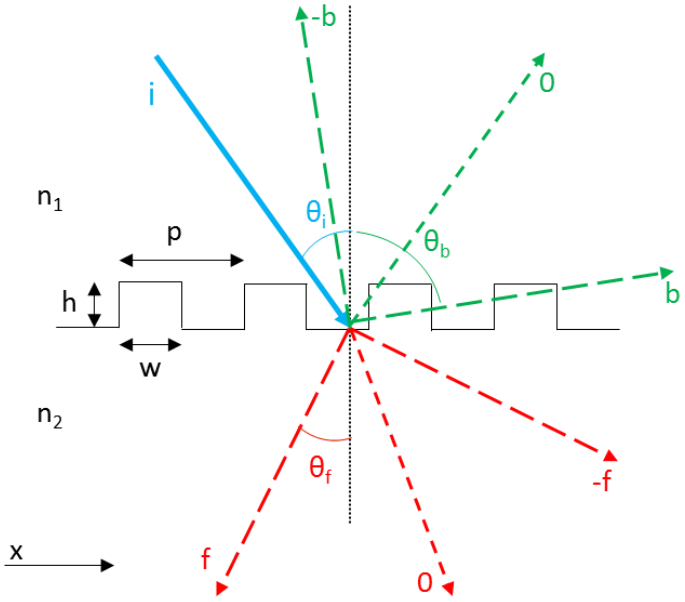

Fig.1.5. Diffraction geometry of a surface-relief grating.

The backward diffracted angles are then given by the corresponding equation:

$$\boldsymbol{b\lambda = p(sin\theta_i + sin\theta_b)} \tag{1.5}$$

Where b is the diffracted order and θ_b the angle of diffraction in the grating material of the bth - order backward diffracted wave.

There are values of p where the above equations do not have solution for non - zero orders of diffraction for any incident angle, which means that only reflection (zero - order diffraction) occurs. For this, there is a condition that must be accomplished [39]:

$$\boldsymbol{p < \lambda/2} \tag{1.6}$$

Once this conditions is satisfied, the design of the parameters of the grating determines the reflection intensity [43,44].

2.2.2.2 Effective medium theory

The EMT explains the AR behavior of SWS. It describes the interaction of light with SWS considering such SWS as a homogenous medium with an effective n (n_{eff}) that depends on the n and volume fill factors of the bulk materials involved. EMT is only valid for textures with motifs much smaller than the wavelength of light. Larger feature sizes require modeling of high order diffractions and cannot be considered as effective media [42].

In the case of light traveling through the interface between air ($n = n_0$) and a particular substrate ($n = n_s$) with SWS on top, the EMT defines an effective medium with a n that varies from the n of air to the n of the substrate. The optical properties of this effective medium depend on the specific profile geometry of the SWS. *Fig.1.6* shows the schematic of two different SWS and the n_{eff} variation along the propagation direction.

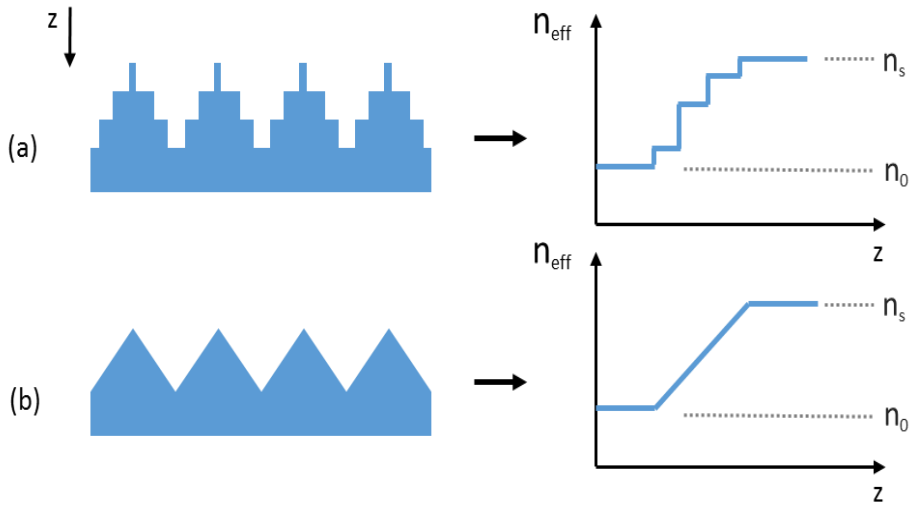

Fig.1.6. Schematic of two graded index SWS and their corresponding n_{eff} variation along light propagation.

The n_{eff} is calculated as the weighted spatial average index of refraction in the light propagation direction. For the case of multilevel SWS (*Fig.1.6*.a), the effective medium is equivalent to a film stack where each layer corresponds to a distinct level of the profile. The n_{eff} in this case increases layer by layer from the n of the air to the n of the substrate ($n_0<n_1<n_2<n_3<n_s$). For a continuous profile (*Fig.1.6*. b), the equivalent effective medium is a gradient film and the n_{eff} increases along the light propagation direction, *z* ($n_0<n(z)<n_s$).

Many different models have been used to calculate the n_{eff} of different SWS. To achieve perfect AR at the interface between air and a particular substrate, very exceptional profile structures, known as the kopflestein structures have been theoretically demonstrated [46,47]. These structures have a specific fifth-order polynomial dependence on depth [45] which create an optimum graded n_{eff} profile for reflection reduction.

Two examples of kopflestein structures are presented in *Fig.1.7*. These structures are perfect AR theoretical designs but it is very complicated to experimentally obtain such profiles. As more feasible approximations, different smoothly tapered profiles with graded n_{eff} have been fabricated obtaining almost perfect antireflection in some cases [39,49,50].

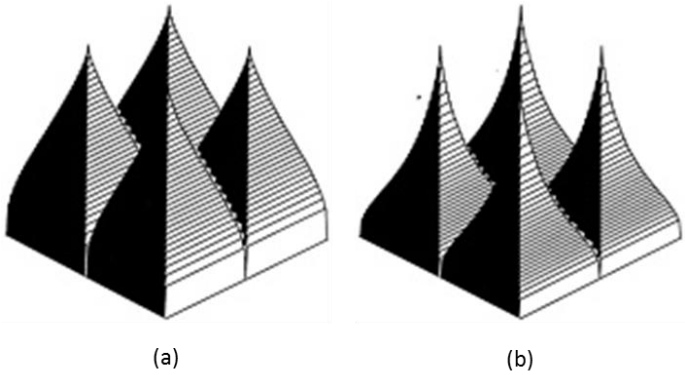

Fig.1.7.Kopflestein structures for two different substrates: one with n = 1.45 (a) and other with n = 3.42 (b).Reprinted form [43].

2.2.3 Graded index sub-wavelength structures

The first graded index SWS were first discovered in nature while inspecting the eyes of the night flying moths by Bernhard in 1967 [48]. Since then, scientists have successfully reproduced the moth eye structures with lithographic techniques [39,40,52]. The basic principle of moth eye structure is that the outer surface is covered with a regular array of conical protuberances, typically of sub-micron height and spacing in the order of 200 nm. Two examples of moth eye surfaces fabricated by scientists are shown in *Fig.1.8*.a. In the moth eye structure, the n_{eff} of the surface layer varies gradually form air to substrate, and suppresses the specular reflectance at the interface of the two media.

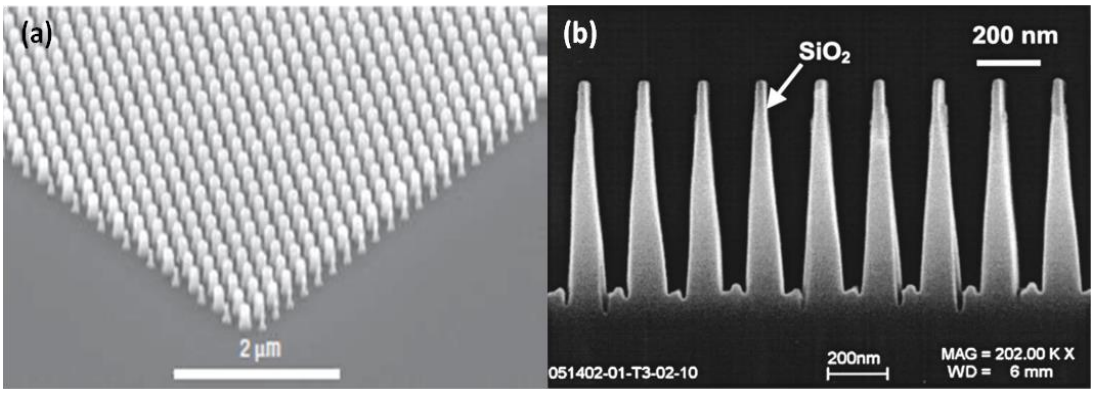

Fig.1.8.Two examples of graded-index SWS: Moth eye structure fabricated in [50] *(a) and nanocone structure fabricated in* [51] *(b).*

Today, numerous scientists are still trying to reproduce the moth eye structure [45,55] and also other graded index SWS to create the ideal AR surface [56-59]. The most popular geometry is the nanocone which is inspired in the moth eyes SWS and is easier to fabricate compared to the kopflestein structures. Periodic nanocones have shown impressive broadband and omnidirectional AR properties for different materials, such as glass and silicon (Si) [60,61]. *Fig.1.8*.b shows an image of nanocones fabricated in the recent years and *Fig.1.9* a diagram of the structure geometry.

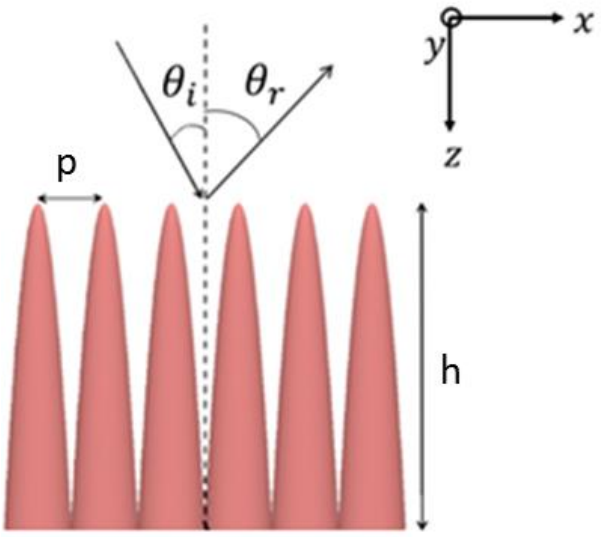

Fig.1.9. Diagram of nanocone structure and incident light geometry.

In *Fig.1.9* light reaches the nanocones with an incident angle θ_i and part of it is reflected at an angle θ_r. In this situation, the optical response of the nanocones is similar to an optical bandpass filter, where the long cutoff wavelength λ_{max} is determined by the structure height h and the short cutoff wavelength λ_{min} by the

structure period p [62,63]. In particular, the long and shot cutoff wavelengths can be approximated as [57]:

$$\lambda_{max} \sim 2hn_a cos\theta_i \quad (1.7)$$

$$\lambda_{min} \sim p(n_s + n_a \sin\theta_i) \quad (1.8)$$

where n_a is the n of the medium, typically air; and n_s the n of the substrate.

According to equations (1.7) and (1.8), the long cutoff wavelength increases with the height of the nanocones and the short cutoff wavelength decreases with the period of the structure. Besides, if the incident angle increases, the maximum wavelength decreases and the minimum wavelength increases.

Therefore, for any fixed incident angle, to yield a wider broadband response, the height of the nanocones needs to be maximized and the period minimized. For this reason, fabricating tapered nanostructures with high aspect-ratio, i.e. the ratio of nanocone height to the period, has become a challenge for many applications. Part of this work deals with this issue: developing a fabrication process for high aspect-ratio nanocones to achieve broadband antireflection.

However, the main application of this work is the PV field, where such high aspect ratio nanostructures are not always necessaries. In the case of Si based solar cells, the wavelength band of operation is defined by the properties of the Si and the AR behavior of the nanostructures can be limited to that range. In this case, the nanostructures geometries and dimensions have been specifically optimized for this particular application.

3. THEORY OF SOLAR CELLS

3.1. INTRODUCTION

A solar cell is an electrical device that converts the radiation coming from the sun into electricity by the PV effect [60]. Light shining on the solar cell produces both current and voltage to generate electric power. A variety of materials and processes can potentially satisfy the requirements for this conversion, but nowadays, practically all

the PV devices use semiconductor materials in form of a p-n junction. Moreover, more than the 80% of these devices are based in Si p-n junctions.

This work is also focused on bulk p-n junction Si solar cells. The basic structure is represented in *Fig.1.10*. It consists on a p-n junction, both back and top metallic contacts to collect the generated current and an AR top surface to maximize the absorption of solar radiation. From now on, the term "solar cell" in this work will refer to this type of device.

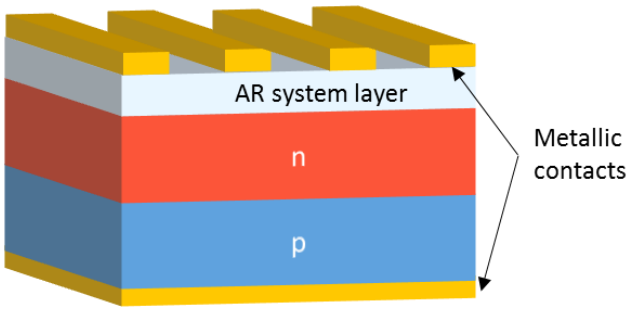

Fig.1.10.Basic structure of a conventional solar cell.

3.2. SUNLIGHT RADIATION

The sun emits electromagnetic radiation from 200 to 2500 nm covering therefore most of the UV, the visible and part of the IR. The irradiation distribution along this wavelength range is shown in *Fig.1.11* for both the outside atmosphere and the sea level.

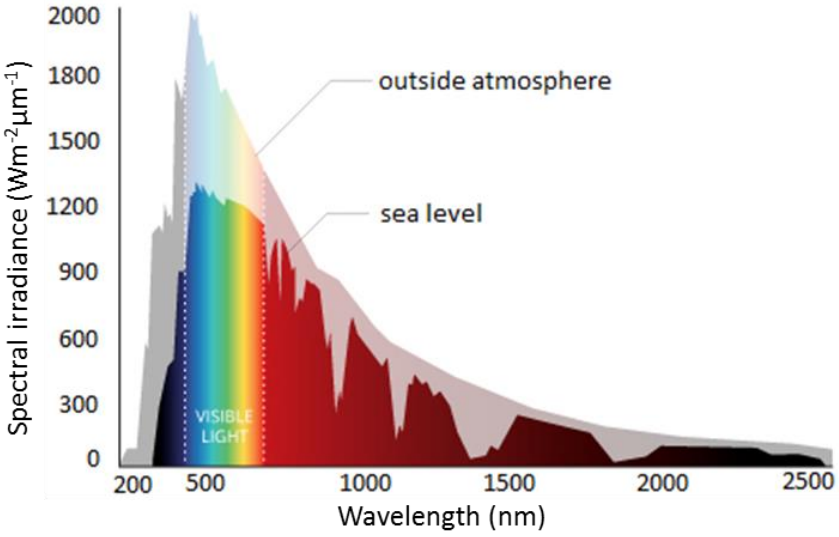

Fig.1.11. Spectral distribution of sun radiation obtained from[61].

The most energetic regions of the sun radiation spectrum are the visible and the near IR, i.e. between 300 and 1000 nm.

The energy of a photon directly depends on its wavelength according to the equation:

$$E = \frac{hc}{\lambda} \tag{1.9}$$

Where *h* is Planck´s constant and *c* is the speed of light. Therefore, the spectrum of sun radiation determines the energy of its photons.

Sun photons have energies between 0.5 eV (2500 nm) and 6.2 eV (200 nm). For example, the red light has around 1.8 eV (690 nm) and the blue light close to 3.1 eV (400 nm). Efficient materials for light into electricity conversion need to have a band gap with lower energy (higher wavelength) than these values to absorb the most efficient spectral bands. Typical band gaps range from 1 to 1.6 eV (1200 and 775 nm). Normally, these efficient materials for PV are from either group IV (e.g. Si or Ge) of the periodic table or from III-V group combination (e.g. GaAs or InP), or of II-VI group combination (e.g. CdTe or CdS).

3.3. MATERIALS

The PV effect requires a material capable of generating both electrical current and voltage directly from light. Generating current requires electron mobility and generating voltage requires a gap between electron energy states. Metals have electron mobility and insulators have gaps between energy states, but only semiconductors have both [62].

Metals, insulators and semiconductors are defined by their unique electric conductive behavior, which is associated with their electronic band structure. The electrons of a single atom occupy atomics orbitals, which form a set of discrete energy levels. If multiple atoms are brought together to form a solid, these energy levels form a global distribution of infinite number of discrete energy bands with band gaps in between. While lower energy bands remain always filled with electrons, higher energy bands are usually empty under ordinary circumstances.

The most relevant bands for electronics and optoelectronics are the valence band and the conduction band. The valence band is the highest energy band filled with electrons

at absolute zero temperature. At this band, electrons are bound to individual atoms. The conduction band is the next energy band in which electrons can move freely within the atomic lattice of the material.

In insulators and semiconductors there is an energy band separating the conduction and the valence bands, called band gap. In contrast, metals have no separation between valence and conduction bands. In insulators, the band gap is large, making it difficult for electrons to jump to the conduction band. In semiconductors, the band gap is small allowing electrons to populate the conduction band. *Fig.1.12* shows an illustration of the electronic band structure of these three different materials.

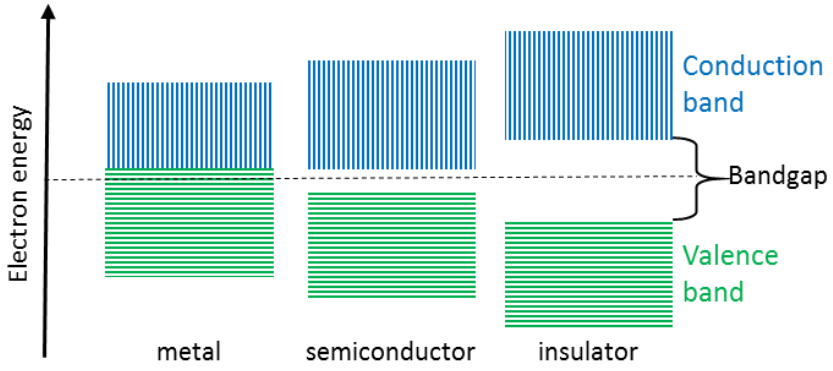

Fig.1.12. Schematic illustration of the band structure of a metal, a semiconductor and an insulator.

The band gap of a semiconductor can be of two types, a direct band gap or an indirect band gap. The band gap is direct if the momentum of electrons is the same in both the conduction and the valence bands. In this case, it is easy for electrons in the conduction band to fall to the valence band. In contrast, in an indirect band gap, electrons in the conduction band rarely move to the valence band.

When light hits a semiconductor, some photons are absorbed by the material and their energy is given to the electrons in the valence band. The photons energy excites some electrons to the conduction band where they are free to move around within the semiconductor. These electrons can be collected in an external circuit generating an electrical current. Each excited electron leaves a hole in the valence band, which is considered as a positive particle. The holes form also a current opposed to the electronic flux. This generation of electron-hole pairs requires that the energy of the absorbed photons is greater than the band gap of the material.

However, not every semiconductor with an appropriate band gap is capable of convert efficiently sun radiation into electricity. Efficient materials for solar cells need also to have a spectral response according to the solar irradiance spectrum. Fig.1.13 shows the spectral response of four typical materials used in solar cells (c-Si, a-Si, GaAsAl and GaAs) compared to the response of the human eye and the sunlight radiation spectrum. While the responses of the a-Si and the human eye are limited to the visible region of the spectrum, the responses of the c-Si, GaAsAl and GaAs reach also part of the near IR. The band gaps of Si, GaAs and GaAsAl are also represented below the graph. The higher the wavelength of the band gap, the lower its energy and therefore, the more photons can be absorbed.

All the materials represented in *Fig.1.13* have band gaps and spectral responses appropriate for the PV conversion. However, there is not a clear optimum: while the wavelength of the Si band gap is the highest of the three materials, the spectral response of the GaAsAl matches better with the spectral distribution of sun radiation. Each semiconductor has a particular spectral response and a band gap, which limits its capabilities for the PV conversion and prevents solar cells to reach 100 % efficiency.

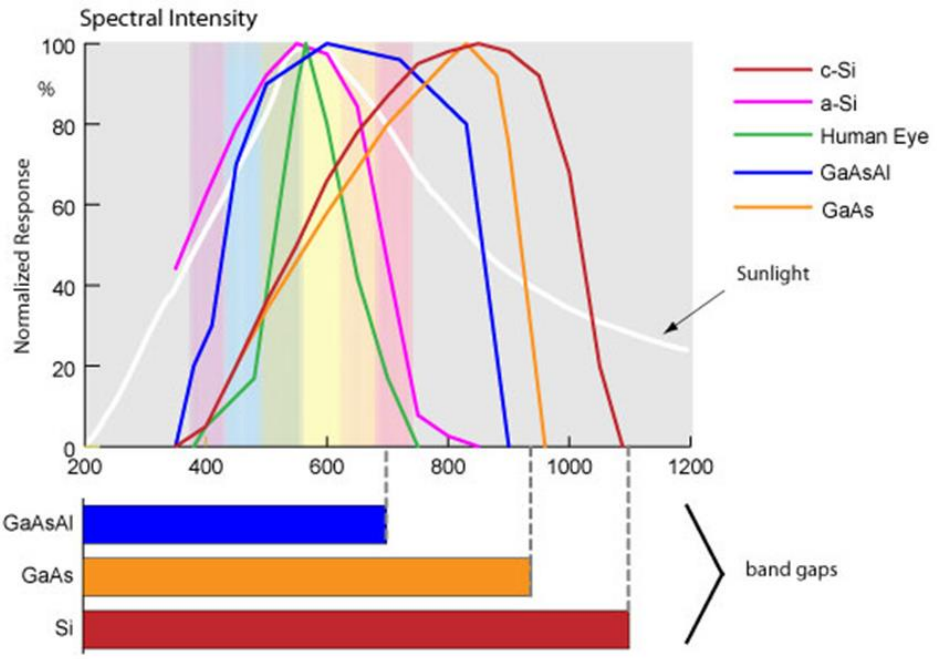

Fig.1.13. Spectral response of amorphous silicon (a-Si), crystalline Si (c-Si), human eye, GaAsAl and GaAs. Reprinted from [63].

Si is one of the most used materials in solar cells due to the desired compatibility between photonic and electronic devices. It has many advantages such as the

availability of large single crystals, high purity and, very importantly, natural abundance. For these reasons, it has been established as the material of choice of the electronic industry which has developed Si technology to its present maturity. Besides, its electronic band structure, with a band gap of 1.1 eV (1150 nm) and its spectral response, from 300 nm to 1150 nm, are optimal for capturing most of the solar spectrum, which makes Si almost ideally suited for PV applications (see *Fig.1.13*). In fact, around 90% of solar panels used today are based on crystalline Si (c-Si) [29].

3.4. SILICON P-N JUNCTION

c-Si consists of Si atoms connected to form a crystal lattice. A single Si atom has four outer electrons available for chemical covalent bonding with other Si atoms. Each bond consists of two electrons, one electron from each of the Si atoms involved in the bond.

A Si p-n junction is an interface between two differently doped Si regions, a p-type region and a n-type region. The n-region is doped with an element with five available bounding electrons, typically phosphorous (P). Each dopant P atom forms four covalent bonds in the same way that a Si atom does with its neighbors. The fifth of the P bonding electrons that is not used in covalent bonding is then only weakly attached to the phosphorus atom so is free to travel around the crystal.

The p-region is doped with an element with three available bounding electrons, typically boron (B). Because a B atom has only three electrons available in its bonding shell, only three covalent bonds can be formed between a boron atom and the Si atoms in a crystal. Therefore, there is an electron vacancy or hole for covalent bounding with the fourth available Si electron.

As a result, the p-type Si has a larger hole concentration and the n-region has larger number of free electrons that can move through the material. When these two regions are joined, there are a large number of mobile electrons at the n-type side but very few on the p-type side so electrons diffuse to the p-type side and holes to the n-type side charging positively the n-type side and negatively the p-type side.

Now, as the electrons and holes have an electric charge, they leave behind positive ions and negative ions respectively near the interface between the n and p regions.

upna Universidad Pública de Navarra Nafarroako Unibertsitate Publikoa

These fixed ions set up an electric field right at the junction pointing from the positively charged ions in the n-side to the negatively charged ions in the p-side (see *Fig.1.14*.a). The free electrons and holes are influenced by this "built-in" electric field with the electrons being attracted towards the positive ions and the holes being attracted towards the negative ions. Thus, the built-in electric field causes some of the electrons and holes to flow in the opposite direction to the flow caused by diffusion (see *Fig.1.14*.b). These opposing flows eventually reach a stable equilibrium where the net flow of electrons and holes across the junction is zero. Therefore, at equilibrium the region across the junction or depletion region is free of mobile charges having only the fixed charges associated with the dopant atoms.

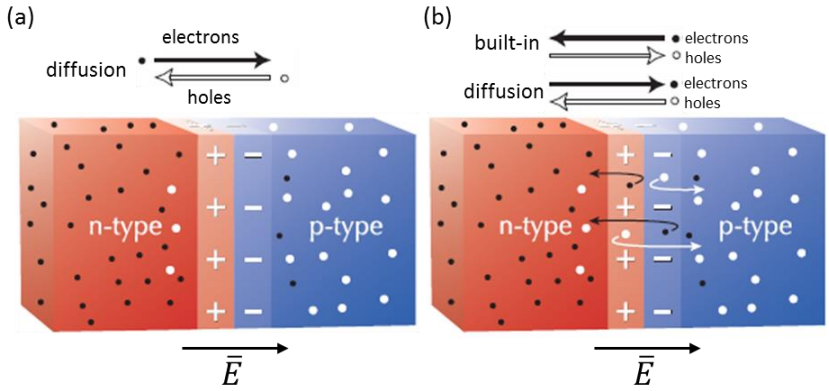

Fig.1.14. Schematic representation of the diffusion process (a) and built-in electric field (b) in a p-n junction. Images source: [64].

When light shines on a p-n junction, as happens in solar cells, more free electron-hole pairs are created and electrons are attracted towards the n-type material side (positively charged) and holes are attracted to the p-type material side (negatively charged). This separation of charges causes a current to flow across the junction from the n-type side to the p-type side. This process is schematically represented in *Fig.1.15*.

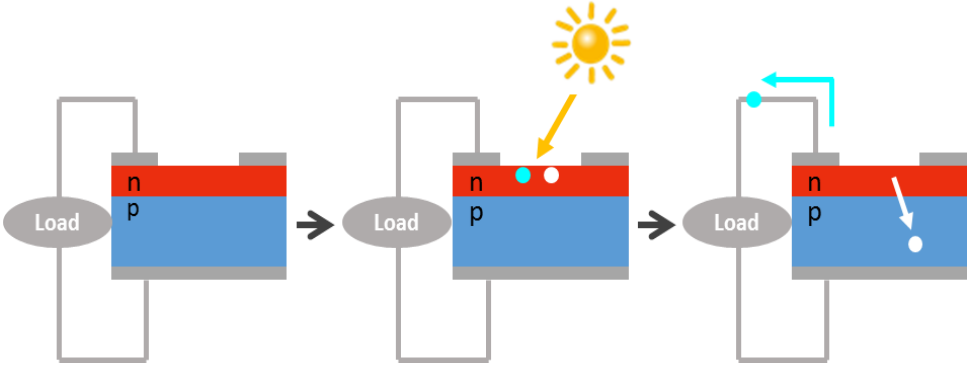

Fig.1.15. Schematic representation of the optoelectronic conversion in a pn junction.

3.5. EFFICIENCY LIMITS

There are many phenomena limiting the performance of optoelectronic devices. Loss processes occurring in a single band gap device under sun illumination can be divided into two distinct categories: intrinsic and extrinsic losses. Intrinsic losses are unavoidable in the device design and will still be present in an idealized solar cell [65]. There are mainly two types of intrinsic losses which determine the efficiencies of ideal solar cells. The first are losses due to the mismatch between the broad solar spectrum and the absorption of a single band gap. Solar photons with energies lower than the energy of the gap are not absorbed and solar photons with energy over the energy gap generate electron hole-pairs which immediately lose almost all energy in excess [66]. The second type of intrinsic losses is due to radiative recombination which is the opposite of the absorption phenomenon. The free carriers go directly from the conduction band to the valence band by emission of a photon. This kind of recombination is important in direct band gap materials but extremely low and usually neglected in indirect band gap semiconductors like Si [66].

The extrinsic limitations includes loses due to reflection, contact shadowing, series resistance, incomplete collection of photogenerated carriers, absorption in inactive layers, surface recombination etc. These losses can in principle be eliminated increasing solar cells efficiency to its ideal limit [69,70]. This work is focused in the reflection losses in Si based solar cells which are one of the most important limitations for this technology.

When the light from the sun traveling through the air reaches a flat Si substrate, more than the 30% of the photons are reflected at the surface due to the change in n at the interface. While the air has a *n* of 1, the Si has a *n* that varies with the wavelength being over 3 in the whole wavelength range of interest for solar cells. This change in *n* causes a change in light velocity and trajectory and part of the light is reflected back at the interface. Therefore, over 30% of the photons do not contribute to the power conversion reducing the final efficiency of the device.

4. ANTI REFLECTION IN SI SOLAR CELLS – STATE OF THE ART

4.1 MICROTREXTURIZATION

Many efforts have been done during the last decades to reduce efficiently light reflection at the Si surface ranging from simple ARCs to more complicated nanostructures based solutions [37,71-74].

Surface texturization of solar cells is a common approach to reduce light reflection and, consequently, increase solar cell efficiency. The p*assivated emitter rear locally diffused* (PERL) cell is a very popular example of a Si based solar cell with texturized surface. This cell appeared in the mid 1970s and since then it has been deeply studied by the scientific community [26,76,77]. The PERL cell is represented in *Fig.1.16*.a. In this cell, there are heavily P diffused regions underneath the metal contacts combined with a lightly diffused top surface that keeps good absorption of the short-wavelength photons. This combination can minimize both contact resistance and contact recombination. Besides, the front surface of the PERL cell is a key feature that contributes to the high performance of the cell. First, the front metal finger grids are defined by photolithography technology to be very thin and therefore to minimize metal shading loss. Moreover, the top surface is textured using micro-inverted pyramid structures and covered by double layer ARC, which reduces surface recombination. Both inverted-pyramid texturing and fine metal fingers decrease the optical losses which contribute to higher current for the solar cells.

The idea behind the micro-texturization used in the PERL cell is to create multiple reflections to obtain total absorbance. As is schematically represented in *Fig.1.16*.b, when light reaches in the wall of one inverted pyramid, the reflected ray has the chance to be absorbed again in the opposite wall. By trapping the light inside the cell, the optical path increases and therefore the light absorption. There is a theoretical limit to the absorption enhancement called “Yablonovitch limit”. This factor was calculated by Eli Yablonovitch using ray optics and can be expressed as [73]:

$$y = \frac{4n^2}{sin^2\theta} \tag{1.10}$$

where n is the refractive index of the active layer, an θ is the angle of incidence with respect to the active layer. Assuming normal incidence, i.e. $\theta = 90°$, the Yablonovich limit is simplified to its popular value of $4n^2$ [79,80].

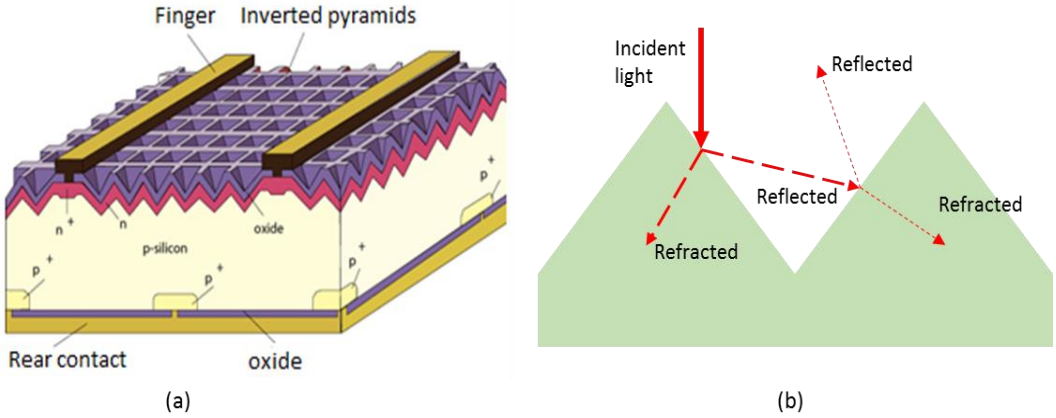

Fig.1.16. PERL cell scheme reprinted from [76] *(a) and the schematic representation of the multi-reflection effect that occurs at its surface due to pyramidal micro-texturization (b).*

Since the PERL cell, many other subsequent designs have appeared [82-84] with micro-texturized surfaces for light management. In fact, micro-texturization is still very popular today and commonly used in commercial devices due to the simple and low-cost processes involved in their fabrication.

The main difference between commercial schemes and the PERL cell surface is the distribution of the microstructures. While the PERL cell texture consists on a periodic pattern of pyramids, commercial devices have random distributions to simplify the fabrication process. Normally, random texturization is obtained by wet etching or mask-less dry etching which can be easily implemented at industrial scale. The most popular fabrication process consists on the immersion of c-Si substrates in a chemical solution which etches the surface following the crystalline directions. This leaves micro inverted pyramids randomly distributed along the surface. The principle of operation of this random distribution is the same explained for the PERL cell and represented in *Fig.1.16.b*.

Fig.1.17 shows two examples of micro-texturization found in the literature together with their measured reflectance. In both cases, the reflectance is over 10% along most of the wavelength range of interest for Si solar cells. In fact, it is difficult to achieve

lower values with this kind of approaches. In commercial solutions, inverted pyramids are combined with AR coatings to reduce the reflectance to acceptable values.

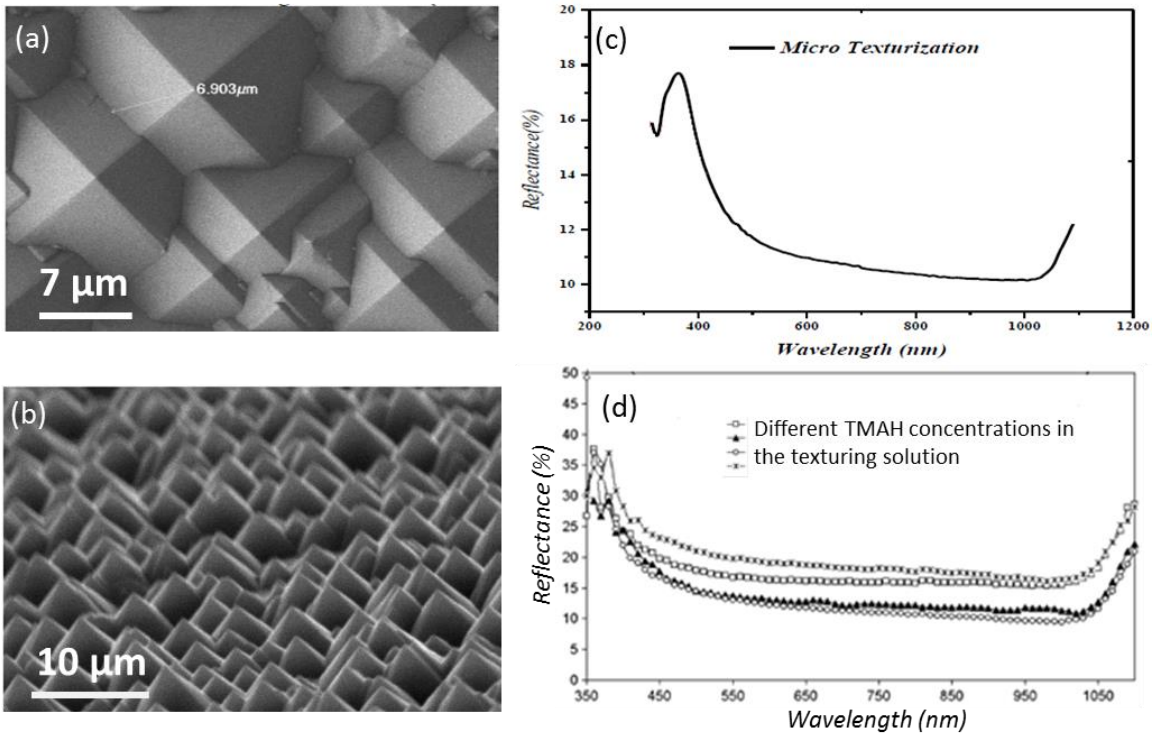

Fig.1.17. Two examples of micro-texturized surfaces (a and b) with their corresponding reflectance measurements (c and d) obtained in [78] *and* [79] *respectively.*

4.2 NANOTEXTURIZATION

With the appearance of next generation of PV devices, i.e. thin film solar cells, new antireflection mechanisms were required due to unsuitability of microstructures to be implemented in such thin layers. The most obvious solution was to reduce the dimensions of the microstructures to the nanoscale. Many efforts have been done during the last decade to design, fabricate and characterize nanostructures for PV applications. With SWS, Si reflectance has been reduced to lower values than those obtained with micro-structures [85-88]. Furthermore, it has been theoretically shown that the optical path length enhancement beyond the Yablonovitch limit is possible with this kind of texturization [82]. *Fig.1.18* shows three recent examples of Si nanostructures and the reflectance measurements for each one. In all the cases, the normal reflectance is close to zero and much lower than the examples of microstructures shown in Fig.1.17.

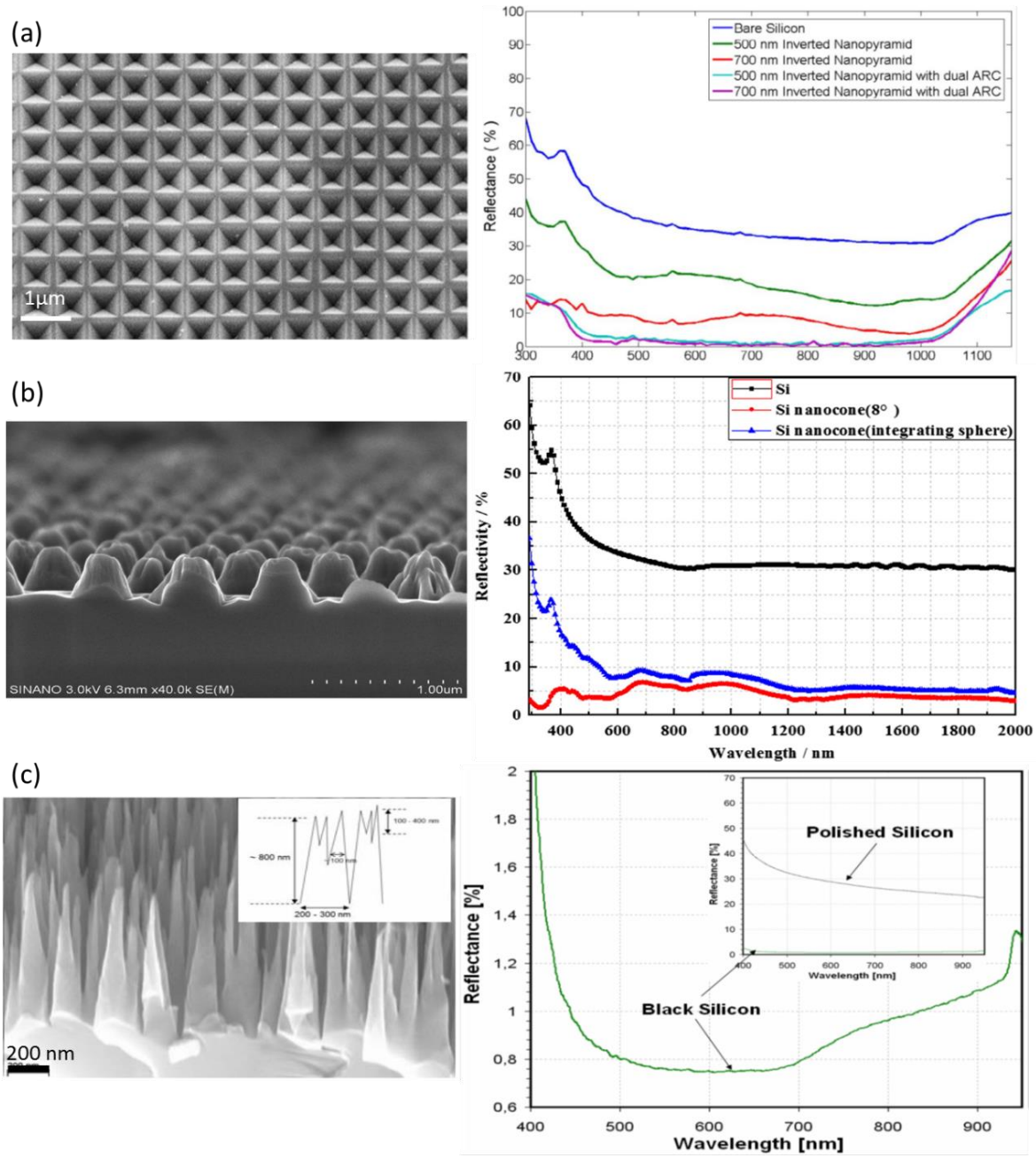

Fig.1.18. Silicon nanostructures and their reflectance measurements from [83] *(a),* [47] *(b) and* [89] *(c).*

The interaction of light with a texturized surface is defined by the dimensions of the irregularities compared to the wavelength. In the case of microtextures, the wavelength is smaller than the structures so light refracts and diffracts at a single interface air - substrate. On the contrary, for nanotextures, the structures are smaller than the wavelength of light so, as explained before, the light interacts with the whole surface rather than interacting with each rough spot [56].

As it happens with microtextures, nanotextures can be random or periodic depending on how the nanostructures are distributed on the surface of the substrate. Random distributions have the advantage of less expensive fabrication techniques and they have shown good AR behavior in the visible region [89]. However, they have low reproducibility and their geometry is difficult to control and optimize when more broadband or specific performance is desired. In contrast, periodic structures are usually fabricated in more controllable processes and their geometries and shapes can be adjusted to those of the model [25,60]. Besides, they are also more suitable for theoretical analysis allowing a better optimization of the dimensions and shapes of that model. The optimization of both the designs and the fabrication processes is an important part of this work so it is restricted to periodic nanostructures.

The optimization of the designs consists on the right selection of geometries and dimensions for the nanostructures. In the literature, different types of periodic nanostructures have been reported showing AR behavior including nanopilars, nanowires, nanocones, nanopyramids and nanodomes [50,60,90]. However, to our knowledge, there is no a deep optimization work to choose the ideal structure along a variety of profiles and dimensions.

For solar cells applications, this optimization should be done taking into account important aspects as the solar spectrum and limitations of the Si substrates. However, once the nanostructure is chosen, its right behavior in a solar cell is not guaranteed. Important parameters like surface recombination and contact losses can be negatively affected by the nanostructures. In this work, the optimization of the nanostructures is done attending to optical and solar cells requirements to optimize the final performance of the devices.

5. REFERENCES

[1] "National Nanotechnology Initiative." [Online]. Available: http://www.nano.gov/.

[2] R. Feynman, "There's plenty of room at the bottom," *Reson. J. Sci. Educ.*, vol. 16, no. 9, pp. 890–905, Sep. 2011.

[3] Taniguchi, "On the Basic Concept of 'NanoTechnology," in *Proceedings*, Tokyo, 1974.

upna Universidad Pública de Navarra Nafarroako Unibertsitate Publikoa

[4] K. E. Drexler, *Engines of Creation*. Fourth Estate Limited, 1996.

[5] M. Barberoglou, "Laser structuring of water-repellent biomimetic surfaces," *SPIE Newsroom*, 2009.

[6] S. Ji, J. Park, and H. Lim, "Improved antireflection properties of moth eye mimicking nanopillars on transparent glass: flat antireflection and color tuning," *Nanoscale*, vol. 4, no. 15, pp. 4603–4610, Jul. 2012.

[7] G. Liao, H. Zuo, Y. Cao, and T. Shi, "Optical properties of the micro/nano structures of Morpho butterfly wing scales," *Sci. China Ser. E Technol. Sci.*, vol. 53, no. 1, pp. 175–181, Jan. 2010.

[8] I. Freestone, N. Meeks, M. Sax, and C. Higgitt, "The Lycurgus Cup — A Roman nanotechnology," *Gold Bull.*, vol. 40, no. 4, pp. 270–277, Dec. 2007.

[9] L. A. Polette-Niewold, F. S. Manciu, B. Torres, M. Alvarado Jr., and R. R. Chianelli, "Organic/inorganic complex pigments: Ancient colors Maya Blue," *J. Inorg. Biochem.*, vol. 101, no. 11–12, pp. 1958–1973, Nov. 2007.

[10] D. F. Emerich and C. G. Thanos, "Nanotechnology and medicine," *Expert Opin. Biol. Ther.*, vol. 3, no. 4, pp. 655–663, Jul. 2003.

[11] J. García-Martínez, *Nanotechnology for the Energy Challenge*. John Wiley & Sons, 2013.

[12] N. Sozer and J. L. Kokini, "Nanotechnology and its applications in the food sector," *Trends Biotechnol.*, vol. 27, no. 2, pp. 82–89, Feb. 2009.

[13] J. Altmann, *Military Nanotechnology: Potential Applications and Preventive Arms Control*. Routledge, 2007.

[14] R. Waser, *Nanoelectronics and Information Technology*. John Wiley & Sons, 2012.

[15] "New Additive to Enhance Surface Cleanability." [Online]. Available: http://www.pcimag.com/articles/new-additive-to-enhance-surface-cleanability. [Accessed: 12-Sep-2014].

[16] "Deutsches Museum: Lotus." [Online]. Available: http://www.deutsches-museum.de/information/jugend-im-museum/erfinderpfad/nano/lotus/. [Accessed: 12-Sep-2014].

[17] K. C. Lee and U. Erb, "Grain boundaries and coincidence site lattices in the corneal nanonipple structure of the Mourning Cloak butterfly," *Beilstein J. Nanotechnol.*, vol. 4, pp. 292–299, May 2013.

[18] "Moth eye (online)," *shutterstock*. [Online]. Available: http://www.shutterstock.com/es/pic-59215597/stock-photo-brown-moth.html?src=pp-photo-168889379-1.

[19] "Artificial Butterfly: Wing Scales Provide Template For Complex Photonic Structures,"*ScienceDaily.*[Online].Available: http://www.sciencedaily.com/releases/2006/12/061211124135.htm. [Accessed: 12-Sep-2014].

[20] “mariposa azul y negra wallpaper - ForWallpaper.com.” [Online]. Available: http://es.forwallpaper.com/wallpaper/blue-and-black-butterfly-420954.html. [Accessed: 12-Sep-2014].

[21] R. Daw, “Nanotechnology is ancient history,” *The Guardian*, 24-Apr-2012.

[22] “Maya Blue Paint Recipe Deciphered,” *DNews*. [Online]. Available: http://news.discovery.com/history/art-history/maya-blue-paint-deciphered-130403.htm. [Accessed: 12-Sep-2014].

[23] Y. Xia, P. Yang, Y. Sun, Y. Wu, B. Mayers, B. Gates, Y. Yin, F. Kim, and H. Yan, “One-Dimensional Nanostructures: Synthesis, Characterization, and Applications,” *Adv. Mater.*, vol. 15, no. 5, pp. 353–389, Mar. 2003.

[24] S.-F. Leung, Q. Zhang, F. Xiu, D. Yu, J. C. Ho, D. Li, and Z. Fan, “Light Management with Nanostructures for Optoelectronic Devices,” *J. Phys. Chem. Lett.*, vol. 5, no. 8, pp. 1479–1495, Apr. 2014.

[25] J. D. Joannopoulos, S. G. Johnson, J. N. Winn, and R. D. Meade, *Photonic Crystals: Molding the Flow of Light (Second Edition)*. Princeton University Press, 2011.

[26] B. Wikipedians, *Physics*. PediaPress.

[27] R. Dick, “The Need for Quantum Mechanics,” in *Advanced Quantum Mechanics*, Springer New York, 2012, pp. 1–23.

[28] S. Chattopadhyay, Y. F. Huang, Y. J. Jen, A. Ganguly, K. H. Chen, and L. C. Chen, “Anti-reflecting and photonic nanostructures,” *Mater. Sci. Eng. R Rep.*, vol. 69, no. 1–3, pp. 1–35, Jun. 2010.

[29] F. Priolo, T. Gregorkiewicz, M. Galli, and T. F. Krauss, “Silicon nanostructures for photonics and photovoltaics,” *Nat. Nanotechnol.*, vol. 9, no. 1, pp. 19–32, Jan. 2014.

[30] S. Matsuo, A. Shinya, C.-H. Chen, K. Nozaki, T. Sato, Y. Kawaguchi, H. Taniyama, and M. Notomi, “20-Gbit/s directly modulated photonic crystal nanocavity laser with ultra-low power consumption,” *Opt. Express*, vol. 19, no. 3, pp. 2242–2250, Jan. 2011.

[31] M. Notomi, A. Shinya, S. Mitsugi, G. Kira, E. Kuramochi, and T. Tanabe, “Optical bistable switching action of Si high-Q photonic-crystal nanocavities,” *Opt. Express*, vol. 13, no. 7, pp. 2678–2687, Apr. 2005.

[32] S. O. Kasap, *Principles of Electronic Materials and Devices*. Boston: Mcgraw-Hill, 2002.

[33] R. Jacobsson, “V Light Reflection from Films of Continuously Varying Refractive Index,” in *Progress in Optics*, vol. Volume 5, E. Wolf, Ed. Elsevier, 1966, pp. 247–286.

[34] J. A. Fawcett and W. H. Gray, “Multi-layer anti-reflection coatings using intermediate layers having monolitically graded refractive index,” 3706485, 19-Dec-1972.

[35] D. Bouhafs, A. Moussi, A. Chikouche, and J. M. Ruiz, “Design and simulation of antireflection coating systems for optoelectronic devices: Application to silicon solar cells,” *Sol. Energy Mater. Sol. Cells*, vol. 52, no. 1–2, pp. 79–93, Mar. 1998.

[36] R. Brunner, B. Keil, C. Morhard, D. Lehr, J. Draheim, U. Wallrabe, and J. Spatz, “Antireflective ?moth-eye? structures on tunable optical silicone membranes,” *Appl. Opt.*, vol. 51, no. 19, pp. 4370–4376, Jul. 2012.

[37] P. B. Clapham and M. C. Hutley, “Reduction of Lens Reflexion by the ‘Moth Eye’ Principle,” *Nature*, vol. 244, no. 5414, pp. 281–282, Aug. 1973.

[38] T. K. Gaylord, W. E. Baird, and M. G. Moharam, “Zero-reflectivity high spatial-frequency rectangular-groove dielectric surface-relief gratings,” *Appl. Opt.*, vol. 25, no. 24, pp. 4562–4567, Dec. 1986.

[39] W. Stork, N. Streibl, H. Haidner, and P. Kipfer, “Artificial distributed-index media fabricated by zero-order gratings,” *Opt. Lett.*, vol. 16, no. 24, pp. 1921–1923, Dec. 1991.

[40] W. E. B. T K Gaylord, “Zero-reflectivity high spatial-frequency rectangular-groove dielectric surface-relief gratings.,” *Appl. Opt.*, vol. 25, no. 24, p. 4562, 1987.

[41] W. Stork, N. Streibl, H. Haidner, and P. Kipfer, “Artificial distributed-index media fabricated by zero-order gratings,” *Opt. Lett.*, vol. 16, no. 24, pp. 1921–1923, Dec. 1991.

[42] K. Han and C.-H. Chang, “Numerical Modeling of Sub-Wavelength Anti-Reflective Structures for Solar Module Applications,” *Nanomaterials*, vol. 4, no. 1, pp. 87–128, Jan. 2014.

[43] W. H. Southwell, “Pyramid-array surface-relief structures producing antireflection index matching on optical surfaces,” *J. Opt. Soc. Am. A*, vol. 8, no. 3, pp. 549–553, Mar. 1991.

[44] D. H. Raguin and G. M. Morris, “Antireflection structured surfaces for the infrared spectral region,” *Appl. Opt.*, vol. 32, no. 7, pp. 1154–1167, Mar. 1993.

[45] W. H. Southwell, “Gradient-index antireflection coatings,” *Opt. Lett.*, vol. 8, no. 11, pp. 584–586, Nov. 1983.

[46] S. Koynov, M. S. Brandt, and M. Stutzmann, “Black nonreflecting silicon surfaces for solar cells,” *Appl. Phys. Lett.*, vol. 88, no. 20, p. 203107, May 2006.

[47] Y. Wang, B. Shao, Z. Zhang, L. Zhuge, X. Wu, and R. Zhang, “Broadband and omnidirectional antireflection of Si nanocone structures cladded by SiN film for Si thin film solar cells,” *Opt. Commun.*, vol. 316, pp. 37–41, Apr. 2014.

[48] C.G. Bernhard, “Structural and functional adaption in a visual system,” *Endeavour*, vol. 26, pp. 79–84, 1967.

[49] S. Ji, K. Song, T. B. Nguyen, N. Kim, and H. Lim, “Optimal Moth Eye Nanostructure Array on Transparent Glass Towards Broadband Antireflection,” *ACS Appl. Mater. Interfaces*, vol. 5, no. 21, pp. 10731–10737, Nov. 2013.

[50] A. R. Parker and H. E. Townley, “Biomimetics of photonic nanostructures,” *Nat. Nanotechnol.*, vol. 2, no. 6, pp. 347–353, Jun. 2007.

[51] Z. Yu, H. Gao, W. Wu, H. Ge, and S. Y. Chou, "Fabrication of large area subwavelength antireflection structures on Si using trilayer resist nanoimprint lithography and liftoff," *J. Vac. Sci. Technol. B*, vol. 21, no. 6, pp. 2874–2877, Nov. 2003.

[52] J. Tommila, A. Aho, A. Tukiainen, V. Polojärvi, J. Salmi, T. Niemi, and M. Guina, "Moth-eye antireflection coating fabricated by nanoimprint lithography on 1 eV dilute nitride solar cell," *Prog. Photovolt. Res. Appl.*, vol. 21, no. 5, pp. 1158–1162, Aug. 2013.

[53] F. L. Gonzalez and M. J. Gordon, "Bio-inspired, sub-wavelength surface structures for ultra-broadband, omni-directional anti-reflection in the mid and far IR," *Opt. Express*, vol. 22, no. 11, pp. 12808–12816, Jun. 2014.

[54] H. Wang, X. Liu, L. Wang, and Z. Zhang, "Anisotropic optical properties of silicon nanowire arrays based on the effective medium approximation," *Int. J. Therm. Sci.*, vol. 65, pp. 62–69, Mar. 2013.

[55] J.-G. Kim, H. J. Choi, K.-C. Park, R. E. Cohen, G. H. McKinley, and G. Barbastathis, "Multifunctional Inverted Nanocone Arrays for Non-Wetting, Self-Cleaning Transparent Surface with High Mechanical Robustness," *Small*, vol. 10, no. 12, pp. 2487–2494, Jun. 2014.

[56] S. Chattopadhyay, Y. F. Huang, Y. J. Jen, A. Ganguly, K. H. Chen, and L. C. Chen, "Anti-reflecting and photonic nanostructures," *Mater. Sci. Eng. R Rep.*, vol. 69, no. 1–3, pp. 1–35, Jun. 2010.

[57] Kyoo-Chul Park, Hyungryul J. Choi, Chih-Hao Chang, Robert E. Cohen, Gareth H. McKinley, and George Barbastathis, "Nanotextured Silica Surfaces with Robust Superhydrophobicity and Omnidirectional Broadband Supertransmissivity," *ACS Nano*, vol. 5, no. 6, pp. 3789–3799, Apr. 2012.

[58] E. B. Grann and M. G. Moharam, "Comparison between continuous and discrete subwavelength grating structures for antireflection surfaces," *J. Opt. Soc. Am. A*, vol. 13, no. 5, p. 988, May 1996.

[59] E. B. Grann, M. G. Varga, and D. A. Pommet, "Optimal design for antireflective tapered two-dimensional subwavelength grating structures," *J. Opt. Soc. Am. A*, vol. 12, no. 2, p. 333, Feb. 1995.

[60] S. U. D. of M. Science, R. H. Bube, A. Fahrenbruch, and P. F. Lindquist, *Mechanism of the Photovoltaic Effect in II-VI Compounds*. 1970.

[61] "Solar Radiation & Photosynthetically Active Radiation," *Environmental Measurement Systems*. [Online]. Available: http://www.fondriest.com/environmental-measurements/parameters/weather/photosynthetically-active-radiation/. [Accessed: 12-Sep-2014].

[62] L. M. Fraas and L. D. Partain, *Solar Cells and Their Applications*. John Wiley & Sons, 2010.

[63] "GREEN RHINO ENERRGY. The Principles of Photovoltaics." [Online]. Available: http://www.greenrhinoenergy.com/solar/technologies/pv_cells.php.

[64] Alistair Sproul, “Understanding the p-n Junction.” .

[65] L. C. Hirst and N. J. Ekins-Daukes, “Fundamental losses in solar cells,” *Prog. Photovolt. Res. Appl.*, vol. 19, no. 3, pp. 286–293, May 2011.

[66] C. H. Henry, “Limiting efficiencies of ideal single and multiple energy gap terrestrial solar cells,” *J. Appl. Phys.*, vol. 51, no. 8, pp. 4494–4500, Aug. 1980.

[67] J. Zhao and M. . Green, “Optimized antireflection coatings for high-efficiency silicon solar cells,” *IEEE Trans. Electron Devices*, vol. 38, no. 8, pp. 1925–1934, Aug. 1991.

[68] J. Zhao, A. Wang, P. Altermatt, and M. A. Green, “Twenty-four percent efficient silicon solar cells with double layer antireflection coatings and reduced resistance loss,” *Appl. Phys. Lett.*, vol. 66, no. 26, pp. 3636–3638, Jun. 1995.

[69] J.-Y. Jung, Z. Guo, S.-W. Jee, H.-D. Um, K.-T. Park, and J.-H. Lee, “A strong antireflective solar cell prepared by tapering silicon nanowires,” *Opt. Express*, vol. 18, no. S3, p. A286, Sep. 2010.

[70] J. Zhao and M. . Green, “Optimized antireflection coatings for high-efficiency silicon solar cells,” *IEEE Trans. Electron Devices*, vol. 38, no. 8, pp. 1925–1934, Aug. 1991.

[71] M. A. Green, A. W. Blakers, S. Narayanan, and M. Taouk, “Improvements in silicon solar cell efficiency,” *Sol. Cells*, vol. 17, no. 1, pp. 75–83, Mar. 1986.

[72] M. . Green, J. Zhao, A. Wang, and S. R. Wenham, “Very high efficiency silicon solar cells-science and technology,” *IEEE Trans. Electron Devices*, vol. 46, no. 10, pp. 1940–1947, Oct. 1999.

[73] E. Yablonovitch, “Statistical ray optics,” *J. Opt. Soc. Am.*, vol. 72, no. 7, pp. 899–907, Jul. 1982.

[74] A. Ingenito, O. Isabella, and M. Zeman, “Experimental Demonstration of 4n2 Classical Absorption Limit in Nanotextured Ultrathin Solar Cells with Dielectric Omnidirectional Back Reflector,” *ACS Photonics*, vol. 1, no. 3, pp. 270–278, Mar. 2014.

[75] S. Fonash, *Introduction to Light Trapping in Solar Cell and Photo-detector Devices*. Elsevier, 2014.

[76] “High Efficiency Solar Cells.” [Online]. Available: http://www.pveducation.org/pvcdrom/manufacturing/high-efficiency. [Accessed: 12-Sep-2014].

[77] P. Panek, M. Lipiński, and J. Dutkiewicz, “Texturization of multicrystalline silicon by wet chemical etching for silicon solar cells,” *J. Mater. Sci.*, vol. 40, no. 6, pp. 1459–1463, Mar. 2005.

[78] Santanu Maity and Sahadev Roy, “Near Sub-Wavelength Texturization Of Silicon Surfaces For Solar Cell Applications,” *Int. J. Sci. Eng. Technol.*, no. 6, p. 511, 2013.

[79] P. Papet, O. Nichiporuk, A. Kaminski, Y. Rozier, J. Kraiem, J.-F. Lelievre, A. Chaumartin, A. Fave, and M. Lemiti, “Pyramidal texturing of silicon solar cell with

TMAH chemical anisotropic etching," *Sol. Energy Mater. Sol. Cells*, vol. 90, no. 15, pp. 2319–2328, Sep. 2006.

[80] K. Hadobás, S. Kirsch, A. Carl, M. Acet, and E. F. Wassermann, "Reflection properties of nanostructure-arrayed silicon surfaces," *Nanotechnology*, vol. 11, no. 3, pp. 161–164, Sep. 2000.

[81] Y.-F. Huang, S. Chattopadhyay, Y.-J. Jen, C.-Y. Peng, T.-A. Liu, Y.-K. Hsu, C.-L. Pan, H.-C. Lo, C.-H. Hsu, Y.-H. Chang, C.-S. Lee, K.-H. Chen, and L.-C. Chen, "Improved broadband and quasi-omnidirectional anti-reflection properties with biomimetic silicon nanostructures," *Nat. Nanotechnol.*, vol. 2, no. 12, pp. 770–774, 2007.

[82] Z. Yu, A. Raman, and S. Fan, "Fundamental limit of nanophotonic light trapping in solar cells," *Proc. Natl. Acad. Sci.*, vol. 107, no. 41, pp. 17491–17496, Oct. 2010.

[83] S. Sivasubramaniam and M. M. Alkaisi, "Inverted nanopyramid texturing for silicon solar cells using interference lithography," *Microelectron. Eng.*, vol. 119, pp. 146–150, May 2014.

[84] K. N. Nguyen, D. Abi-Saab, P. Basset, E. Richalot, F. Marty, D. Angelescu, Y. Leprince-Wang, and T. Bourouina, "Black silicon with sub-percent reflectivity: Influence of the 3D texturization geometry," in *Solid-State Sensors, Actuators and Microsystems Conference (TRANSDUCERS), 2011 16th International*, 2011, pp. 354–357.

[85] B. Hua, Q. Lin, Q. Zhang, and Z. Fan, "Efficient photon management with nanostructures for photovoltaics," *Nanoscale*, vol. 5, no. 15, pp. 6627–6640, Jul. 2013.

CHAPTER 2. CONTEXT AND OBJECTIVES

1. RESEARCH GROUP AND PROJECTS

The PhD candidate, Sagrario Dominguez, graduated with a master degree in telecommunication engineering (2003 - 2009) and with a postgraduate degree in communications (2010-2011), both at the Public University of Navarra (UPNA). At the end of 2009, she joined the Foundation for the Research and Development in Nanotechnology (FideNa) thanks to a grant of the government of Navarra (067/11/09). There, she started the PhD studies under the supervision of Dr. Jesús Pérez-Conde and Dr. Javier Bravo in the fields of nanotechnology and optics. In 2012 she did a 9 months research stay at the Massachusetts Institute of Technology (MIT) in the group of professor George Barbastathis, where part of the work presented in this thesis was also developed. In 2013, FideNa merged to the Multidisciplinary Centre of Technologies for the Industry (CEMITEC). There, in the Materials Deposition Area, she has ended the PhD and works at present.

The present work has been developed within the frame of two collaborative projects between FideNa/CEMITEC and the National Renewable Energy Center (CENER) supported by the government of Navarra:

- CFVNANOTEXT: Development of superficial structures to improve the radiation absorption in photovoltaic (PV) solar cells. (Expedient number IIM13156.RA1) (2010-2012).
- SiGlass: Superficial nanostructures to improve the absorption of PV solar cells (Expedient number IIM13156.RI1) (2012-2014).

Both projects were focused on the fabrication of periodically nanostructured surfaces for solar cells applications. The first one was focused on the design of nanostructures

to improve the optical behavior of Si for solar cell applications, the fabrication of periodic nanostructures and the optimization of all the different integration processes. The second project was focused on the use of all the knowledge acquired in the first one to achieve the integration of nanostructured silicon (Si) solar cells on industrial substrates following industrial processes. Besides, part of this project was dedicated to design nanostructures for novel technologies based on thin film absorbers.

2. OBJECTIVES OF THIS THESIS

This work is focused on the improvement of the light absorption of Si by the nanostructuration of its surface with periodic patterns. There are two general objectives: the improvement of the light absorption of bulk Si solar cells in their wavelength range of operation and the maximization of the absorption of Si in a broader wavelength band for other applications. These general objectives include all the following specific objectives:

2.1. OPTIMIZATION OF NANOSTRUCTURES: GEOMETRY AND DIMENSIONS.

The first objective is the design of two optimum nanostructures: one for bulk Si in solar cell application and the second to maximize the light absorption along the broader possible wavelength range. This means the achievement of the following operative goals:

- Design of different nanostructures according to our fabrication capabilities. The idea is to study as many different structures as possible to obtain reliable conclusions.
- Development of a methodology to optimize by simulation the optical response of any kind of periodic nanostructure along the wavelength range of interest. This implies the selection of the appropriate software, the definition of models for the Si nanostructures, the simulation of the sunlight propagation and the calculation of the reflection at the nanostructured Si surface.
- Development of a process to choose between the different designed nanostructures depending on the simulation results and the intended behavior.

upna Universidad Pública de Navarra Nafarroako Unibertsitate Publikoa

In the case of the nanostructures for bulk Si solar cells, the complete optimization process is explained in detail in the section 1 of chapter 4 (*"Photonic crystals for solar cells"*) where the optimum design is obtained. Two publications summarize the results [1,2].

In the case of nanostructures for maximum broadband absorption, the related literature gives enough clues for the optimum design and not much optimization is needed. This is explained in section 3 of chapter 4 and published in [3].

2.2. FABRICATION OF PERIODIC NANOSTRUCTURES.

The second objective is the development of fabrication processes for the designed nanostructures. This implies the knowledge of all the techniques defined in Chapter 3 and the ability of combine them to obtain the intended geometries and dimensions in each situation. In this case, there are three operative objectives:

- Fabrication of periodic nanostructures "reasonably feasible" with the fabrication processes available on the optimum substrates for such processes. This allows the increase of the knowledge on the fabrication techniques and makes it possible to move to more ambitious objectives.

  In the section 1 of chapter 4, the fabrication processes developed for different structures on circular polished Si wafers are presented. Besides, the results have been published in two articles [1,2].

- Adjustment of the developed nanofabrication processes to industrial PV substrates. The size and superficial roughness of the typical PV industry substrates complicate the nanostructuration of their surface by the available techniques. Therefore, the nanofabrication processes previously developed on polished substrates need to be modified. This way, it will be possible to integrate nanostructured solar cells following industrial processes.

  This objective has been accomplished and the results are explained in the section 2 of chapter 4. Besides, these results have been published in a scientific article [4].

- Development of a fabrication process to create ultra-high aspect ratio nanostructures with enhanced antireflective properties. The fabrication capabilities

acquired previously allows us to fabricate new structures with much better antireflection.

The results related to this objective are detailed in section 3 of chapter 4 and published in [3].

3. REFERENCES

[1] S. Domínguez, O. García, M. Ezquer, M. J. Rodríguez, A. R. Lagunas, J. Pérez-Conde, and J. Bravo, "Optimization of 1D photonic crystals to minimize the reflectance of silicon solar cells," *Photonics Nanostructures - Fundam. Appl.*, vol. 10, no. 1, pp. 46–53, 2012.

[2] S. Domínguez, I. Cornago, O. García, M. Ezquer, M. J. Rodríguez, A. R. Lagunas, J. Pérez-Conde, and J. Bravo, "Design, optimization and fabrication of 2D photonic crystals for solar cells," Photonics Nanostructures - Fundam. Appl., vol. 11, no. 1, pp. 29–36, 2013.

[3] S. Dominguez, I. Cornago, J. Bravo, J. Pérez-Conde, H. J. Choi, J.-G. Kim, and G. Barbastathis, "Simple fabrication of ultrahigh aspect ratio nanostructures for enhanced antireflectivity," J. Vac. Sci. Technol. B, vol. 32, no. 3, p. 030602, May 2014.

[4] I. Cornago, S. Dominguez, M. Ezquer, M. J. Rodríguez, A. R. Lagunas, J. Pérez-Conde, R. Rodriguez, and J. Bravo, "Periodic nanostructures on unpolished substrates and their integration in solar cells," Nanotechnology, vol. 26, no. 9, p. 095301, Mar. 2015.

CHAPTER 3. MATERIAL AND METHODS

1. OPTIMIZATION OF PERIODIC NANOSTUCTURES

In this work, we have studied and compared between them different types of periodic nanostructures. The design of the geometries of these nanostructures has been done according to our fabrication capabilities and then, the dimensions of each design have been optimized to obtain minimum reflectance. Consequently, we have developed a complete optimization process based on computer simulation. This process involves three important stages.

First, the design of a sequence of simulations that allows us to obtain enough information to calculate the optimum dimensions of a given design in the last stage. This has been done by a statistical method known as design of experiments (DOE). Second, the development of the defined simulations and finally, the last stage is the post-processing of the output data to find the optimum design.

2.1. DESIGN OF EXPERIMENTS

DOE is a systematic, rigorous approach to engineering problem-solving that applies principles and techniques at the data collection stage so as to ensure the generation of valid, defensible, and supportable engineering conclusions. In addition, all of this is carried out under the constraint of a minimal expenditure of engineering runs, time, and money [1]. Basically, it consists on the definition of a sequence of controlled experiments and the application of some technique to analyze the results obtaining useful information about the influence of some factors in a particular scientific phenomenon. In this work these factors are the dimensions of the designed nanostructures.

We use the response surface methodology (RSM), which defines a model to estimate a response (output variable) for any value of a set of pre-defined variables (input variables) [2]. In particular, the RSM has been used to calculate a model for the reflectance of the nanostructures (output variable) as a function of their dimensions (input variables). The commercial software DOE PRO XL has been used to define the DOE for each studied structure and to construct the model. The objective is to find the optimal dimensions of the structures, which minimize the reflectance.

To construct the model, the input variables are first defined in a range of values and discretized in a set of points along this range. Then, the response is evaluated at some of these points in a set of experiments or runs. According to the response values and the kind of fitting desired, the model is defined. The most common approximations are low-order polynomials (first or second orders). In this work, a second order model is used, which can capture the influence of each input variable in the output and the interaction between the input variables. A general second-order model is defined as:

$$y = a_0 + \sum_{i=1}^{n} a_i x_i + \sum_{i=1}^{n} a_{ii} {x_i}^2 + \sum_{i=1}^{n} \sum_{j=1}^{n} a_{ij} x_i x_j \ ; i < j \qquad (3.1)$$

where x_i and x_j are the design variables and a the tuning parameters.

The estimation of the tuning parameters in a quadratic model requires the study of the variables at three different levels (3-level design) [2]. Therefore, for a large number of variables (N), the number of experiments can become impractical (3^N).

To avoid this problem, we have used a central composite design (CCD). In a CCD, the input variables are studied only at two levels (at their upper and lower bounds, named node points), plus a central point and some points out of the range named star points. Then, there is the same number of runs as in a 2-level model (2^N) plus some additional runs. When these runs are performed, linear regression is used to estimate all the tuning parameters of a 3-level model.

1.1.1. 3-level CCD with 2 variables

The experiments of a 3-level CCD with 2 input variables can be represented in a square as in *Fig.3.1*. The node points correspond to experiments with the variables at the lower or upper bounds of the studied range, the center point to the experiment where

the variables are at its central value and the stars points are experiments with the variables at an α value out of the range.

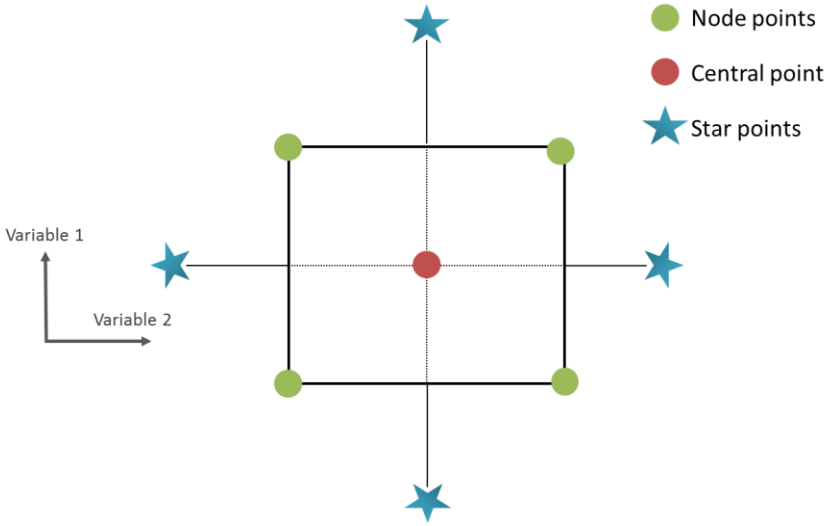

Fig.3.1. 3-level CCD with two input variables.

There are many different methods to select a useful value for the star points. In this work, these values are set as:

$$\alpha = \sqrt[4]{2^N} \tag{3.2}$$

This value of α makes the design to be rotable, which means that the variance of the predicted response at any point depends only on the distance from this point to the center point of design [3]. Therefore, the rotable design provides the uniformity of prediction error. Following this criterion, in a CCD with two variables (N=2), the value of α is 1.41, which result in the DOE of *Table 3.1*.

# run	Encoded values	
	Period	Heigth
1	-1	-1
2	-1	1
3	1	-1
4	1	1
5	0	0
6	-1.41	0
7	1.41	0
8	0	-1.41
9	0	1.41

Table 3.1. DOE for a rotable 3-level CCD with two variables. The runs #1-4 correspond to the node points, the run #5 to the center point and the run #6-9 to the star points.

In a CCD, normally, the experiment corresponding to the central point is repeated a number of times to have an idea about the variability of the response and take this into account in the model. In the software used in this work, the number of repetitions can be chosen depending on the desired accuracy. The more repetitions, the best the estimation of the variability. However, in our case, the runs are computer simulations so there is no error in the response, i.e. different simulations with the same parameters give the same response. Therefore, the central point, as well as the others, is simulated only once. Then, in the design, the number of repetitions of the central point is set to its default value for the software, which is 2^N. The output for all the repetitions is the same so that the model assumes no variability.

1.1.2. 3-level CCD Designs with 3 variables

In most of the DOEs of this work, three input variables are considered resulting in a CCD design like the one represented in *Fig.3.2*. This design consists in 15 runs: 8 node points, 1 central point and 6 stars points.

The sequence of runs of the corresponding DOE is summarized in *Table 3.2*. The star points are calculated according to equation (3.2) resulting in +/-1.68 ($\sqrt[4]{2^3}$).

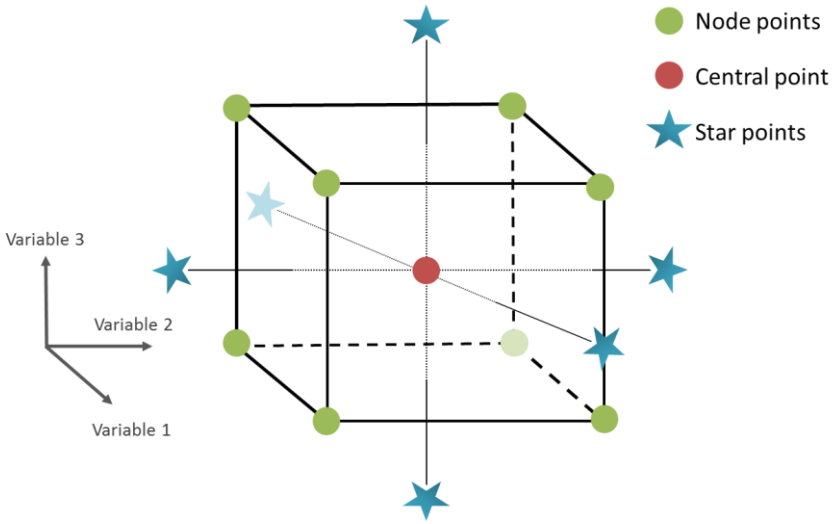

Fig.3.2. Central composite design for 3 variables at 2 levels.

# run	Encoded values		
	Variable 1	Variable 2	Variable 3
1	-1	-1	-1
2	-1	-1	1
3	-1	1	-1
4	-1	1	1
5	1	-1	-1
6	1	-1	1
7	1	1	-1
8	1	1	1
9	0	0	0
10	-1.68	0	0
11	1.68	0	0
12	0	-1.68	0
13	0	1.68	0
14	0	0	-1.68
15	0	0	1.68

Table 3.2. DOE for a rotable 3-level CCD with 3 variables. Runs #1- 8 correspond to the node points, run #9 to the centre point and runs #10-15 to the star points.

2.2. SIMULATION OF PERIODIC NANOSTRUCTURES

In this work, we use finite-difference time-domain (FDTD) method to study the antireflective (AR) behavior of periodic nanostructures. FDTD is a time-based space-discretized method which gives an explicit numerical solution to Maxwell´s equations [4,5]. Though it is computationally intense, it has the benefits of covering a wide wavelength range in a single simulation. Besides, the FDTD method outputs field strength results over the whole geometry and is capable of modeling arbitrary shapes [6].

We use the FDTD algorithm implemented in the commercial software package OptiFDTD, which allows computer aided design and simulation of advanced passive photonic components [7].

1.2.1. FDTD equations

The FDTD approach is based on a direct numerical solution of the time-dependent Maxwell´s equations:

Faraday´s Law: $$\frac{\partial \vec{B}}{\partial t} = -\nabla x \vec{E} - \vec{M} \quad (3.3)$$

Ampere´s Law: $$\frac{\partial \vec{D}}{\partial t} = \nabla x \vec{H} - \vec{J} \quad (3.4)$$

Gauss´s Laws $$\nabla \cdot \vec{D} = \rho$$

$$\nabla \cdot \vec{B} = \rho^* \quad (3.5)$$

Continuity Equations: $$\nabla \cdot \vec{J} = -\frac{\partial}{\partial t}\rho$$

$$\nabla \cdot \vec{M} = -\frac{\partial}{\partial t}\rho^* \quad (3.6)$$

Where $\vec{B}$ is the magnetic field, $\vec{D}$ is the electric flux density and $\vec{E}$ is the electric field intensity, $\vec{H}$ is the magnetizing field, $\vec{J}$ is the electric current density, $\vec{M}$ is the magnetization, ρ is the electric charge density and ρ^* is the equivalent magnetic loss.

The FDTD software is based in Yee´s scheme derived by Kane S. Yee in 1966 [8]. The formulation is based on discretizing the volume domain with a regular rectangular grid named Yee´s cell [9] (*Fig.3.3*).

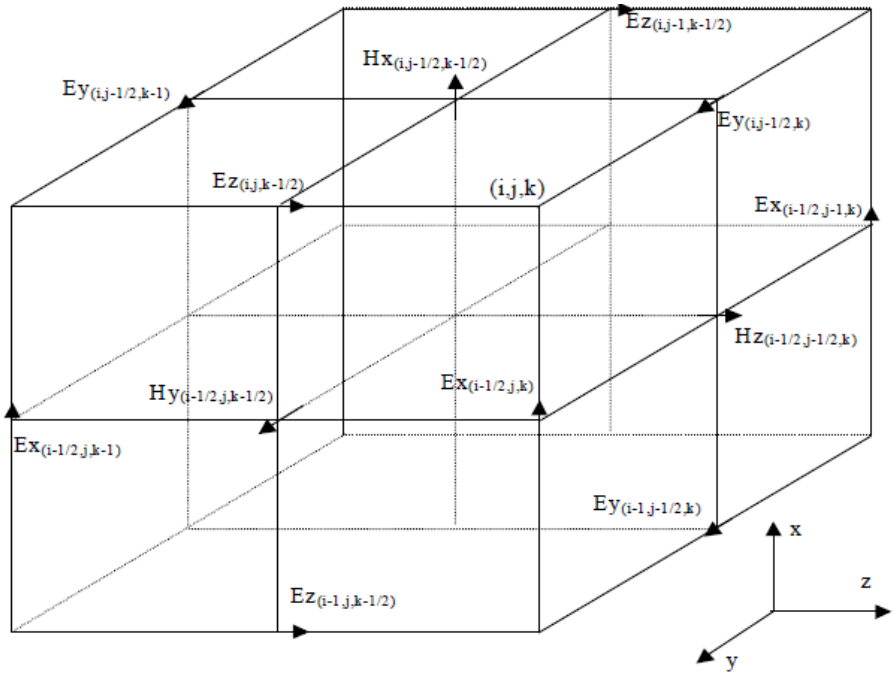

Fig.3.3. Displacement of the electric and magnetic field vector components about a cubic unit cell of the Yee space lattice reprinted from [7].

In Yee´s scheme, the model under analysis laid out in the X-Y-Z space, which is first divided into a lattice of small cubes. Each node of the lattice is associated with a specific type of material containing information about its properties such as refractive index (n) and dispersion parameters. Each field component is placed in the edges of

the lattice as shown in *Fig.3.3*. The indices i, j and k account for the number of space steps in the x, y and z direction respectively. In OptiFDTD, and in this work, the coordinates system is defined as in *Fig.3.3*. Besides, in this work, z is always set as the propagation direction.

The equations are solved interleaving E and H components: if E is updated at a given instant in time, H is update at the next instant in time; and the process is repeated over and over again until the desired transient or steady-state electromagnetic field behavior is fully evolved [10].

1.2.2. Boundary conditions

The boundary conditions are the set of conditions specified for the behavior of the fields at the boundary of the discretized domain. Boundary conditions can easily make the difference between successful and unsuccessful computation, or between a fast and a slow one [11].

In OptiFDTD there are several choices for the type of boundary conditions: anisotropic perfectly matched layer (APML), perfect electric conductor (PEC), perfect magnetic conductor (PMC) and periodic boundary condition (PBC). In the simulations carried out in this thesis, APML and PBC boundaries are used.

1.2.2.1. APML boundary condition

A perfectly matched layer (PML) is an artificial absorbing layer for wave equations. PML is that is designed so that the waves incident upon the PML from a non-PML medium do not reflect at the interface. Therefore, the PML strongly absorbs outgoing waves from the interior of a computational region without reflecting them back to the interior [12].

OptiFDTD uses the uniaxial or anisotropic PML (APML), in which the PML is described as an artificial anisotropic absorbing material [13]. The absorbing properties of APML boundary are physically equivalent to the properties of an absorbing uni-axial anisotropic medium [14]. A plane wave incident on a half space composed of the above uni-axial medium is purely transmitted into it regardless of the angle of incidence, polarization and frequency of the incident wave.

In this work, the APML condition is used at both the beginning and the end of the propagation direction (z) to avoid undesired reflections.

1.2.2.2. PBC Boundary condition

The PBC condition used in OptiFDTD is schematically represented in *Fig.3.4*. It is based on the Bloch´s Theorem, which states that the wave function of a particle in a periodically-repeating environment is a combination of a periodic function, with the same periodicity as the environment, and an enveloping plane wave [15]. Therefore, the whole wave has the following form:

$$\psi(\gamma + \Delta\gamma) = e^{ik\cdot\Delta\gamma}\varphi(\gamma) \tag{3.7}$$

where γ is the position, $\Delta\gamma$ is the period of the environment, φ is a periodic function with the same periodicity as the environment and k is called the wave vector. That means that the wave function in equivalent positions of different periods differs only by a phase $e^{ik\cdot\Delta\gamma}$ factor.

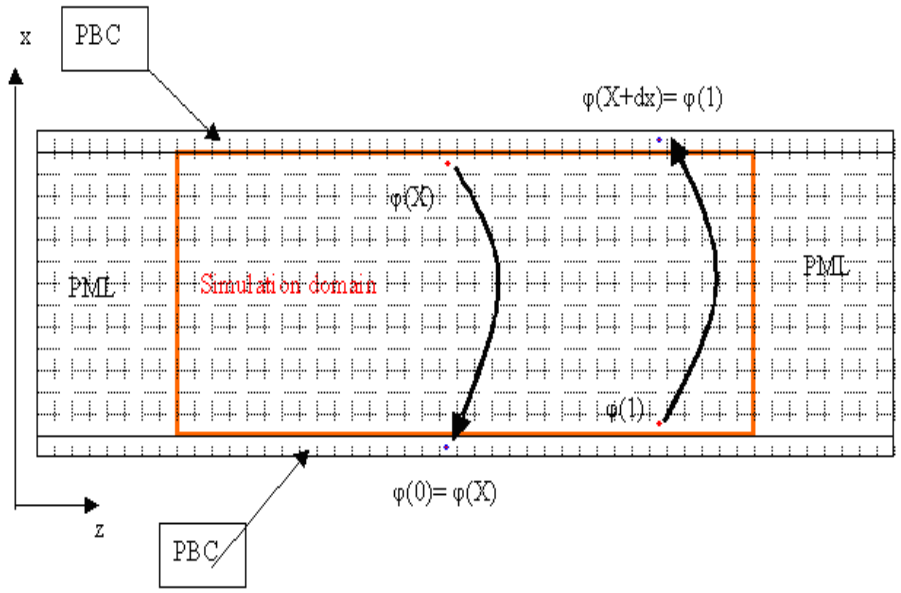

Fig.3.4. Schematic representation of the PBC boundary condition reprinted from [7].

In OptiFDTD, the Bloch´s Theorem is simplified to the case where there are no phase difference between periods, i.e. the k-vector is zero, so the equation (3.7) becomes [7]:

$$\psi(\gamma + \Delta\gamma) = \varphi(\gamma) \tag{3.8}$$

where $\Delta\gamma$ is the periodic length of the edge which is set to periodic boundary condition, $\varphi(\gamma)$ is the field component at the edge of the simulation domain and

$\psi(\gamma + \Delta\gamma)$ is the corresponding field value at the boundary of the opposite edge of the $\varphi(\gamma)$. The situation is shown in *Fig.3.4*.

1.2.3. Input source

The FDTD algorithm starts with an initial field excitation that is propagated through the computational domain. Two types of incident fields are used in this work: continuous waves (CW) and pulsed excitations.

1.2.3.1. Continuous waves

CWs are used to simulate a single wavelength sinusoidal function propagating until it reaches the stationary state everywhere in the computational window.

For example, in a 2D simulation the incident E_y field has the following form [7]:

$$E_y(x, z_{inc}) = AF(x, z_{inc})\sin(\omega t + \theta_i) \tag{3.9}$$

where A is the field amplitude, $F(x, z_{inc})$ is the transverse field distribution at z_{inc}, θ_i is the phase difference between points in the incidence plane, and $\omega = (2\pi/\lambda)c$ is the frequency of the input wave.

1.2.3.2. Pulsed excitations

Pulsed excitations are used to simulate a range of wavelengths propagating until the desired time response is observed at the points of interest.

In this case, the E_y incident field has the form [7]:

$$E_y(x, z_{inc}) = AT(t)F(x, z_{inc})\,\sin(\omega t + \theta_i) \tag{3.10}$$

where

$$T(t) = e^{-\frac{1}{2}\left(\frac{t-t_{off}}{t_0}\right)^2} \tag{3.11}$$

is the pulse envelope function, t_{off} is the time offset and t_0 is the pulse width parameter.

1.2.4. Material models

Two different types of materials are modeled in this work: constant dielectrics such as air and dispersive materials, such as Si, with frequency dependent n and dielectric permittivity (ε).

1.2.4.1. Constant dielectrics

Constant dielectric materials like air are characterized by a complex refractive index value ($\tilde{n}$) or relative permittivity value (ε_r).

$$\tilde{n} = n + ik$$

$$\varepsilon_r = \varepsilon_r' + i\varepsilon_r'' \tag{3.12}$$

$$\varepsilon_r = \tilde{n}^2$$

Here, *k* is the extinction coefficient, which indicates the amount of absorption loss when the electromagnetic wave propagates through the material.

1.2.4.2. Dispersive materials

In the case of dispersive materials, such as Si, their n and ε dependence with frequency needs to be considered in FDTD algorithm. In this work, Si structures are simulated using CWs. To do that, the wavelength range of interest is discretized and one different simulation is run for each wavelength with its corresponding value of n and ε.

Also, there are some models available in the OptiFDTD software that numerically express the relationship between n and frequency of dispersive materials. These models can be solved in the FDTD algorithm giving a continuous response in certain wavelength range. The most used model is the Lorentz-Drude which is defined as follows [7]:

$$\varepsilon_r(\lambda) = \varepsilon_0 + \sum_{m=1}^{N} \frac{A_m \lambda^2}{\lambda^2 + j\gamma_m \lambda - {\lambda_m}^2} \tag{3.13}$$

Where A_m is the strength, Γ_i is the damping factor or collision wavelength and λ_i the oscillating frequency. OptiFDT has a library with all these parameters calculated for many materials in different wavelength regions.

1.2.5. Simulation parameters

Besides boundary conditions, the fundamental constraint of FDTD method is the step size for both the time and space. Space and time steps relate to the accuracy, numerical dispersion and stability of the FDTF method. In general, to keep the results as accurate as possible, with a low numerical dispersion, the mesh size often used is

"10 cells per wavelength", meaning the side of each cell should be 1/10λ or less at the shortest wavelength [16].

OptiFDTD automatically calculates a mesh size solving the equation:

$$minimum\ (\Delta x, \Delta y, \Delta z) \leq \frac{\lambda_{min}}{10 n_{max}} \tag{3.14}$$

where $\Delta x, \Delta y$ and Δz are the sizes of the mesh in the x, y and z directions respectively; λ_{min} is the minimum wavelength and n_{max} the maximum n in the computational cell.

Once the cell is determined, Optiwave also calculates the maximum time step, Δt, following the Courant-Friedrichs-Lewy condition [17,11]:

$$\Delta t \leq \frac{1}{v\sqrt{\frac{1}{\Delta x^2}+\frac{1}{\Delta y^2}+\frac{1}{\Delta z^2}}} \tag{3.15}$$

where v is the speed of the light in the medium.

However, according to our experience, the automatic calculation of mesh size and number of time steps in OptiFDTD is not always accurate enough. In this work, these parameters have been optimized prior to the final analysis.

In most of the cases, we analyze Si nanostructures with sizes between 100 nm and 1000 nm and light between 300 and 1200 nm of wavelength so we have optimized the simulation parameters in this scenario. Different mesh sizes and number of time steps have been used starting from the values suggested by OptiFDTD and varying them till the output parameter converges. The result of this optimization is shown in *Fig.3.5*. The graph plots the normalized response obtained for an average structure under different simulation conditions. While the output with the meshes of 3 nm and 1 nm converge to values close to each other, the output with the 5 nm mesh is far with a 60% of difference. Therefore, in this work, the mesh of 3 nm has been set as default since the 5 nm mesh is inaccurate and the 1 nm mesh require too much computational effort.

Once the mesh size is chosen, the evolution of the output with the increase of the number of time steps is studied. As can be seen in *Fig.3.5*, at some number of time steps, the output stabilizes and from that point, it is almost constant. This number of time steps is then chosen as the most efficient value for the simulation. For the mesh

size of 3 nm, 5000 time steps have been chosen as default parameter. We have validated these default values of mesh size and time steps by comparison of simulation results and experimental measurements (*Fig.3.6*).

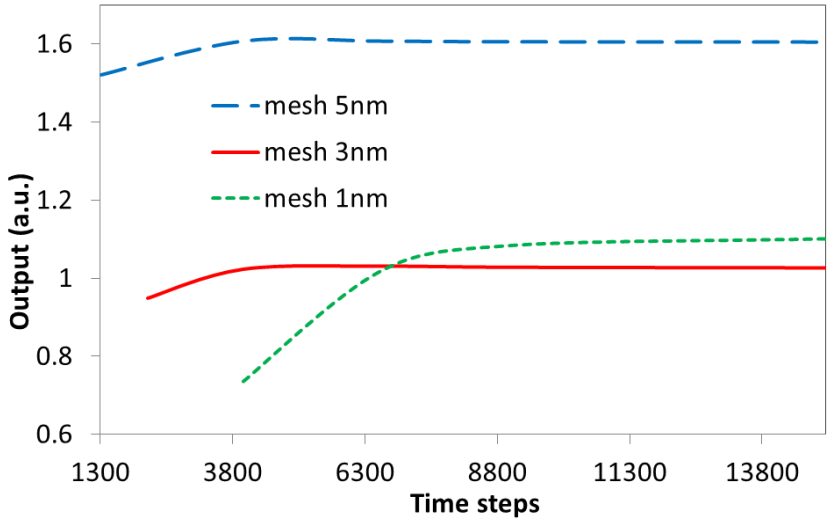

Fig.3.5. Simulation results for a particular model for different mesh sizes and number of time steps. There is a 16% of difference between the output calculated with the 3 nm mesh and with the 1 nm mesh. This value has been considered as acceptable so the mesh size has been set at 3 nm as a compromise result between accuracy and computational time. For the mesh of 3 nm, the output keeps stable from 4000 time steps of simulation. In general, 5000 has been chosen as the default value for the simulations.

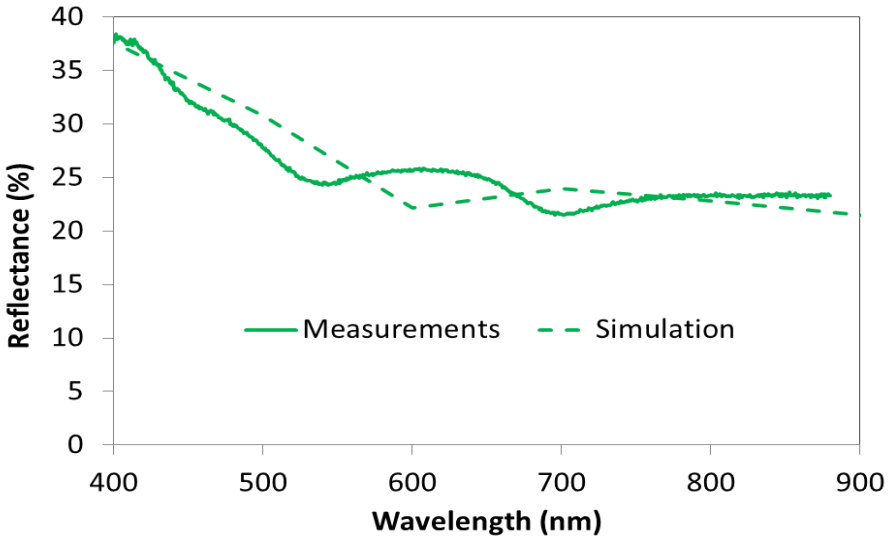

Fig.3.6. Comparison of the simulated and measured reflectance of a periodic nanostructure of lines with 600 nm of period. The simulation has been carried out with a mesh of 3nm and 5000 time steps. The good agreement between simulation and measurement validates the simulation parameters.

In *Fig.3.6* we show the simulated and measured reflectance for a periodic nanostructure of lines with 600 nm of. Both curves are presented as obtained, without any treatment and the maximum difference between them is 6% at 650 nm of wavelength. Taking into account the difference between the ideal model simulated and the real fabricated sample, this is a very good result, which confirms that the simulation method is correct for predict the final reflectance of the fabricated samples.

1.2.6. Output data

The fields propagated by the FDTD algorithm are the time domain fields. At the end of the simulation, these fields need to be at the stationary state in order to obtain all the useful information such as transmitted and reflected powers. This information is obtained by a time Fourier transformation performed in the last time period of the simulation at the desired points of the layout.

In this work, most of the simulations are carried out using the Total/Reflected Field formulation [7]. This means that the computational domain is separated into two sub-regions; the total field region and the reflected field region, separated by the incident field (see *Fig.3.7*).

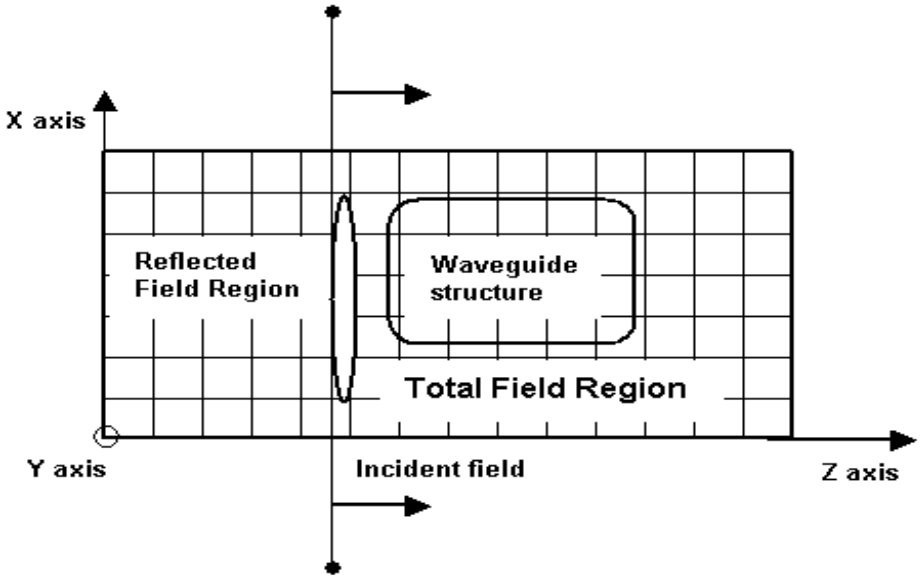

Fig.3.7. Total/reflected field formulation scheme reprinted from [7].

In the total field region, the structures of interest are designed. The interaction between the incident field and the structures take place in this region and therefore it contains information of both the incident and reflected waves from the structures. In contrast, there are no objects in the reflected field region and the propagating waves

upna Universidad Pública de Navarra Nafarroako Unibertsitate Publikoa

correspond only to the fields reflected from the total field region. Therefore, to calculate the reflected power at the nanostructures under study in this work, an output plane (i.e. a detector) is always located in the reflection region.

One example of this scenario for the simulation of a periodic structure with the input source and the output plane is shown in *Fig.3.8*. The dimensions (h, w and p in the figure) and geometries are adjusted for each structure.

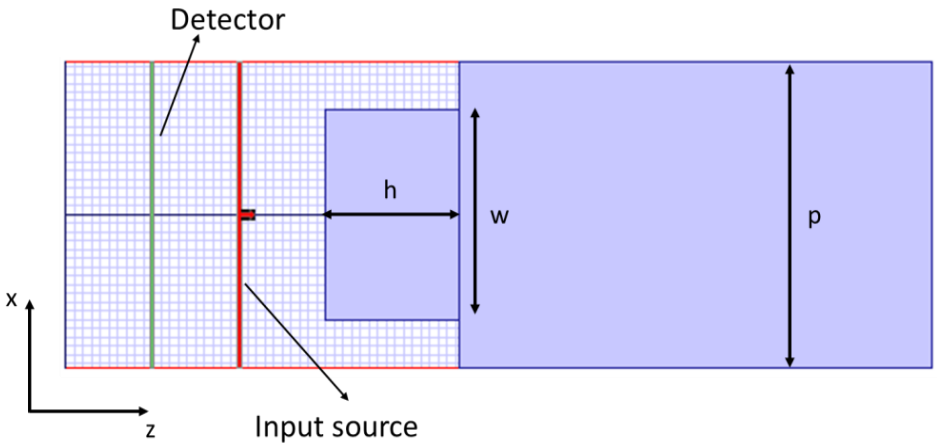

Fig.3.8. Simulation layout for the structure (a).

2.3. POST-PROCESSING OF THE SIMULATION DATA

As explained in section 1.1 of this chapter, a number of simulations are carried out for each structure with different values of its parameters (input variables in the DOE). Each simulation is done in certain wavelength range according to the desired application. This means that the output of the simulation is a curve, i.e. a sequence of pairs reflectance/wavelength. However, to compare between different structures and construct the model for the RSM, one single output value per run is required. Therefore, it is necessary to calculate an average reflectance along the wavelength range after the simulation.

In this work, due to the final application, most of the simulations are done in the range of performance of bulk Si solar cells (300 nm – 1150 nm). In these cases, the average of the final reflectance is calculated according to the spectral efficiency of bulk Si solar cells (*Fig.3.9*.a) and the sunlight spectra (*Fig.3.9*.b), weighting more the wavelengths where the sun emits more energy and the Si has more capability of conversion. This way, the weighting curve is the product between these two curves, shown in *Fig.3.9*.c.

The integral of the reflectance spectrum obtained in simulations multiplied by the weighting curve is used as the output value for the DOE analysis. The RSM optimization consists in in minimizing this value so the reflectance is also minimized for the solar cell application.

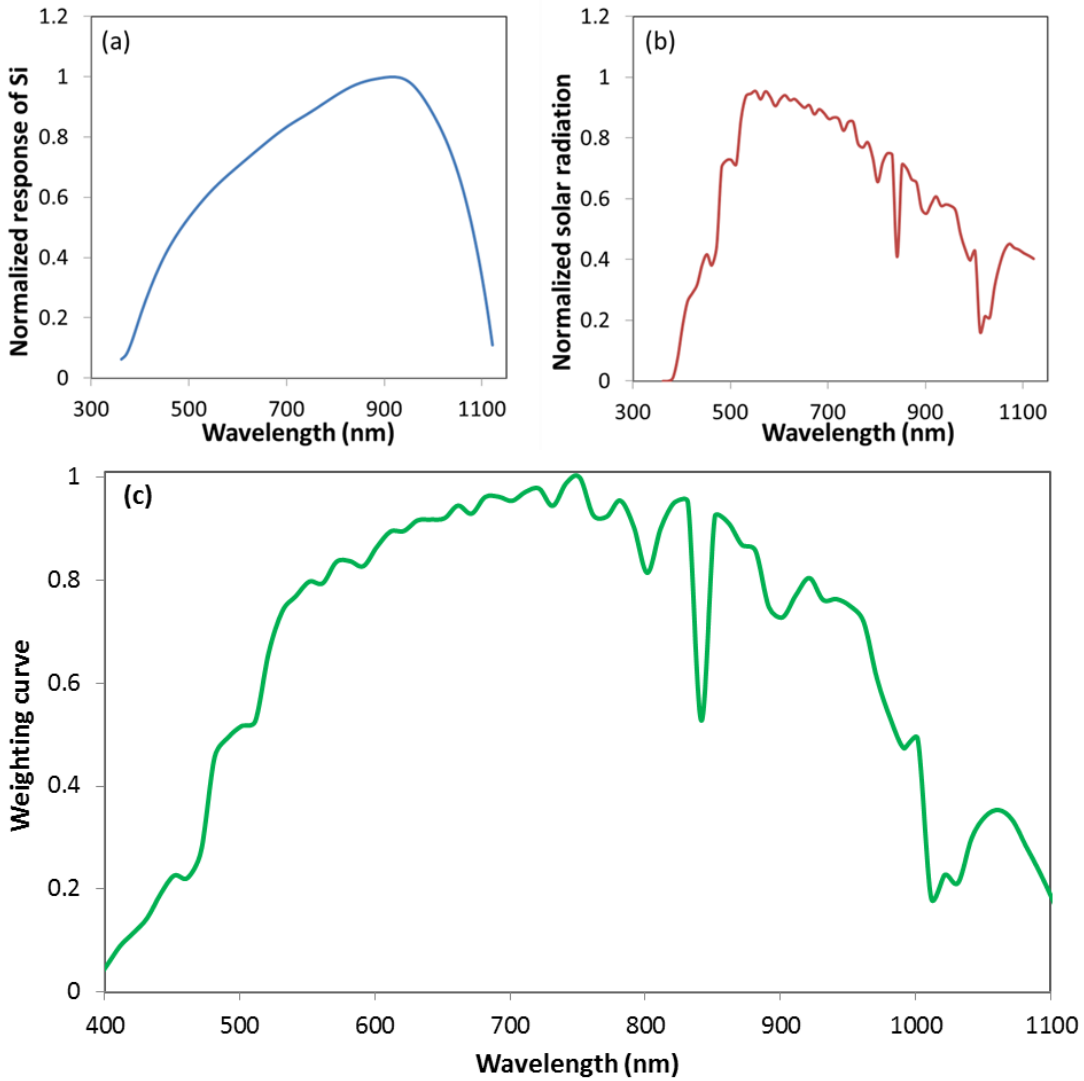

Fig.3.9. Spectral distribution of the normalized response of Si solar cells obtained from the National Renewable Energy Center (a), the normalized solar radiation (b) and the product between both curves, which is the weighting curve used in this work to calculate the average reflectance of the structures studied for Si solar cell applications.

2. FABRICATION OF PERIODIC NANOSTRUCTURES

Many types of nanostructures are fabricated in this work following different procedures with two main techniques in common: laser interference lithography (LIL) used to create the periodic structures on a photosensitive material and reactive ion etching (RIE) used to transfer the structure from the photosensitive material to the substrate. This section details the materials, equipment and implemented processes. Specific methods are also presented in the results section (chapter 4).

2.1. MATERIALS

Two types of crystalline silicon (c-Si) substrates were used as the starting material in this work: one side polished 550 µm thickness, 100 mm diameter circular wafers and unpolished 200 µm thickness, 156 mm x 156 mm square substrates.

The first step in the fabrication process is the cleaning of the substrates by immersion in a piranha solution. This is a mixture of sulphuric acid and hydrogen peroxide (3:1) that creates a highly oxidant and exothermic reaction that warms up to 120°C. Piranha is used to remove organic impurities on the substrates. After the cleaning process, some materials are deposited on the substrate to form the initial stack, being a photoresist (PR) always the last layer to deposit.

PRs are commonly organic polymers, whose solubility change when exposed to photons within a certain energy range [18]. This way, the irradiation distribution can be converted into a topographical pattern by the immersion in a developer solution.

In this work, PRs are used to create periodic patterns by LIL as will be explained later. Three different UV light-sensitive PRs are used: positive Sumitomo PFI-88, positive TSMR-iN027 and negative OKHA PS4. As shown in *Fig.3.10*, the difference between them is that, positive PR turns soluble in the developer when exposed to light while negative PR turns insoluble.

The developer is a solution that dilutes the PR regions exposed or unexposed depending on the type of PR. In this work, CD-26 developer is used, which is a 2.4% solution of Tetramethylammonium Hydroxide (TMAH) on water.

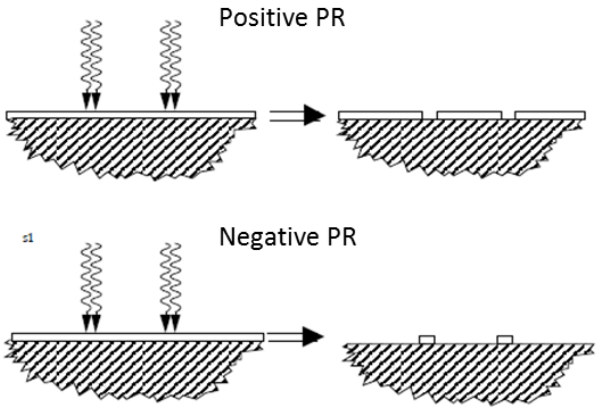

Fig.3.10. Schematic representation of positive and negative photoresists obtained from [18].

Between the substrate and the PR, at least two extra materials are also deposited to form the initial stack [19]: an antireflective coating (ARC, XHRiC-16, Brewer Science, Inc.), and an electron beam (e-beam) evaporated layer of silicon oxide (SiO_x). The purpose of the ARC is to suppress reflection from the substrate during the LIL process. The thickness of this layer is optimized for each case and depends on the complete stack used, particularly on the n and thickness of the different layers; and on the angle of the incident light [18,20]. On the other hand, the SiO_x layer is sandwiched between the PR and the ARC providing high etch rate selectivity [19].

Besides, in some cases, two other materials are used at different stages to improve the transference of the pattern from the PR to the Si: Chromium (Cr) (Testbourne) and hydrogen silsesquioxane (HSQ, Dow Corning).

2.2. DEPOSITION TECHNIQUES

In this work, two different deposition techniques are used. On the one hand, e-beam evaporation is used to deposit layers of hard materials like SiO_x and Cr. The evaporation occurs in a vacuum chamber where DC voltage is applied to a tungsten filament causing electron excitation. An electric field is applied to accelerate the electrons and a magnetic field to focus the beam on the material to evaporate, which is placed on a crucible in the form of grains. The electron beam makes the atoms from the target to sublimate into the gaseous phase either directly or passing through the intermediate liquid phase. The gaseous atoms then precipitate into solid form, coating everything in the vacuum chamber with a thin layer of material[21]. The whole process

is represented in *Fig.3.11* and the tool used in this work, i.e. a Pfeiffer Classic 5000, in *Fig.3.12*.a.

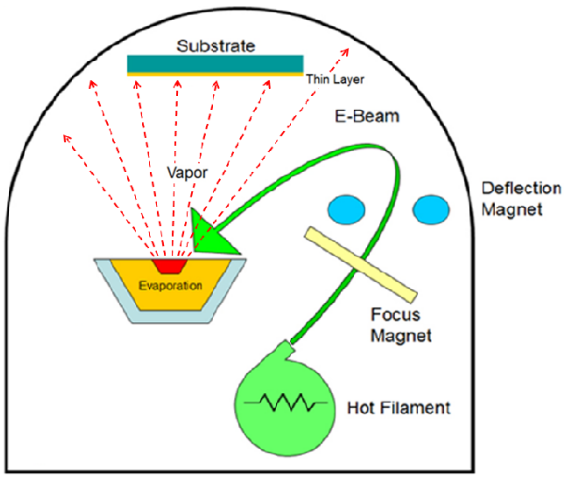

Fig.3.11. Representation of the e-beam evaporation process obtained from [22].

On the other hand, spin coating is used to deposit fluid materials like the PR, ARC and the HSQ. This process produces thin organic films with high uniformity over large areas. In the first step, the material is deposited onto the substrate surface, which is fixed to a rotatory rod by vacuum. Then, the substrate is accelerated up to a desired rotation speed and then it is rotated at this constant rate to thin the fluid. Fluid viscosity, spin speed and rotation time define the thickness of the deposited layer. Finally, the deposited film is dried in a hot plate to eliminate excess of solvents [23][24]. This dried step is especially important in the case of the PR because it can affect their sensitivity to light exposure [18]. The spin coater used in this work is the Laurel WS-650S-6NPP-Lite Single Wafer Spin processor presented in *Fig.3.12*.b.

(a) (b)

Fig.3.12. Deposition tools used: (a) spin coater and (b) e-beam evaporator.

2.3. LASER INTERFERENCE LITHOGRAPHY

LIL is a method for fabricating periodic patterns over large areas [25]. LIL is a conceptually simple process where two or more coherent laser beams interfere to produce a standing wave, which is recorded on a PR.

In this work, LIL is carried out using two different interferometers: a Mach-Zehnder (MZ) and, in most of the cases, a Lloyd´s mirror (LM). In both schemes, two coherent laser beams coming from a helium-cadmium source with 325 nm of wavelength and 300 mm of coherence, interfere forming a grating pattern. More complex patterns, such as square or hexagonal grids can be formed by multiple exposures.

2.3.1. Coherent two beam interference

As shown in *Fig.3.13*, two overlapping coherent plane waves produce a standing-wave interference pattern whose fringes have a periodicity (p), which is determined by the wavelength (λ) and the half-angle between the two plane waves (θ). Assuming plane waves, the electric fields of the two beams of *Fig.3.13*, arriving to a point from two different directions can be expressed as [26]:

$$\overrightarrow{E_1} = \hat{e}_1 E_1 e^{i(\vec{k}_1 \cdot \vec{r} - \omega t)} \tag{3.16}$$

$$\overrightarrow{E_2} = \hat{e}_2 E_2 e^{i(\vec{k}_2 \cdot \vec{r} - \omega t + \phi(t))} \tag{3.17}$$

where $\hat{e}_1$ and $\hat{e}_2$ are unit vectors pointing in the polarization direction, E_1 and E_2 the field amplitudes, k is the wave number ($k = 2\pi/\lambda$), and $\phi(t)$ is a relative phase shift random in time.

The electric field of the interference is the sum of the two components in Equations (3.16) and (3.17) so its intensity can be expressed as follows [27]:

$$I \propto (\overrightarrow{E_1} + \overrightarrow{E_2}) \cdot (\overrightarrow{E_1}^* + \overrightarrow{E_2}^*) \tag{3.18}$$

$$I \propto {E_1}^2 + {E_2}^2 + 2E_1 E_2 \hat{e}_1 \cdot \hat{e}_2 \cos\left(2\pi x \cdot \frac{2\sin\theta}{\lambda} + \phi(t)\right) \tag{3.19}$$

The periodicity of the intensity can be deduced examining the argument of the cosine term in equation (3.19) as:

$$p = \frac{\lambda}{2\sin\theta} \tag{3.20}$$

Therefore, according to equation (3.20) and the laser wavelength of the source used (325 nm), the smallest period achievable in this work is 162.5 nm.

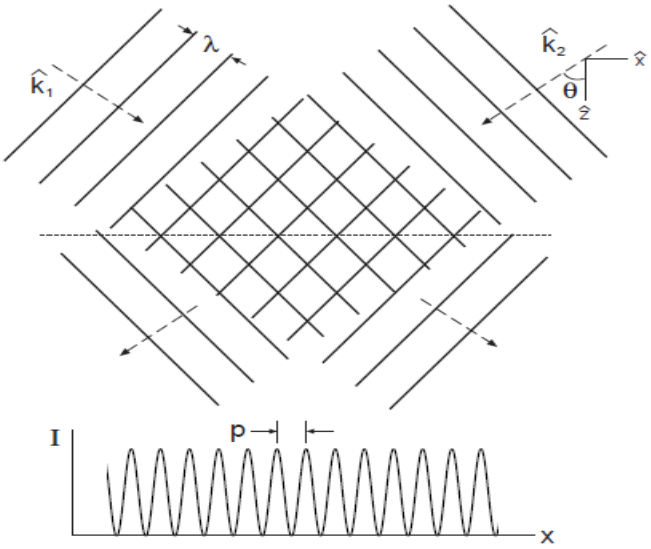

Fig.3.13. Two interfering coherent beams and the resulting standing wave. Image reprinted from [26].

However, two-beam coherent interference does not necessarily imply stationary fringes with a period given by equation (3.20). *Fig.3.13* shows fringes with nodes whose amplitude is zero. To achieve such high-contrast fringes three requirements must be met: the intensity of the two arms must be identical (${E_1}^2 = {E_2}^2$); the phase $\phi(t)$ must be independent of time and the polarization of the two beams must be TE so that $\hat{e}_1 \cdot \hat{e}_2 = 1$, independent of the angle [26].

2.3.2. Mach-Zehnder Interferometer

The MZ interferometer is schematically represented in *Fig.3.14*. This configuration uses one laser source which output is divided into two different beams using a beam-splitter. Then, each beam is redirected to the substrate with two different mirrors. Prior to the interference, both beams are focused with two spatial filters composed by a lens and a pinhole. The spatial filters produce spherical wavefronts if the diameter of their pinholes is equal to, or less than, the diffraction-limited spot size of the lenses [18]. The gratings produced are not linear since the waves are spherical. However, by making the distance from the pinhole to the substrate large enough, it is possible to reduce the deviation from linearity [28,29].

The MZ also has a feedback system, formed by a beam-splitter, two detectors and a feedback loop, that stabilizes the interference pattern against environmental perturbations such as air turbulence and vibrations [30].

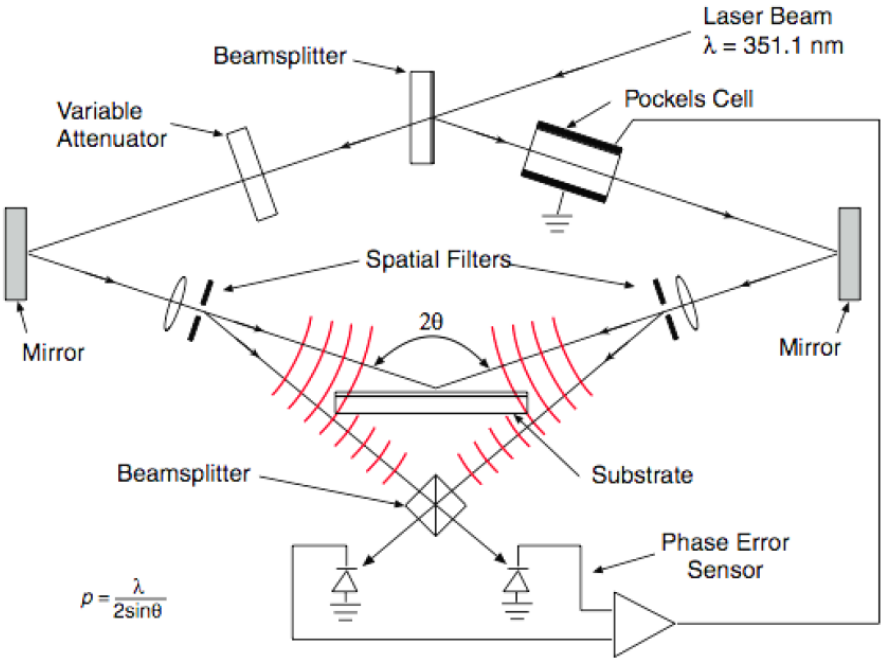

Fig.3.14. Mach-Zehnder configuration for laser interference lithography.

In this work, we use the MZ interferometer at the Nanostructures Laboratory (NSL) in the Massachusetts Institute of Technology (MIT). A picture of the set-up is shown in *Fig.3.15*.

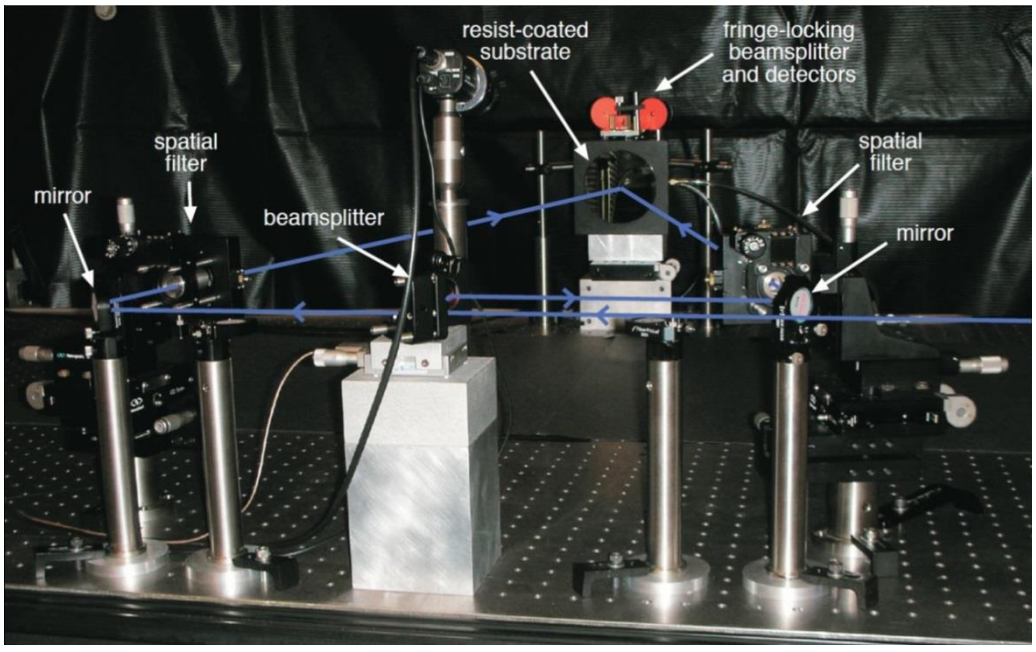

Fig.3.15. Mach-Zehnder interferometer.

2.3.3. Lloyd´s Mirror Interferometer

The schematic representation of LM configuration is shown in *Fig.3.16.* As it happens in the MZ, the LM creates the interference pattern from a single point laser source. The laser beam is guided with a set of mirrors to the spatial filter, which is located two meters distant from the substrate. The substrate is placed normal to a mirror on a rigid frame. In this way, half of the beam is first reflected from the mirror prior to interfering with the other half at the substrate surface. The substrate and the mirror are mounted on a rotation stage that allows us to choose the period of the interference pattern.

The angle of rotation of the stage, i.e. the angle between the laser beam and the mirror, and the length of the mirror, determine the size of the nanostructured area. This can be seen schematically represented in *Fig.3. 17*. If either the angle (θ) or the length of the mirror (M_L) decrease, the nanostructured length (L) is reduced too. According to that scheme, the resulted nanostructured length is given by:

$$L = M_L \cdot \tan\theta \qquad (3.21)$$

where θ depends on the period and the wavelength of the light as expressed in equation (3.20).

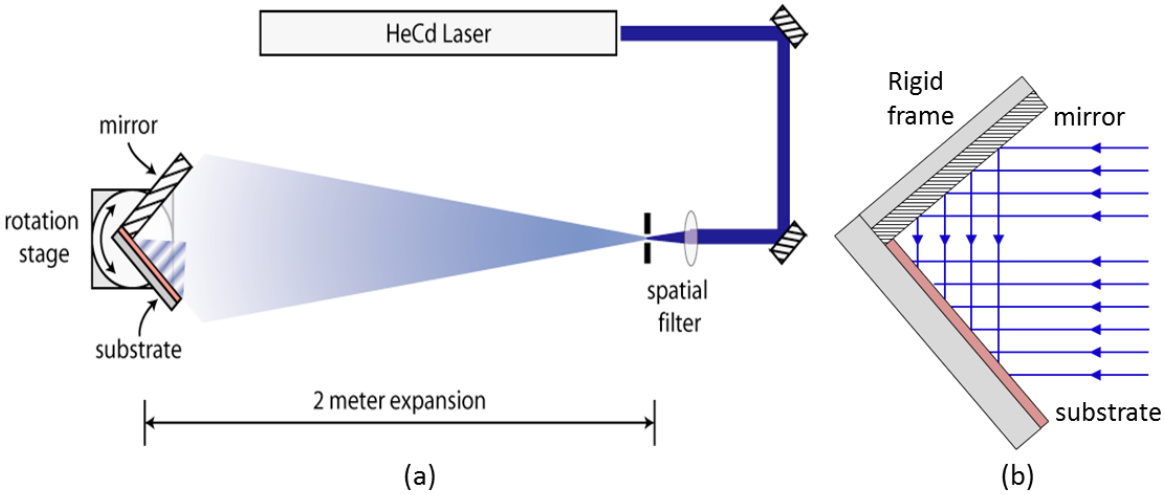

Fig.3.16. Schematic representation of the Lloyd´s mirror interferometer: complete set-up (a) and detail of the interference between the direct and the reflected beams at the substrate (b).

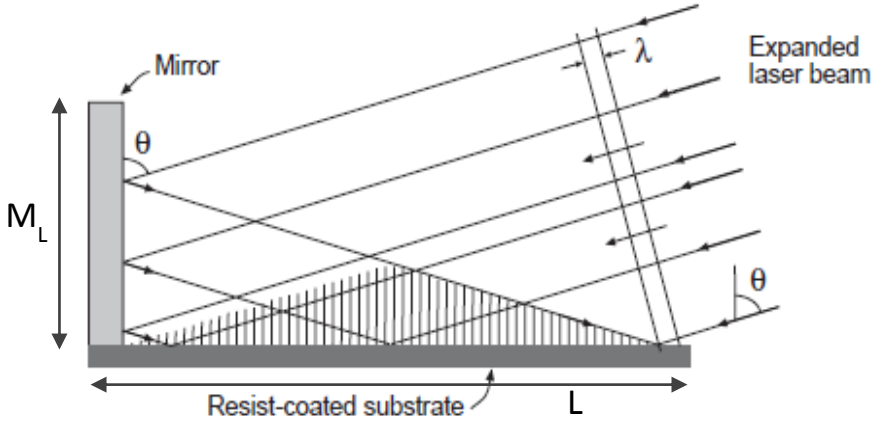

Fig.3. 17. Detailed representation of the interference in a Lloyd´s mirror reprinted from [26].

Two different LM interferometers with the same configuration are used in this work: one in NSL at MIT and the other in FideNa and later in CEMITEC.

2.4. REACTIVE ION ETCHING

RIE is used to transfer the pattern recorded on the PR to the layers underneath. The process uses a chemically reactive plasma to remove material from the sample [31] (*Fig.3.18*). In this work, the etching is done using a periodic patterned mask of a hard material which leaves some holes over the target material.

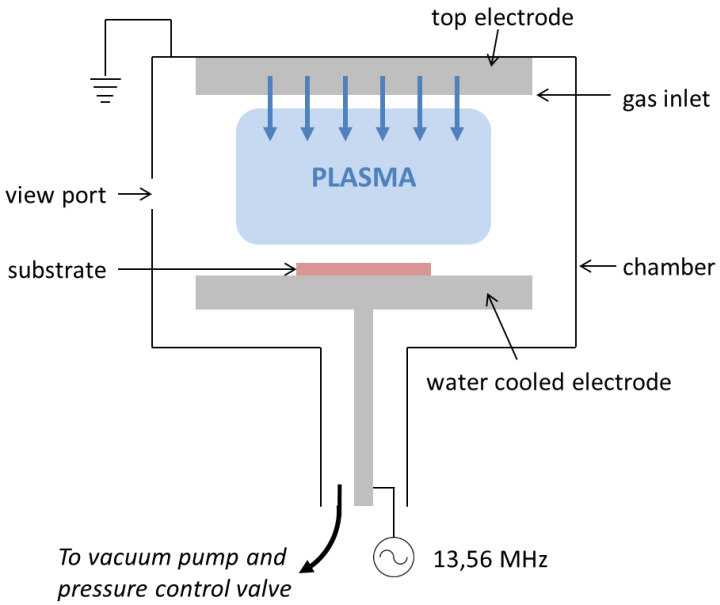

Fig.3.18. Schematic representation of a reactive ion etching chamber.

The process takes place in a vacuum chamber, which has a wafer platter in the bottom between two electrodes. Gas enters through small inlets at the top of the chamber and

exits to the vacuum pump system through the bottom. A RF powered electromagnetic field ionizes the gas creating the plasma. Then, a voltage difference (DC bias) is created, making the active ions to drift from the plasma toward the wafer platter, where they collide with the sample knocking of some material by transferring part of their kinetic energy (physical etching). Besides, the radicals react chemically with the materials on the surface of the sample (chemical etching). Etching characteristics in a RIE system depend on which kind of etching (chemical or physical) dominates over the other.

Different process parameters allow us to control the etching characteristics:

- Type of gas. In this work the gases used are Oxygen (O_2), Helium (He), Tetrafluoromethane (CF_4) and Hydrobromic acid (HBr).
- Gas flow. This is normally set at 20 sccm.
- Chamber pressure. The typical value used is 10 mTorr.
- RF power. This is varied between 50 and 200 W depending on the materials to etch and the desired profile.
- DC bias: This parameter depends directly on the RF power and the chamber pressure, which can be set by the user. Typical values can be between a few volts and some hundreds of volts.
- Etching time. The time can be less than 1 minute or more than one hour.

Adjusting the above parameters it is possible to control important etching parameters such as the etch rate, the directionality and the selectivity [32,33]. The etch rate depends on the power almost linearly. Therefore, knowing this parameter, it is easy to control the depth of the etching varying the time of the process while maintaining the rest of the parameters.

The directionality is the degree of isotropy or anisotropy of the etching. This depends on whether the chemical or the physical etching is dominating the process. Normally, chemical etching is more isotropic than physical etching which can achieve almost vertical sidewalls. The directionality depends on the ion bombardment produced by the DC bias and the chemical reactivity of the gas and the material used.

The selectivity is the ratio of the etch rate of the target material to the etch rate of other materials present in the sample. This depends on the nature of the materials and the gases and on the DC bias which is directly related to the power and the pressure. The selectivity is an important parameter to consider in order to choose an appropriate mask for a particular material.

2.5. LIFT-OFF PROCESS

Lift-off is a technique to create nanostructures in a target material from the inverse nanostructure in a sacrificial layer, typically a resist [34]. The process is sketched in *Fig.3.19*. The starting point of the process is a resist pattern on top of a substrate. The first step consists in depositing a material on the pattern so it fills the holes in the resist. Then, the resist is chemically removed and the negative of the initial pattern on the deposited material remains on the substrate.

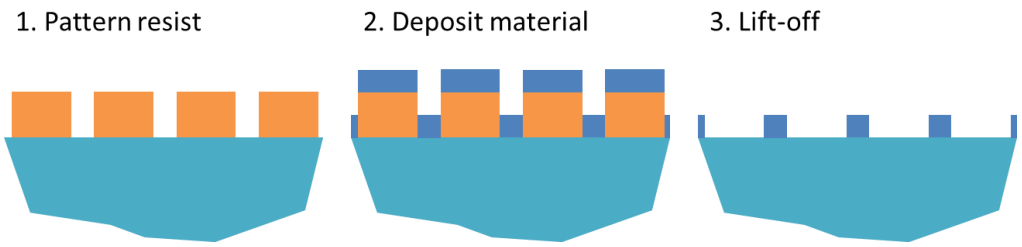

Fig.3.19. Basic elements of the lift-off process.

Lift-off is used in this work to obtain patterns on Cr that are used as hard masks in subsequent deep transfer processes.

3. CHARACTERIZATION OF NANOSTRUCTURES

3.1 PROFILOMETER

A profilometer is an instrument used to characterize the topography of a sample. In this work, the profilometer quantifies the roughness of the substrates as well as to measure the layer thickness of different deposited materials such as ARC, PRs, Cr and SiO_2. The tool used is a Bruker DektakXT like the one shown in *Fig.3.20*. It is a contact profilometer with a diamond stylus, which is placed vertically in contact with the sample and then moved laterally across the sample for a specified distance, time and

contact force. The tool measures small variations in vertical stylus displacement as a function of position.

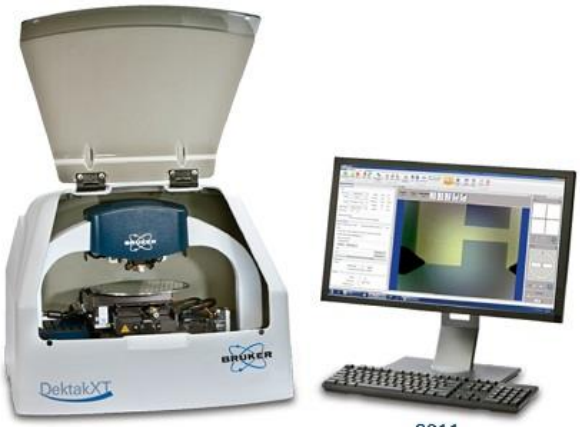

Fig.3.20. Profilometer used in this work.

3.2 SCANNING ELECTRON MICROSCOPE

The scanning electron microscopy (SEM) is the characterization tool used in this work along the fabrication processes to check the results after every single step. The tool used is a Zeiss UltraPlus like the one in *Fig.3.21*.

Fig.3.21. SEM used in this work.

Basically, the SEM produces images of a sample by scanning it with a focused beam of electrons. The electrons interact with atoms in the sample producing signals that are detected and contain information about the topography and composition of the

sample. These signals are used in combination with the information of the beam position to create an image.

3.3 SPECTROPHOTOMETER

A spectrophotometer is a tool to quantitatively measure the reflectance or transmittance of a sample. In this work, the equipment used is the JASCO V-670 shown in *Fig.3.22*. With this spectrophotometer it is possible to measure the absorption spectrum of a sample over a wavelength range of 190 to 2700 nm. It consist of two different light sources (one for Ultraviolet and visible light and the other for near infrared) and a set of mirrors to direct the light through a window to reach the sample. Two different paths are possible: one is reserved for the references provided with the tool (usually mirrors with a known response) and the other for the samples being characterized. After the samples, there are a set of mirrors to direct the beam to two detectors (again, one for Ultraviolet and visible light and the other for near infrared).

Fig.3.22. Spectrophotometer used in this work.

In this work, the spectrophotometer is used together with an integrating sphere (JASCO ISN-723), which is an optical component consisting in a hollow spherical cavity covered with a diffuse reflective material with a uniform scattering effect. The operating principle is represented in *Fig.3.23*: light rays incident on any point on the inner surface are, by multiple scattering reflections, distributed equally to all other points. In that way, a single point detector is enough to calculate the total amount of light in the sphere. This is used to characterize the total reflectance of the samples including direct and diffuse components.

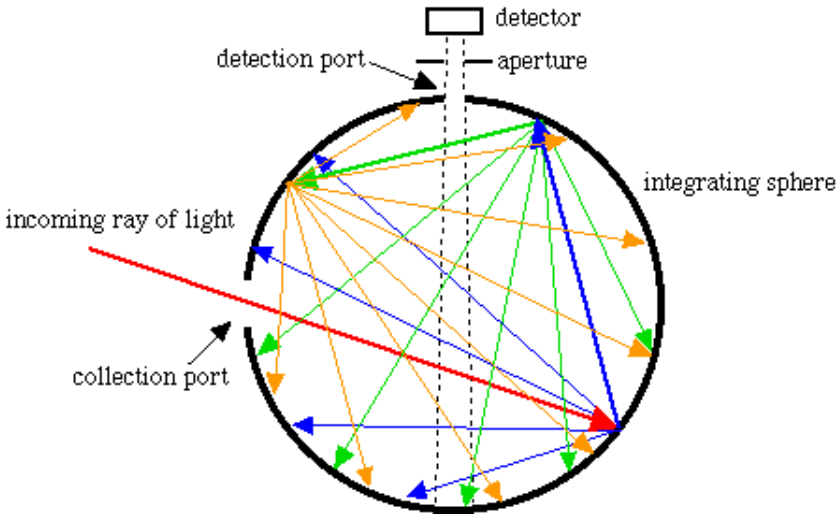

Fig.3.23. Schematic representation of an integrating sphere.

4. SOLAR CELL INTEGRATION

The nanostructured substrates are integrated in solar cells at CENER following a conventional process like the one schematically represented in *Fig.3.24*. Normally, before this process, the surface is chemically etched to remove the saw damage and a sodium hydroxide (NaOH) texturing process is used to create the antireflection micro-inverted pyramids at the surface. In this case, prior to the process of *Fig.3.24*, the nanostructures are created following the process explained in the previous section.

The solar cell integration starts with a surface cleaning step (step 2 in *Fig.3.24*) and then, the substrate is heated in a furnace with a phosphorous based gas to create the emitter via diffusion (step 2 in the figure). This process generates a layer of phosphor silicate glass (PSG) on top of the substrate, which is then removed with hydrofluoric acid (HF) (step 3 of *Fig.3.24*).

After this, a layer of silicon nitride (SiNx) is deposited by plasma-enhanced chemical vapor deposition (PECVD) (step 4 of *Fig.3.24*). This process deposits a thin film on a substrate from a material in gas state. The process occurs in a chamber where the reacting gas is placed between two electrodes. A DC voltage is applied creating plasma with the gas. Then, this plasma reacts with the substrate forming a thin film on its surface [34]. The SiN_x layer is used to passivate the surface, i.e. reduce the recombination of the electron-hole pairs created in the p-n junction (see Chapter 1).

Besides, the SiN_x reduces the reflectance of the surface due to its intermediate n between air and Si.

Finally, the metal contacts of the cell are created in two steps: first, a metal paste is deposited by screen printing at the pace where the bursbars and finger gridlines will be formed (step 4 of *Fig.3.24*). This paste is then heated (fired) (step 6 of *Fig.3.24*) so that it melts through the SiN_x layer to effectively make electrical contact with the underlying Si.

The performance of the solar cells is tested, also in CENER, with different techniques: I-V curve at standard test conditions (STC), external and internal quantum efficiency (EQE and IQE) and electroluminescence image (EL).

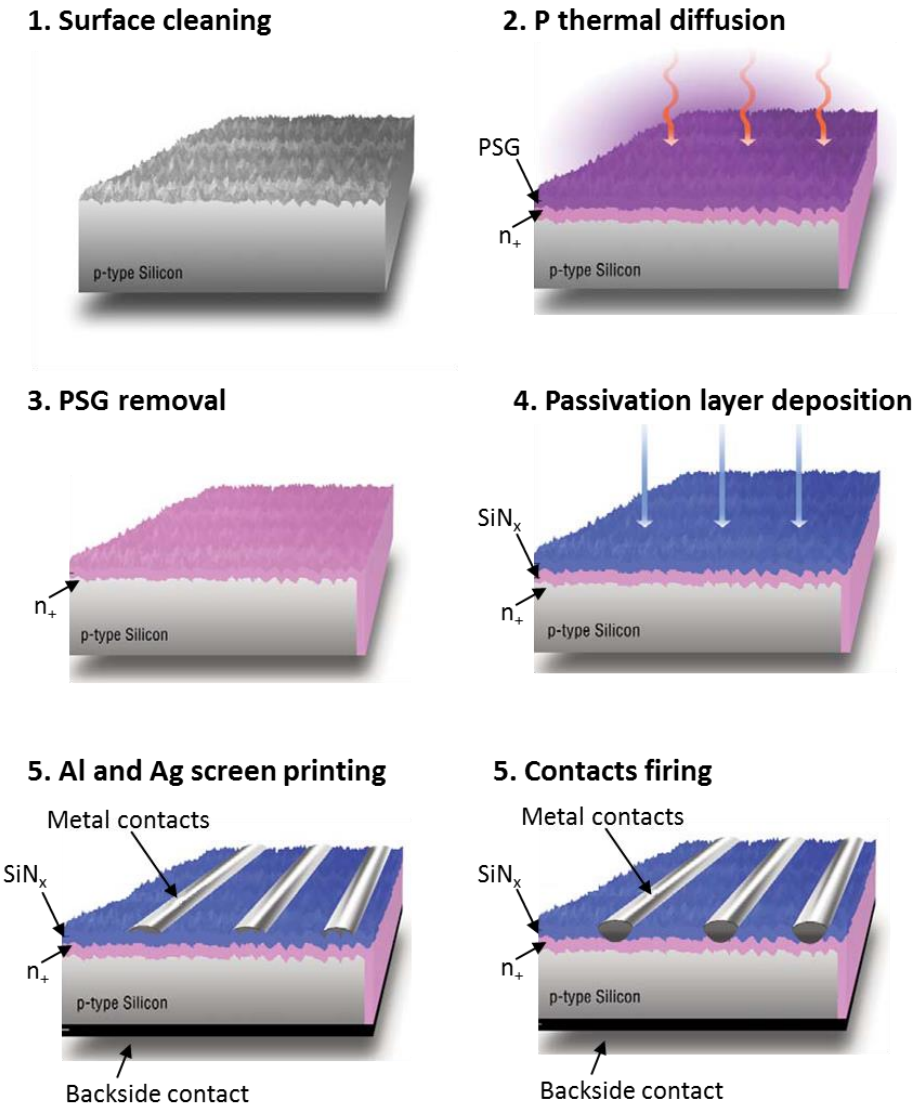

Fig.3.24. Solar cells integration process followed in this work.

5. REFERENCES

[1] "Training in Midlothian." [Online]. Available: http://www.training-classes.com/programs/05/73/57320_design_of_experiments_doe.php. [Accessed: 24-Nov-2014].

[2] L.F. Alvarez, "DESIGN OPTIMIZATION BASED ON GENETIC PROGRAMMING."

[3] P. Sahoo, T. Barman, and J. P. Davim, *Fractal Analysis in Machining*. Springer Science & Business Media, 2011.

[4] A. Taflove, *Computational Electrodynamics: The Finite-Difference Time-Domain Method, Third Edition*, 3 edition. Boston: Artech House, 2005.

[5] K. S. Kunz and R. J. Luebbers, *The Finite Difference Time Domain Method for Electromagnetics*. CRC Press, 1993.

[6] K. Han and C.-H. Chang, "Numerical Modeling of Sub-Wavelength Anti-Reflective Structures for Solar Module Applications," *Nanomaterials*, vol. 4, no. 1, pp. 87–128, Jan. 2014.

[7] "OptiFDTD 10 Technical Background and Tutorials," *Optiwave*. .

[8] F. W. L. Kung, "Modeling Of Electromagnetic Wave Propagation In Printed Circuit Board And Related Structures," phd, Multimedia University, 2003.

[9] K. Yee, "Numerical solution of initial boundary value problems involving maxwell's equations in isotropic media," *IEEE Trans. Antennas Propag.*, vol. 14, no. 3, pp. 302–307, May 1966.

[10] J. Krc and M. Topic, *Optical Modeling and Simulation of Thin-Film Photovoltaic Devices*. CRC Press, 2013.

[11] L. N. Trefethen, *Finite Difference and Spectral Methods for Ordinary and Partial Differential Equations*. Cornell University, [Department of Computer Science and Center for Applied Mathematics], 1996.

[12] S. Obayya, *Computational Photonics*. John Wiley & Sons, 2011.

[13] S. d. Gedney, "An anisotropic perfectly matched layer-absorbing medium for the truncation of FDTD lattices," *IEEE Trans. Antennas Propag.*, vol. 44, no. 12, pp. 1630–1639, Dec. 1996.

[14] S. Tanev, D. Feng, S. Dods, V. P. Tzolov, Z. J. Jakubczyk, C. Chen, P. Berini, C. A. Waechter, H. F. Pinheiro, A. P. L. Barbero, and H. E. Hernandez-Figueroa, "Advances in the development of simulation tools for integrated optics devices: FDTD, BPM, and mode-solving techniques," 2001, vol. 4277, pp. 1–20.

[15] Charles Kittel-8th Edition, *Introduction to Solid State Physics*. .

[16] R. C. Dorf, *The Electrical Engineering Handbook*. Urban Media Comics, 1993.

[17] R. Courant, K. Friedrichs, and H. Lewy, "On the Partial Difference Equations of Mathematical Physics," *IBM J Res Dev*, vol. 11, no. 2, pp. 215–234, Mar. 1967.

[18] H. Smith and K. Berggren, "Draft of book manuscript, 'Nanostructure Fabrication.'" .

[19] T. A. Savas, M. L. Schattenburg, J. M. Carter, and H. I. Smith, "Large-area achromatic interferometric lithography for 100 nm period gratings and grids," *J. Vac. Sci. Technol. B*, vol. 14, no. 6, pp. 4167–4170, Nov. 1996.

[20] K. Hehl and W. Wesch, "Calculation of optical reflection and transmission coefficients of a multi-layer system," *Phys. Status Solidi A*, vol. 58, no. 1, pp. 181–188, Mar. 1980.

[21] S. Kumar, J. Singh, and J. Akhtar, "Materials and Processing for Gate Dielectrics on Silicon Carbide (SiC) Surface," in *Physics and Technology of Silicon Carbide Devices*, Y. Hijikata, Ed. InTech, 2012.

[22] M. Nicholson, "Constant Current Control in Industrial Deposition," *Industrial Power Supplies*. .

[23] L. E. Scriven, "Physics and Applications of DIP Coating and Spin Coating," in *Symposium H – Better Ceramics Through Chemistry III*, 1988, vol. 121.

[24] "Spin-Coating Test No. - Uni-kiel.de Pdf - Ebooks Pdf Download." [Online]. http://ebookall.biz/view/ebook/aHR0cDovL3d3dy50Zi51bmkta2llbC5kZS9jbWEvbTEwMl9zcGluX2NvYXRpbmcucGRmW2J3bl1TcGluLUNvYXRpbmcgVGVzdCBOby4gLSBVbmkta2llbC5kZQ. [Accessed: 25-Sep-2014].

[25] "1 Nanostructures Technology, Research and Applications 1 ...," *yumpu.com*. [Online]. Available: https://www.yumpu.com/en/document/view/25798861/1-nanostructures-technology-research-and-applications-1-. [Accessed: 25-Sep-2014].

[26] T. A. Savas, "Achromatic Interface Lithography," PhD dissertation, Physics, Massachusetts Institute of Technology, 2002.

[27] R. Serway and J. Jewett, *Physics for Scientists and Engineers*. Cengage Learning, 2012.

[28] E. H. Anderson, "Fabrication and electromagnetic applications of periodic nanostructures," Thesis, Massachusetts Institute of Technology, 1988.

[29] J. Ferrera, M. L. Schattenburg, and H. I. Smith, "Analysis of distortion in interferometric lithography," *J. Vac. Sci. Technol. B Microelectron. Nanometer Struct.*, vol. 14, no. 6, pp. 4009–4013, Nov. 1996.

[30] H. I. Smith, "Fabrication techniques for surface-acoustic-wave and thin-film optical devices," *Proc. IEEE*, vol. 62, pp. 1361–1387, Oct. 1974.

[31] W. Lu, *Fabrication and Characterization of a Double Torsional Mechanical Oscillator and Its Applications in Gold Micromass Measurements*. ProQuest, 2008.

[32] K. S. Chuah, "Inductively coupled plasma dry etching process on planar lightwave circuit fabrication / Chuah Khoon Seah," masters, University of Malaya, 2010.

[33] F. Li, A. Nathan, Y. Wu, and B. S. Ong, *Organic Thin Film Transistor Integration: A Hybrid Approach*. John Wiley & Sons, 2011.

[34] C. T. Reviews, *e-Study Guide for: Fundamentals of Modern Manufacturing : Materials, Processes, and Systems: Business, Business*. Cram101 Textbook Reviews, 2012.

CHAPTER 4. RESULTS AND DISCUSSION

1. DESIGN AND FABRICATION OF PHOTONIC CRYSTALS FOR SOLAR CELLS

An important objective of this work is the improvement of the light absorption in bulk silicon (Si) solar cells by means of periodic nanostructures or photonic crystals (PCs). This implies the optimization of the PCs, their fabrication on Si substrates and the subsequent integration of solar cells on these nanostructured substrates.

In this section we present the results of the optimization and fabrication of PCs on polished Si substrates.

1.1 INITIAL OPTIMIZATION PROCESS

The first optimization process is done attending to optical aspects and our fabrication capacities. The idea is to find the optimum nanostructure that can be fabricated with our facilities and tools to improve Si absorption according the spectral efficiency of bulk Si solar cells and the solar irradiated spectrum (see Chapter 2).

The optimization starts with the identification of the different feasible PCs, the variable dimensions in their geometry and the reasonable ranges of variation for these dimensions. Then, the dimensions of each PC are optimized in the selected ranges by using a design of experiments (DOE) and computer simulation as explained in chapter 3. Finally, the reflectivity of all the optimized PCs is computed to decide which one is the best.

1.1.1. Feasible PCs with our fabrication process

As said before, the design of PCs has been done attending to the possibilities of our fabrication tools. Therefore, we have first analyzed the different steps of the typical fabrication process to identify the feasible geometries.

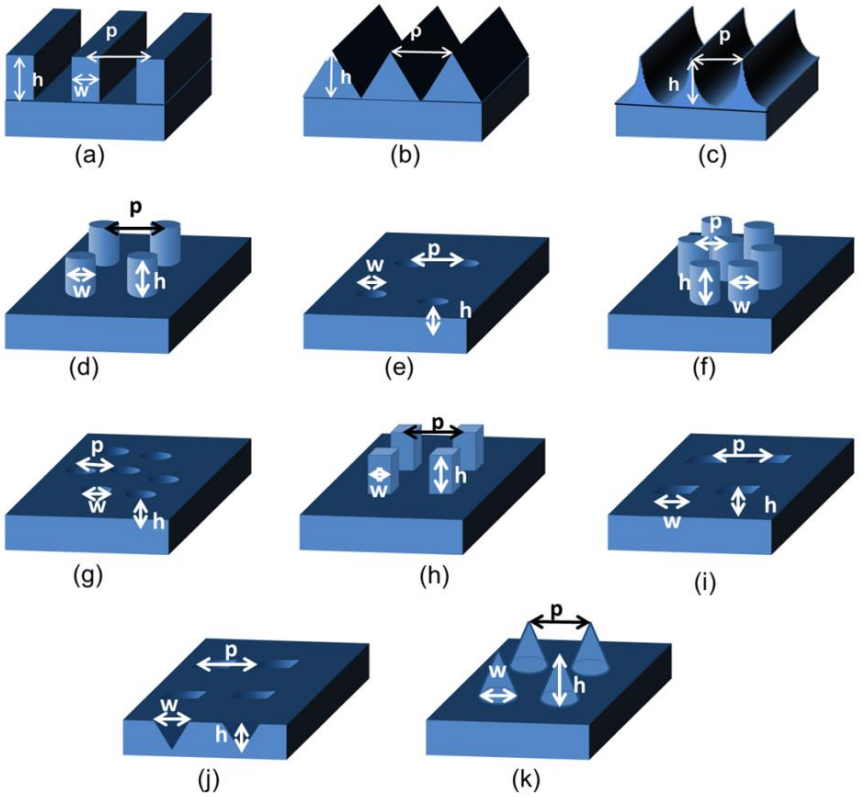

Fig.4.1. Different geometries considered in the PC optimization work.

First, the laser interference lithography (LIL) process allows the fabrication of 1D or 2D periodic nanostructures. One single exposure with the Lloyd´s Mirror (LM) produces a pattern of lines on photoresist (PR). Therefore, for 1D structures, the only possible variability will be given by the transfer process, which is typically carried out by reactive ion etching (RIE) and sometimes combined with wet etching or lift-off.

The typical transfer profile obtained by RIE is vertical but also omnidirectional or oblique etchings can be obtained by adjusting the process parameters. Wet etching also allows us to obtain oblique and omnidirectional etching by choosing the appropriate chemicals. According to this, we have defined three different profiles for the 1D structure: rectangular, triangular and circular (a, b and c in *Fig.4.1* respectively).

In the case of 2D structures, there is more diversity of possible patterns. First, depending on the angle between the two exposures with the LM, two different lattices can be obtained: a square lattice for an angle between exposures of 90° and a hexagonal lattice for an angle of exposure of 60°. The schematic explanation of this is shown in *Fig.4.2*. When the two beams coming to the sample are orthogonal, the resulted interference is a square lattice of points. Otherwise, when the angle between

the two beams is 60° the periodic pattern is repeated in a hexagonal lattice. Despite the ideal interference represented in the figure, in the real samples, the corners tend to be round so we obtain circles in the orthogonal case and ovals in the hexagonal one.

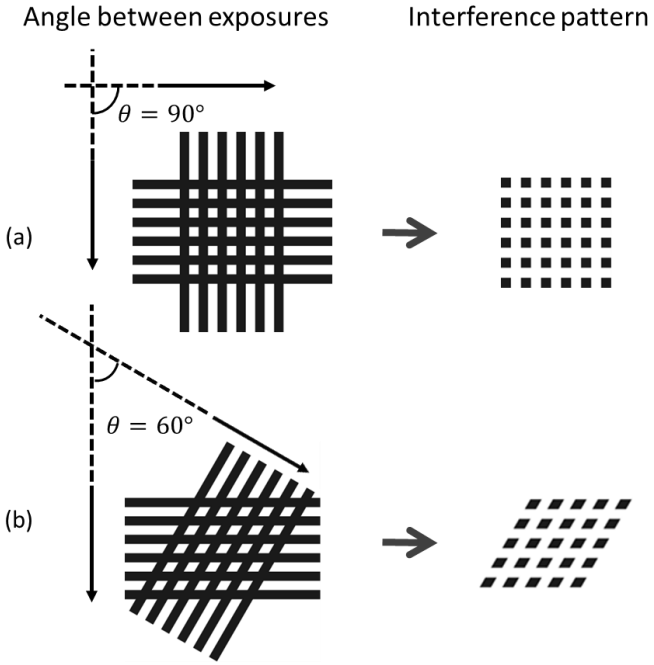

Fig.4.2. Two different distributions for the 2D periodic patterns feasible with the Lloyd´s Mirror in a double exposition: a square lattice obtained with a 90° rotation of the sample between exposures and a hexagonal lattice obtained with 60° of rotation between exposures (b).

Besides, the type of PR used defines whether the final pattern is formed by pillars or holes. With this considerations and assuming vertical etching from the PR to de Si, we obtain four different designs: pillars in square lattice, holes in square lattice, pillars in hexagonal lattice and holes in hexagonal lattice (structures d, e, f and g in *Fig.4.1*).

Moreover, starting from the circular pillars in square lattice on the PR, if we suppose oblique etching, which is also achievable with the RIE, we can obtain a pattern of cones in square lattice (structure k in *Fig.4.1*). Since the posts in hexagonal lattice (structure f in *Fig.4.1*) have not circular shape it is more difficult to obtain cones in this lattice so it was discarded. Also, starting from holes it is possible to obtain oblique etching. However, in this case it is easier to do it by wet etching with potassium hydroxide (KOH). In this process, the etching occurs following the crystalline orientation of Si resulting in a pattern of inverted pyramids (structure j in *Fig.4.1*).

Finally, we have included the square shape for the pillars and holes in square lattice obtaining the structures h and i in *Fig.4.1*. This is also feasible with our tools but

increasing considerably the number of fabrication steps. In this case, the process is considered as a double 1D PC fabrication process, i.e. we start with a pattern of lines on PR, we transfer it to the underneath layers, then we deposit PR again and repeat the process creating an orthogonal pattern of lines.

1.1.2. PCs dimensions and variation ranges

We have kept the study to the 11 structures above mentioned and summarized in *Fig.4.1*, avoiding more complicated processes. For each one of these structures, we have identified the different variable parameters that need to be optimized. In general, there are three parameters to take into account: the period (p), the height (h) and the width of the motifs (w), i.e. the linewidth in the 1D case and de diameter or side-width in the 2D case. However, in some cases, these parameters are mutually dependent so two parameters determine the third one or even just one parameter determines the other two. In these particular cases only two or one parameters need to be considered. This will be explained in detail for each structure in the following subsections.

Once the variable parameters have been identified, we can define, for each parameter, a possible range of variation according, again, with our fabrication processes. For example, the height is limited by the RIE process. Although the RIE parameters can be optimized to achieve higher structures, in this section, we have defined 300 nm as the upper limit to keep the fabrication process in comfortable values. The lower limit for the height has been set to 10 nm. In the case of the period it is determined by the LM, having a theoretical lower limit of 162.5 nm. The top limit is given by the decrease in the patterned area with the increase of the period. We have set 800 nm as the largest possible period, which gives a patterned area of 3 cm x 3 cm, with the wavelength of our laser (325 nm) and the length of our mirror (15 cm). We have considered that smaller areas, i.e. larger periods, are not convenient for the solar cell application. Finally, in the case of the size of the motifs, the limits are given again by the LIL process. The lower and upper reasonable values are the 20% and the 80% of the period respectively. Therefore, we have defined the range of variation of the width between 30 and 640 nm to study the situations of 80% of the higher period and the 20% of the theoretical smaller period.

With all the parameters and their variation ranges identified, we define a 3-level central composite design (CCD) (see Chapter 3). In the general case of three variables, it gives 15 combinations of parameters (period, width and height) to be simulated. The design does not take into account the dependence between width and period and can give unfeasible structures. In our case, the DOE have four runs with width bigger than the period, which are treated as flat Si. This implies a loss of information in the DOE to construct the response surface. Consequently, in the most promising structures, we have performed a second DOE with its central point in the optimum obtained in the first one and with a smaller range of variation of the parameters avoiding the overlapping between width and period.

1.1.3. Optimization of PCs

In the following subsections we present the optimization process for every PC defined in the previous sections and summarized in *Fig.4.1*.

1.1.3.1. 1D Rectangular lines (Fig.4.1.a)

In this structure, there are 3 independent variable parameters: the period (p), the linewidth (w) and the height (h). Therefore, a 3-level CCD with 3 variables has been developed. These parameters have been analyzed in the ranges of variation explained in the previous section obtaining the sequence of runs of the DOE summarized in *Table 4.1*. In the case of runs #3, #4, #10 and #13 the linewidth is bigger than the period so the structure is considered as a flat surface. The results of the simulation for all the runs of the DOE are shown in *Fig.4.3*. It can be seen in the graph that all the nanostructures improve the behavior of the flat Si surface (runs #3-4-10-13). The best result is obtained for run #11, whose lowest value under 10% is found at 760 nm.

The output column of *Table 4.1* corresponds to the average weighted reflectance (AWR), obtained as explained in Chapter 3: first, we calculate the reflectance vs wavelength curves by computer simulation, then we multiply each curve by the weighting curve and finally we integrate the result. The AWR is used as output in the response surface method (RSM) to obtain the predictive model, which is summarized in *Table 4.2*.

# run	Period (nm)	Linewidth (nm)	Heigth (nm)	AWR (%)
1	201.35	115.13	68.78	**12.79**
2	201.35	115.13	241.22	**12.90**
3	201.35	364.87	68.78	**12.46**
4	201.35	364.87	241.22	**13.03**
5	498.65	115.13	68.78	**14.93**
6	498.65	115.13	241.22	**13.74**
7	498.65	364.87	68.78	**13.90**
8	498.65	364.87	241.22	**11.22**
9	350	240	155	**8.83**
10	100	240	155	**9.98**
11	600	240	155	**10.22**
12	350	30	155	**13.74**
13	350	450	155	**10.80**
14	350	240	10	**19.59**
15	350	240	300	**11.52**

Table 4.1.DOE 1 for the structure of rectangular lines and the AWR.

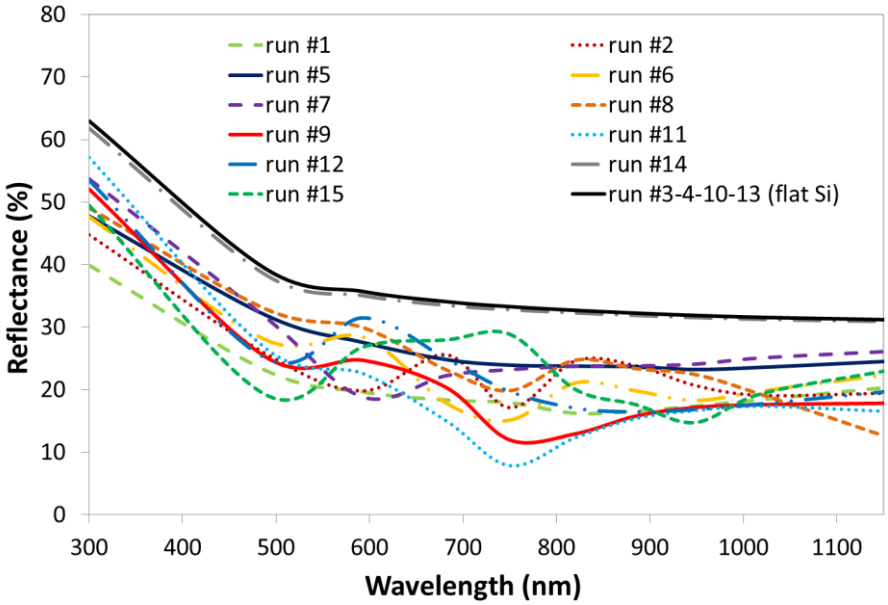

Fig.4.3. Simulated reflectance results for all the runs in the DOE 1 for the structureof rectangular lines.

The model is a sum of factors; each one multiplied by a coefficient. It includes all the main effects (p, w and h), as well as 2-way (pw, ph and hw), 3-way (pwh) and quadratic interactions (pp, ww and hh). Besides, there is information about the significance of every factor in the model with the P-value in *Table 4.2*. The lower the P-value, the more significant the corresponding factor. P-values higher than 0.1 indicate no significance (P-values in black in *Table 4.2*), P-values between 0.1 and 0.05 some

significance (P-values in blue in *Table 4.2*) and P-values under 0.05 indicate high significance (P-values in red in *Table 4.2*).

Model		
Factor	Coeff	P-value
Const	12.96	5.5E-11
p	-1.98	1.5E-03
w	2.49	2.6E-04
h	-1.00	6.3E-02
pw	-2.11	6.1E-03
ph	-0.63	3.4E-01
hw	0.04	9.5E-01
pwh	0.62	3.5E-01
pp	1.39	9.6E-03
ww	1.84	1.5E-03
hh	1.81	1.7E-03

Fitting Indicators	
R^2	8.94E-01
Adj R^2	8.06E-01
Std Error	1.80E+00
F	1.02E+01
Sig F	2.00E-04

Table 4.2. Model for the reflectance of the PC of rectangular lines with DOE 1.

In the table, there are also some parameters that give information about the quality of the model (fit indicators)[1]. R^2 is the coefficient of determination, which is a measure of the fit of the model. It takes values between 0 and 1 where a value of 1 means a perfect fit. The next parameter (Adj R^2) is an adjustment of R^2 but taking into account the number of observations and terms in the model. In this model, we obtain acceptable values of $\mathrm{R}^2 = 8.94 \cdot 10^{-1}$ and $\mathrm{Adj\ R}^2 = 8.06 \cdot 10^{-1}$. The parameter *Std Error* is the standard deviation of the model from the real values of reflectance. The two final parameters indicate if the model is significant for prediction. Values of *F* greater than 6 and *Sig F* lower than 0.05 indicate a significant model for prediction. In this case, the *F* is $1.02 \cdot 10^{1}$ and the *Sig F* is $2 \cdot 10^{-4}$ so the model approximates well enough to the reflectance data.

This model gives an equation for the reflectance dependent on the three variables:

$$R = 12.96 - 1.98p + 2.49w - h - 2.11pw - 0.63ph + 0.04hw + 0.62pwh + 1.39pp + 1.84ww + 1.81hh \quad (4.1)$$

Where *R* is the modeled reflectance and the polynomic terms correspond to the products of the coefficients and factors of the model in *Table 4.2*. Once this model is defined, it is possible to mathematically calculate the values of the parameters at which the reflectance reach its minimum value. For this, is enough to calculate the

derivatives of the equation (1) with respect the three variables and make them to be equal to zero:

$$\frac{\partial R}{\partial p} = -1.98 - 2.110w - 0.63h + 0.62wh + 2 \cdot 1.39p = 0 \quad (4.2)$$

$$\frac{\partial R}{\partial w} = 2.49 - 2.11p + 0.04h + 0.62ph + 2 \cdot 1.84w = 0 \quad (4.3)$$

$$\frac{\partial R}{\partial h} = -1 - 0.63p + 0.042w + 0.62pw + 2 \cdot 1.810h = 0 \quad (4.4)$$

Now, the system of equations (4.2), (4.3) and (4.4) can be numerically solved and the minimum is reached at 0.53 for the period, -0.41 for the linewidth and 0.41 for the height. The model used is normalized so that the bottom and the top values of the variation range are -1 and 1 respectively. Consequently, the mentioned minimum corresponds to 429 nm for the period, 188 nm for the linewidth and 190 nm for the height.

In *Fig.4.4* the model is plotted along the period and the linewidth for a constant value of height fixed as the calculated minimum (h=0.41). The minimum is observed at the mathematically calculated values. The value of the AWR estimated by the model (AWR*) for this structure is 11.75 %. This value is just an estimated value so the optimum structure will be simulated to obtain the real theoretical value for the final comparison between PCs in the next section.

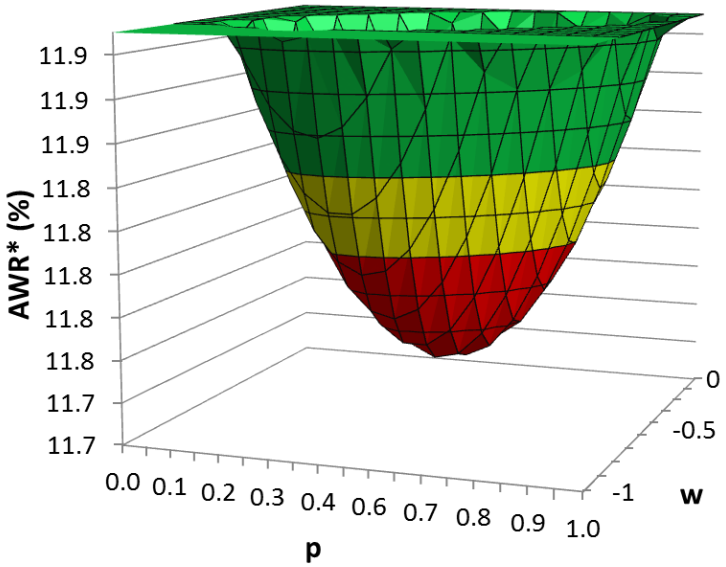

Fig.4.4. Response surface for the AWR of the rectangular lines for h = 0.41. The minimum is observed for a normalized period of 0.53 (429 nm), a normalized linewidth of -0.41 (188 nm) and a normalized height of 0.41 (190 nm).

1.1.3.2. 1D Triangular lines (Fig.4.1.b)

Our fabrication process for this structure consists on a KOH etching of Si, using a pattern of lines as a mask. Due to the anisotropy of KOH etching and the <100> crystalline orientation of the used Si substrates, the angle of etching is 54.7° with respect to the Si surface (see *Fig.4.5*). Therefore, there are only two input variables to consider in the DOE: the period and the height. In this case, due to the KOH etching, the range of variation of the height can be broader from 20 nm to 500 nm. The DOE obtained is summarized in *Table 4.3*.

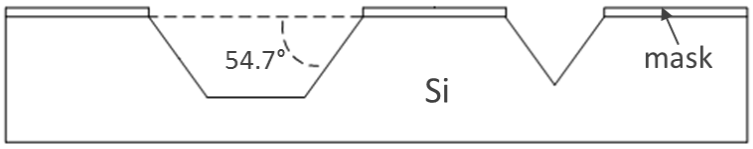

Fig.4.5. Schematic representation of the KOH etching process.

# run	Period (nm)	Heigth (nm)	AWR (%)
1	287.87	90.29	**14.39**
2	287.87	429.71	**8.01**
3	712.13	90.29	**17.28**
4	712.13	429.71	**8.02**
5	500.00	260.00	**8.64**
6	200.00	260.00	**8.59**
7	800.00	260.00	**12.77**
8	500.00	20.00	**19.49**
9	500.00	500.00	**6.37**

Table 4.3. DOE for the structure of triangular lines.

The curves of the simulations results for the nine runs are shown in *Fig.4.6*. The optimum PC of the DOE presents a simulated reflectance of 10% over a broad range from 600 nm to 1000 nm of wavelength.

The obtained model is presented in *Table 4.4*. The fit indicators show a great adjustment of the model to the data with a R^2 = 0.99 very close to 1, a F = 100, very far from 6 and a very low $SigF = 9.9 \cdot 10^{-6}$. With the model of *Table 4.4*, the optimum values of the input parameters are calculated with the same process as the one explained for the previous structure. The optimum period is 456 nm, which corresponds to a normalized value of -0.2 and the optimum height 421 nm, which correspond to 0.95. The value of the AWR* for this structure is 6.5 %.

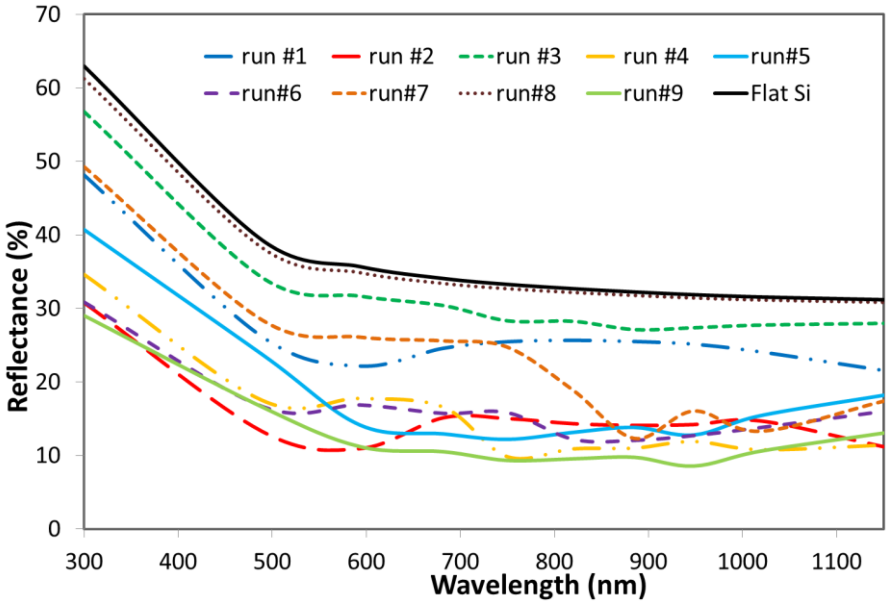

Fig.4.6. Simulated reflectance results for all the runs in the DOE for the structure of triangular lines.

Model			Fit Indicators	
Factor	Coeff	P-value		
Const	10.07	5.5E-07	**R2**	9.7E-01
p	1.10	1.4E-02	**Adj R2**	9.5E-01
h	-4.28	1.1E-05	**Std Error**	9.1E-01
ph	-0.72	1.6E-01	**F**	4.2E+01
pp	0.33	3.9E-01	**Sig F**	1.4E-04
hh	1.46	6.7E-03		

Table 4.4. Model calculated for the reflectance of the structure of triangular lines.

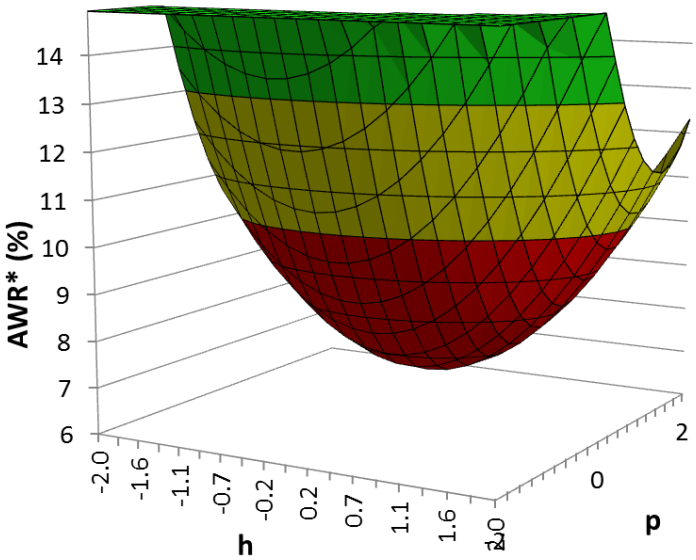

Fig.4.7. Response surface for the AWR of the structure of triangular lines. The minimum is observed at a normalized period of -0.2 (456 nm) and a normalized height of 0.95 (421 nm).

1.1.3.3. 1D Circular lines (Fig.4.1.c)

This pattern has been designed as an array of empty half-cylinders tangential to each other so pitch and linewidth are the same. The height is the radius of the cylinder so with one parameter the whole structure is defined. For this reason, the optimization process is simpler in this case. First, the reflectance of 8 PCs with different periods has been simulated (*Fig.4.8*) and then, the AWR values have been calculated and represented along the period to choose the optimum (*Fig.4.9*). The minimum AWR according to the graph of *Fig.4.9* is at 430 nm of period and the corresponding AWR* is 11.7%.

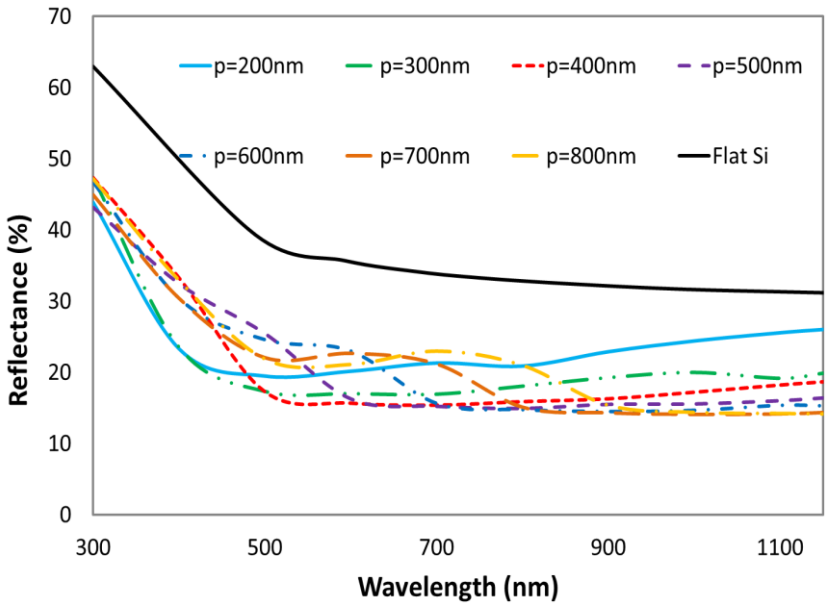

Fig.4.8. Simulated reflectance results for all the runs in the DOE for the structure of circular lines.

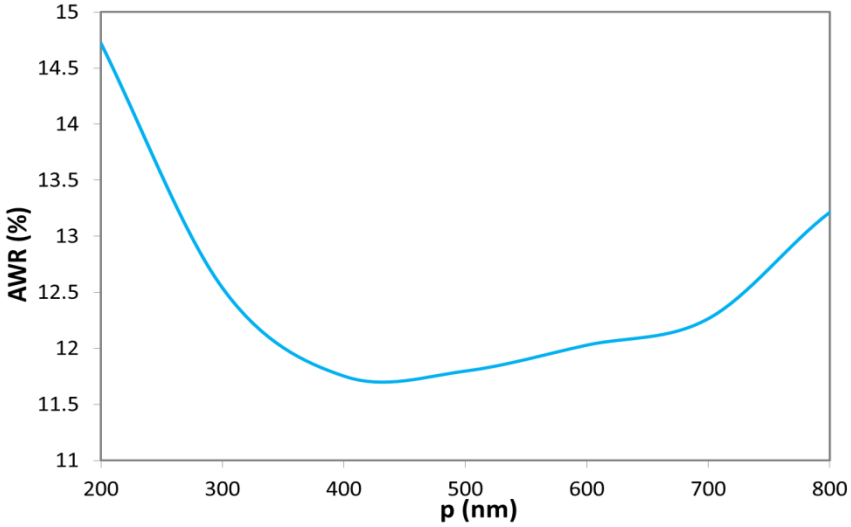

Fig.4.9. AWR dependence with the period for the structure of circular lines.

1.1.3.4. Circular pillars in square lattice (Fig.4.1.d)

For this structure, there are three independent parameters to optimize: the period, the diameter and the height. The corresponding 3-level CCD is summarized in *Table 4.5* and the calculated reflectance for all the runs in *Fig.4.10*.

# run	Period (nm)	Diameter (nm)	Heigth (nm)	AWR (%)
1	241.89	153.65	68.78	**8.54**
2	241.89	153.65	241.22	**10.77**
3	241.89	516.35	68.78	**19.38**
4	241.89	516.35	241.22	**19.38**
5	658.11	153.65	68.78	**17.60**
6	658.11	153.65	241.22	**13.34**
7	658.11	516.35	68.78	**12.64**
8	658.11	516.35	241.22	**8.87**
9	450	335	155	**3.25**
10	100	335	155	**17.47**
11	800	335	155	**13.15**
12	450	30	155	**19.49**
13	450	640	155	**19.61**
14	450	335	10	**19.26**
15	450	335	300	**9.85**

Table 4.5. DOE 1 for the structure of circular pillars in square lattice.

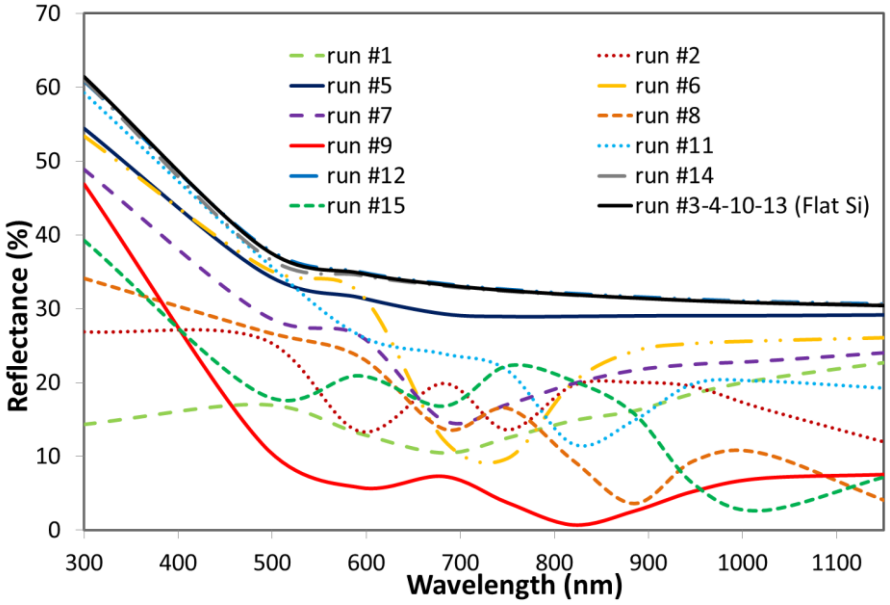

Fig.4.10. Simulated reflectance results for all the runs in the DOE 1 for the structure of circular pillars in square lattice.

The run #9 shows a reflectance under 10% from 500 nm of wavelength, having hills and valleys along the spectral band and reaching a minimum close to 0 % of

reflectance at 820 nm. This result improves the behavior of all the optimized 1D structures.

The model obtained for the reflectance is summarized in *Table 4.6*. Again, according to the fit indicators, the model is a good enough estimation for the reflectance in the considered range of variation of the input variables. The minimum obtained with this model is plotted in *Fig.4.11*. The optimum PC has a period of 448 nm, a diameter of 325 nm and a height of 138 nm. The value of the AWR* for this structure is 3.05 %.

Model		
Factor	Coeff	P-value
Const	3.32	7.0E-04
p	-0.94	1.4E-01
w	0.75	2.3E-01
h	-1.58	2.1E-02
pw	-3.61	5.8E-04
ph	-1.28	1.3E-01
hw	-0.22	7.9E-01
pwh	0.34	6.7E-01
pp	3.55	3.4E-05
ww	5.05	9.7E-07
hh	3.28	7.0E-05

Fit Indicators	
R^2	9.4E-01
Adj R^2	8.9E-01
Std Error	2.2E+00
F	1.9E+01
Sig F	7.0E-06

Table 4.6. Model calculated for the reflectance of the structure of circular pillars in square lattice with DOE1

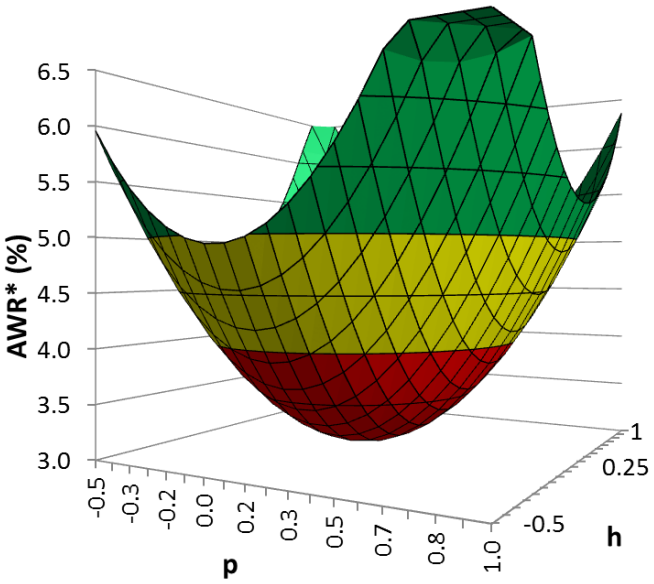

Fig.4.11. Response surface for the AWR of the structure of circular pillars in square lattice. The optimum is observed at a normalized period of 0.18 (488 nm), a normalized diameter of -0.0055(334 nm) and a normalized height of 0.27 179 nm.

1.1.3.5. 2D Circular holes in square lattice (Fig.4.1.e)

For this structure there are also three variables to consider. The corresponding DOE is summarized in *Table 4.7* and the simulation results for all the runs in *Fig.4.12*. There are two of structures (run #9 and run #8) with very low reflectance minimums (at 500 nm and 720 nm respectively) but with values over 10% in the rest of the spectrum.

# run	Period (nm)	Diameter (nm)	Heigth (nm)	AWR (%)
1	241.89	153.65	68.78	**8.54**
2	241.89	153.65	241.22	**14.21**
3	241.89	516.35	68.78	**19.38**
4	241.89	516.35	241.22	**19.38**
5	658.11	153.65	68.78	**18.54**
6	658.11	153.65	241.22	**18.59**
7	658.11	516.35	68.78	**14.92**
8	658.11	516.35	241.22	**8.30**
9	450	335	155	**9.16**
10	100	335	155	**17.23**
11	800	335	155	**16.40**
12	450	30	155	**19.55**
13	450	640	155	**19.61**
14	450	335	10	**19.31**
15	450	335	300	**11.34**

Table 4.7. DOE for the structure of circular holes in square lattice.

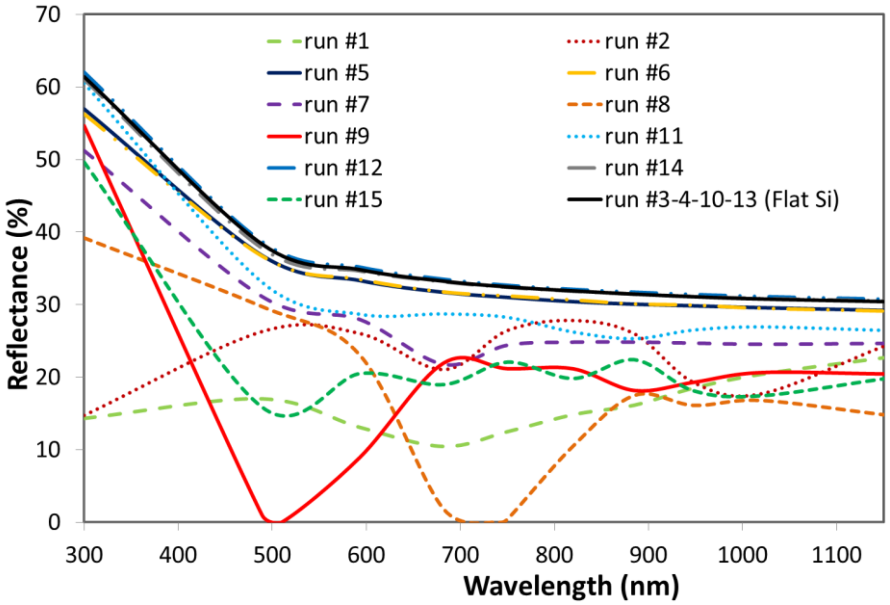

Fig.4.12.Simulated reflectance results for all the runs in the DOE for the structure of circular holes in square lattice.

The model obtained from these curves is summarized in *Table 4.8*. The fit indicators of *Table 4.8* show a good adjustment of the model to the output data calculated by simulation.

Model		
Factor	Coeff	P-value
Const	9.213	1.9E-09
p	-0.204	6.7E-01
w	0.178	7.1E-01
h	-1.06240	4.3E-02
pw	-3.769	5.0E-05
ph	-1.50097	3.1E-02
hw	-1.57047	2.5E-02
pwh	-0.09563	8.8E-01
pp	2.194	2.9E-04
ww	3.172	9.7E-06
hh	1.667	2.4E-03

Fit Indicators	
R^2	9.2E-01
Adj R^2	8.6E-01
Std Error	1.7E+00
F	1.5E+01
Sig F	2.9E-05

Table 4.8. Model calculated for the reflectance of the structure of circular holes in square lattice.

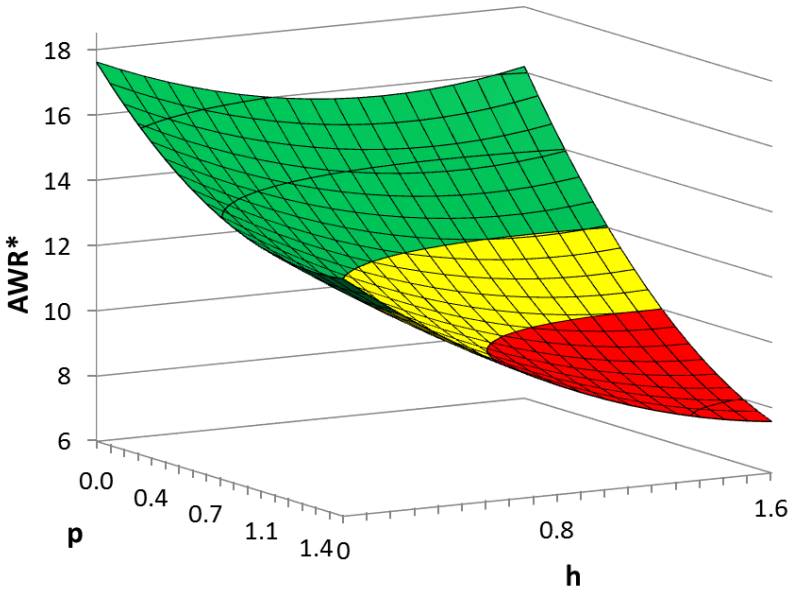

Fig.4.13. Response surface for the AWR for the circular holes in square lattice. The optimum structure correspond to the larger values of the parameters: period of 800 nm, diameter of 640 nm and height of 300 nm.

The response surface is represented in *Fig.4.13*. It seems like the absolute minimum would be reached close to the upper star points but it is outside the range. Therefore, the optimum is considered at the edge of the three ranges (period of 800 nm, diameter of 640 nm and height of 300 nm). The value of the AWR* for this optimum is 7.6%.

1.1.3.6. 2D Circular pillars in hexagonal lattice (Fig.4.1.f)

This structure also has three input parameters. The corresponding DOE is summarized in *Table 4.9* and the simulated reflectance curves in *Fig.4.14*.

# run	Period (nm)	Diameter (nm)	Heigth (nm)	AWR (%)
1	241.89	153.65	68.78	**7.55**
2	241.89	153.65	241.22	**10.60**
3	241.89	516.35	68.78	**19.63**
4	241.89	516.35	241.22	**19.63**
5	658.11	153.65	68.78	**17.49**
6	658.11	153.65	241.22	**11.88**
7	658.11	516.35	68.78	**11.53**
8	658.11	516.35	241.22	**10.55**
9	450	335	155	**4.03**
10	100	335	155	**17.17**
11	800	335	155	**8.28**
12	450	30	155	**19.57**
13	450	640	155	**19.74**
14	450	335	10	**19.39**
15	450	335	300	**11.00**

Table 4.9.DOE for the structure of circular pillars in hexagonal lattice.

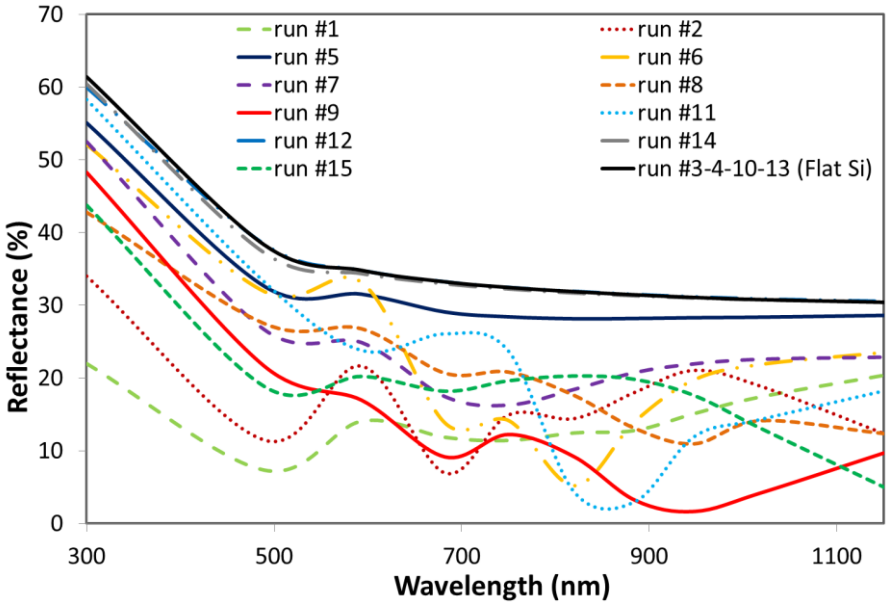

Fig.4.14. Simulated reflectance results for all the runs in the DOE for the structure of circular pillars in hexagonal lattice.

The parameters of the model are shown in *Table 4.10* and the obtained surface is plot in *Fig.4.15*. There is an optimum structure with a period of 531 nm, a diameter of 339 nm and a height of 178 nm with an AWR* of 3.64%.

Model		
Factor	Coeff	P-value
Const	4.098	1.7E-04
p	-1.532	3.0E-02
w	1.031	1.2E-01
h	-1.29301	6.0E-02
pw	-3.551	9.1E-04
ph	-1.20416	1.6E-01
hw	0.19849	8.1E-01
pwh	0.95913	2.6E-01
pp	2.457	1.1E-03
ww	4.908	2.0E-06
hh	3.329	8.8E-05

Fitting Indicators	
R^2	9.3E-01
Adj R^2	8.7E-01
Std Error	2.3E+00
F	1.6E+01
Sig F	2.0E-05

Table 4.10. Model calculated for the reflectance of the structure of circular pillars in hexagonal lattice.

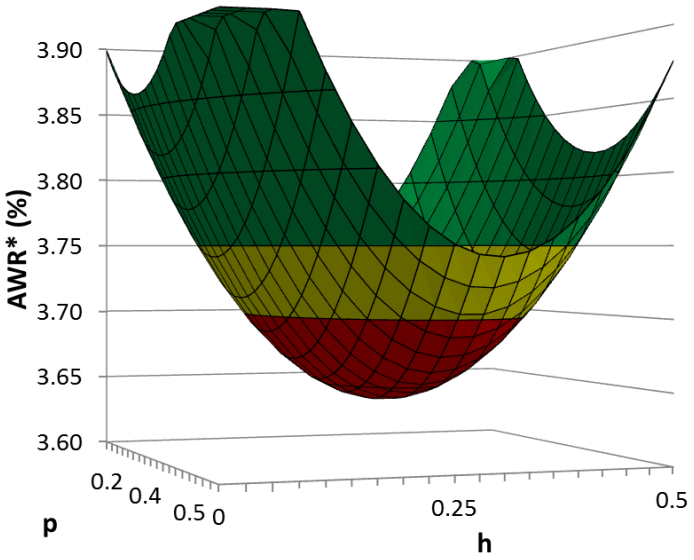

Fig.4.15. Response surface for the AWR of the circular pillars in hexagonal lattice. There is an optimum structure with a normalized period of 0.39 (531 nm), a normalized diameter of 0.021 (339 nm) and a normalized height of 0.26 (178 nm).

1.1.3.7. 2D Circular holes in hexagonal lattice (Fig.4.1.g)

This structure has three input variables so the DOE is a 3-level CCD. The values for the three input variables for every experiment in the DOE and its calculated AWR are summarized in *Table 4.11*. The reflectance versus wavelength curves obtained by computer simulation for all these runs are presented together in the graph of *Fig.4.16*. Both the curves and the calculated AWR data have higher values than the case of pillars in hexagonal lattice.

# run	Period (nm)	Diameter (nm)	Heigth (nm)	AWR (%)
1	241.89	153.65	68.78	**13.05**
2	241.89	153.65	241.22	**14.07**
3	241.89	516.35	68.78	**19.63**
4	241.89	516.35	241.22	**19.63**
5	658.11	153.65	68.78	**18.48**
6	658.11	153.65	241.22	**18.56**
7	658.11	516.35	68.78	**14.45**
8	658.11	516.35	241.22	**8.27**
9	450	335	155	**10.29**
10	100	335	155	**17.17**
11	800	335	155	**15.79**
12	450	30	155	**19.66**
13	450	640	155	**19.74**
14	450	335	10	**19.42**
15	450	335	300	**10.33**

Table 4.11. DOE for the structure of circular holes in hexagonal lattice.

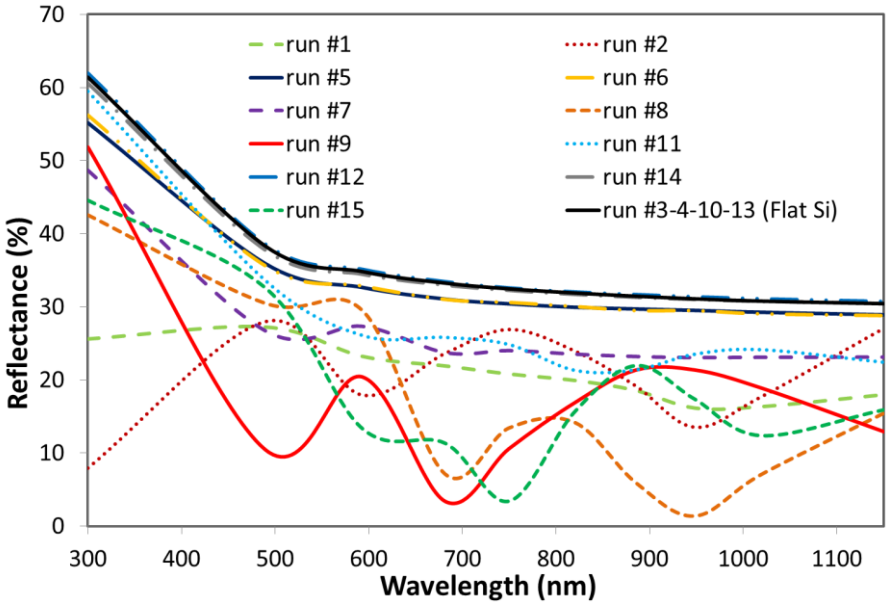

Fig.4.16. Simulated reflectance results for all the runs in the DOE for the structure of circular holes in hexagonal lattice.

The obtained model is summarized in *Table 4.12*. and represented as a surface in *Fig.4.17*. There is not an absolute minimum in the surface because the output decrease continuously when the period, diameter or height are increased. Therefore, the upper limits of all the variables are considered as the optimum values. This means that the best structure in this range is the one with 800 nm of period, 640 nm of diameter and 300 nm of height. The AWR* is 6.5 %.

Model		
Factor	Coeff	P-value
Const	10.33	4.5E-11
p	-0.65	1.1E-01
w	-0.15	7.0E-01
h	-1.49	2.1E-03
pw	-3.31	2.4E-05
ph	-0.89	1.0E-01
hw	-0.91	9.3E-02
pwh	-0.66	2.1E-01
pp	1.84	2.2E-04
ww	2.98	2.2E-06
hh	1.28	3.6E-03

Fitting Indicators	
R^2	9.4E-01
Adj R^2	8.9E-01
Std Error	1.4E+00
F	1.8E+01
Sig F	9.8E-06

Table 4.12. Model calculated for the reflectance of the structure of circular holes in hexagonal lattice.

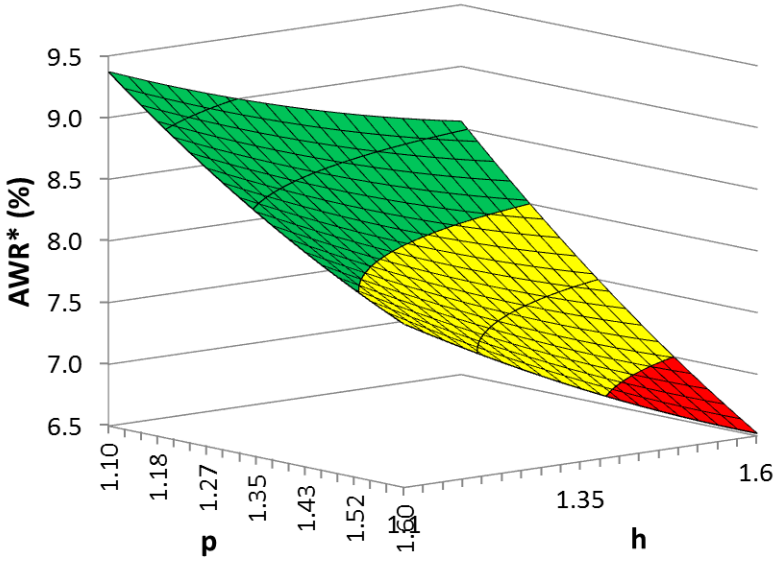

Fig.4.17. Response surface for the AWR of the circular holes in hexagonal lattice. The best structure is at the upper edge of the variation range for the three parameters: 800 nm for the period, 640 nm for the diameter and 300 nm for the height.

1.1.3.8. 2D Square pillars in square lattice (Fig.4.1.h)

The DOE for this structure is the 3 - level CCD summarized in *Table 4.13*. The last column of the table corresponds to the AWR obtained from the curves of the calculated reflectance vs wavelength for each experiment. The mentioned curves are shown in *Fig.4.18*. The optimum of these curves corresponds to the run #9, which presents a minimum of zero reflectance at 830 nm. However, its AWR is higher than those obtained in some of the runs of the circular pillars in square lattice.

# run	Period (nm)	Linewidth (nm)	Heigth (nm)	AWR (%)
1	241.89	153.65	68.78	**7.16**
2	241.89	153.65	241.22	**8.92**
3	241.89	516.35	68.78	**19.38**
4	241.89	516.35	241.22	**19.38**
5	658.11	153.65	68.78	**17.16**
6	658.11	153.65	241.22	**11.39**
7	658.11	516.35	68.78	**12.24**
8	658.11	516.35	241.22	**11.66**
9	450	335	155	**6.41**
10	100	335	155	**17.47**
11	800	335	155	**11.02**
12	450	30	155	**19.41**
13	450	640	155	**19.61**
14	450	335	10	**19.18**
15	450	335	300	**10.96**

Table 4.13. DOE for the structure of square pillars in square lattice.

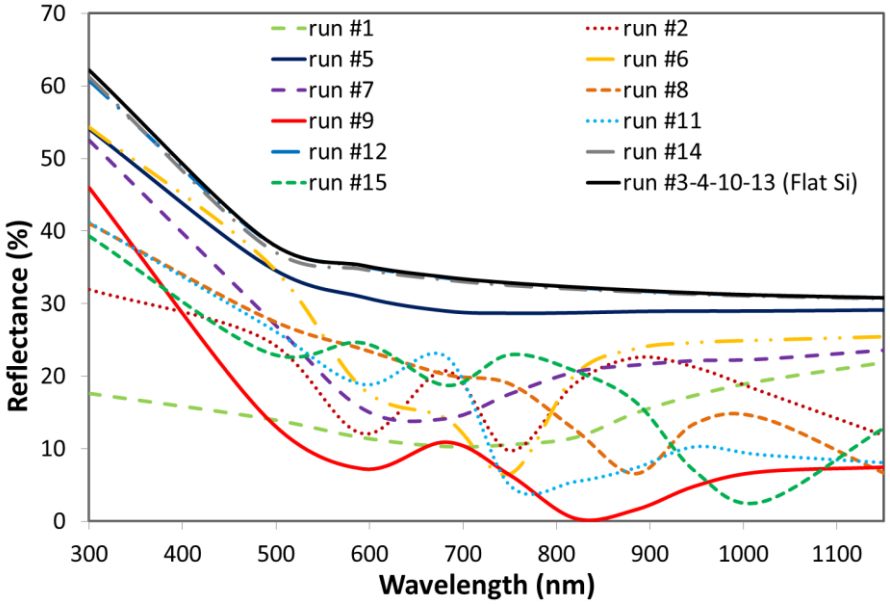

Fig.4.18. Simulated reflectance results for all the runs in the DOE for the structure of square pillars in square lattice.

The model obtained from the AWR values is summarized in *Table 4.14*. Also, this model is represented as a surface dependent on the diameter and the height in *Fig.4.19*. The absolute minimum reflectance of the model is obtained for a period of 503 nm, a width of 319 nm and a height of 186. The value of the AWR* for these values is 6.1%.

Model			Fit Indicators	
Factor	Coeff	P-value		
Const	6.486	4.8E-06	R^2	8.8E-01
p	-0.970	1.8E-01	Adj R^2	7.9E-01
w	1.345	6.9E-02	Std Error	2.5E+00
h	-1.34967	6.9E-02	F	9.1E+00
pw	-3.419	2.2E-03	Sig F	3.5E-04
ph	-1.01466	2.7E-01		
hw	0.42817	6.4E-01		
pwh	0.86803	3.4E-01		
pp	2.052	6.6E-03		
ww	3.913	4.2E-05		
hh	2.343	2.8E-03		

Table 4.14. Model calculated for the reflectance of the structure of square pillars in square lattice.

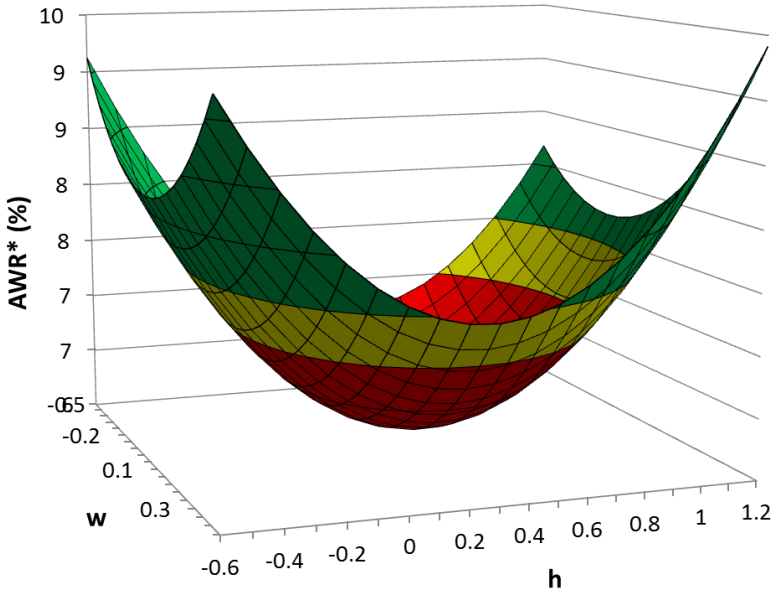

Fig.4.19. Response surface for the AWR of the square pillars in square lattice for a constant. The optimum is found at 503 nm of period (0.26 in normalized values), 319 nm of width (-0.089 in normalized values) and a 186 nm of height (0.36 in normalized values).

1.1.3.9. 2D Square holes in square lattice (Fig.4.1.i)

The DOE obtained for the optimization of this structure is summarized in *Table 4.15*. There are three variable parameters in the geometry so 15 runs are obtained. The AWR calculated by simulation for each experiment is shown in the last column of the table.

# run	Period (nm)	Linewidth (nm)	Heigth (nm)	AWR (%)
1	241.89	153.65	68.78	**12.33**
2	241.89	153.65	241.22	**12.81**
3	241.89	516.35	68.78	**19.38**
4	241.89	516.35	241.22	**19.38**
5	658.11	153.65	68.78	**18.21**
6	658.11	153.65	241.22	**18.20**
7	658.11	516.35	68.78	**14.28**
8	658.11	516.35	241.22	**8.89**
9	450	335	155	**8.46**
10	100	335	155	**17.47**
11	800	335	155	**14.77**
12	450	30	155	**19.52**
13	450	640	155	**19.61**
14	450	335	10	**19.23**
15	450	335	300	**9.36**

Table 4.15.DOE for the structure of square holes in square lattice.

The reflectance curves obtained by simulation for all the runs of the DOE are shown in *Fig.4.20* and the model obtained from these data is summarized in *Table 4.16*. This model is also represented in *Fig.4.21* for a constant value of width. The surface has a minimum AWR* of 7.85 % corresponding to an optimum structure with a period of 556 nm, a diameter of 395 nm and a height of 213 nm.

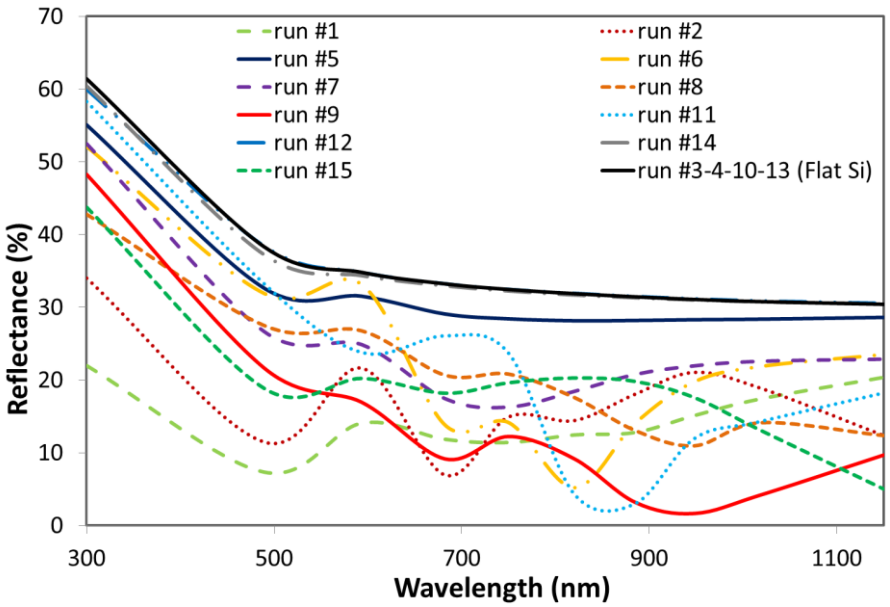

Fig.4.20. Simulated reflectance results for all the runs in the DOE for the structure of square holes in square lattice.

Model			Fitting Indicators	
Factor	Coeff	P-value		
Const	8.498	1.0E-09	R^2	9.5E-01
p	-0.649	1.4E-01	Adj R^2	9.0E-01
w	0.040	9.2E-01	Std Error	1.5E+00
h	-1.57560	2.3E-03	F	2.1E+01
pw	-3.360	4.1E-05	Sig F	4.8E-06
ph	-0.73438	2.0E-01		
hw	-0.73198	2.0E-01		
pwh	-0.61181	2.8E-01		
pp	2.351	4.7E-05		
ww	3.568	7.1E-07		
hh	1.706	7.4E-04		

Table 4.16. Model calculated for the reflectance of the structure of square holes in square lattice.

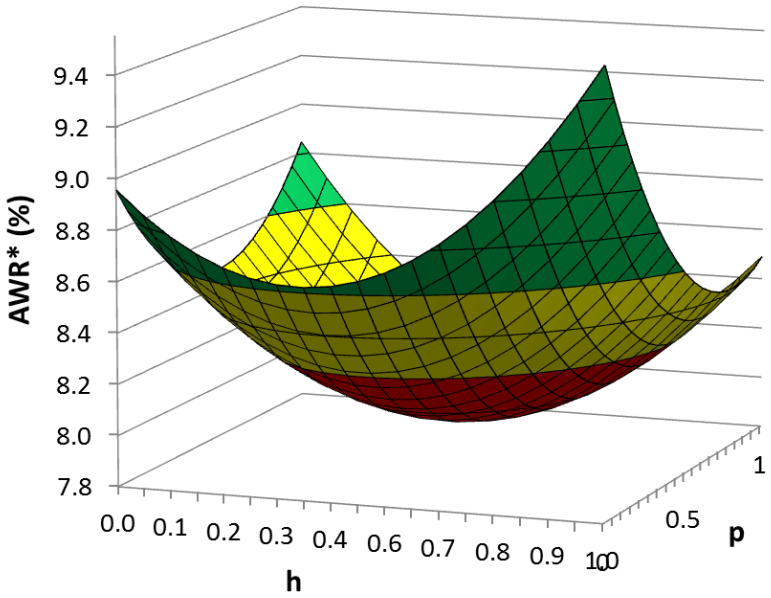

Fig.4.21. Response surface for the AWR of the structure of square holes in square lattice. The optimum structure has a normalized period of 0.51 (556 nm), a normalized diameter of 0.33 (395 nm) and a normalized height of 0.67 (213 nm).

1.1.3.10. 2D Inverted pyramids (Fig.4.1.j)

In this case, the fabrication process is equivalent to the case of triangular lines. To obtain a pattern of inverted pyramids, we do a KOH etching process of Si using a pattern of circular holes as mask. As a result, the etching angle is fixed to 54.7° (see *Fig.4.5*) and there are only two input variables, the period and the height. The respective DOE has only the 9 runs summarized in *Table 4.17*.

The results obtained in the simulations are presented in *Fig.4.22* and the model obtained for the AWR is summarized in *Table 4.18*. This model is represented with the

surface of *Fig.4.23* along the range of variation of both the period and the height. This time, the minimum is observed slightly outside of the range of variation of the pyramid height but close enough to be calculated. The optimum period is 760 nm and the optimum height is 536.7 nm. The AWR* for this optimum design is 5.62 %.

# run	Period (nm)	Heigth (nm)	AWR (%)
1	287.87	90.29	**13.88**
2	287.87	429.71	**7.20**
3	712.13	90.29	**18.55**
4	712.13	429.71	**5.89**
5	500	260	**9.23**
6	200	260	**8.82**
7	800	260	**14.04**
8	500	20	**19.38**
9	260	500	**6.30**

Table 4.17.DOE for the structure of inverted pyramids.

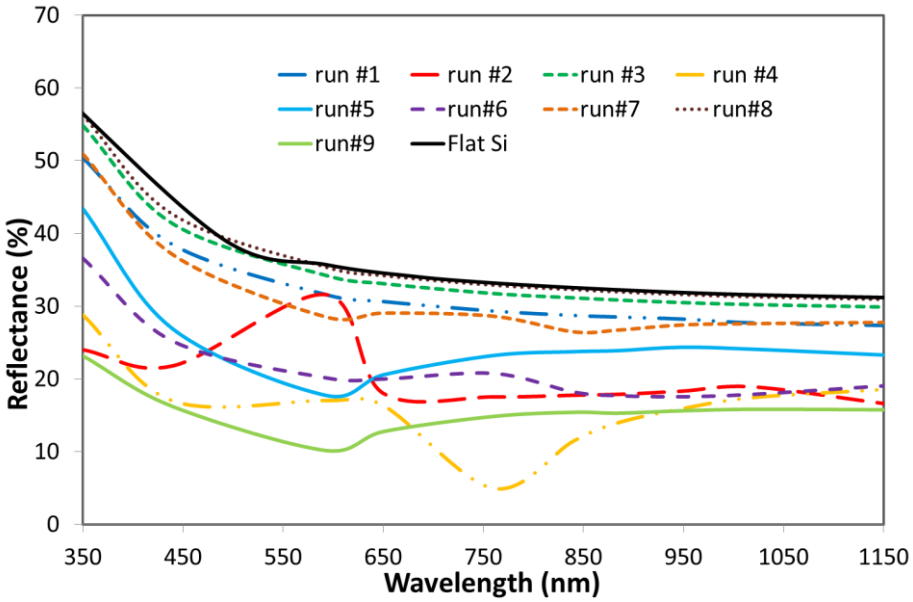

Fig.4.22. Simulated reflectance results for all the runs in the DOE for the structure of inverted pyramids.

Model			Fitting Indicators	
Factor	Coeff	P-value		
Const	14.25	1.96E-06	**R^2**	9.2E-01
p	0.65	2.93E-01	**Adj R^2**	8.6E-01
h	-4.58	1.84E-04	**Std Error**	1.6E+00
ph	-1.52	1.05E-01	**F**	1.5E+01
pp	0.65	3.39E-01	**Sig F**	2.6E-03
hh	0.55	4.18E-01		

Table 4.18. Model calculated for the reflectance of the structure of inverted pyramids.

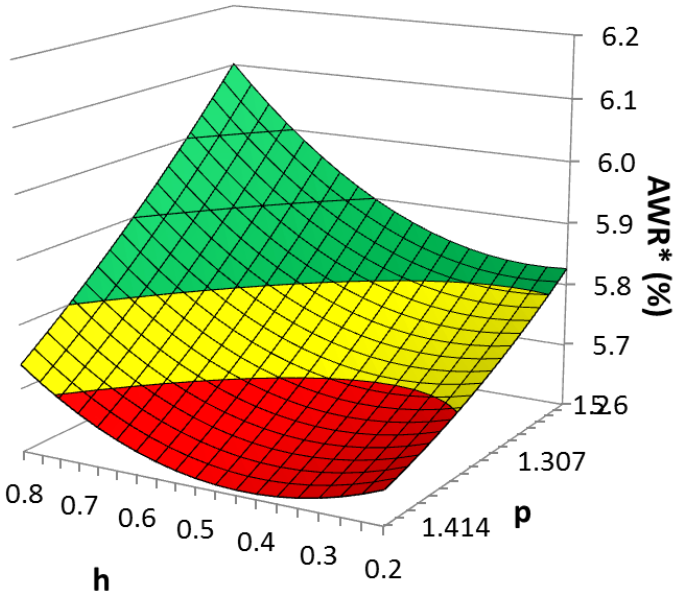

Fig.4.23. Response surface for the AWR of the structure of inverted pyramids. The minimum is observed outside of the range of variation of the height at: period of 760 nm and height of 536.7 nm (normalized values of 0.75 and 1.81 respectively).

1.1.3.11. 2D Cones (Fig.4.1.k)

There are three input parameters in the cone geometry, which results in the 3 - level CCD summarized in *Table 4.19*. All the reflectance curves obtained from the simulations of this DOE are presented in *Fig.4.24*.

# run	Period (nm)	Linewidth (nm)	Heigth (nm)	AWR (%)
1	241.89	153.65	68.78	**19.68**
2	241.89	153.65	241.22	**9.87**
3	241.89	516.35	68.78	**21.46**
4	241.89	516.35	241.22	**12.69**
5	658.11	153.65	68.78	**22.13**
6	658.11	153.65	241.22	**20.42**
7	658.11	516.35	68.78	**21.65**
8	658.11	516.35	241.22	**14.62**
9	450	335	155	**16.37**
10	100	335	155	**18.30**
11	800	335	155	**21.35**
12	450	30	155	**22.76**
13	450	640	155	**17.55**
14	450	335	10	**22.78**
15	450	335	300	**8.76**

Table 4.19.DOE for the structure of cones.

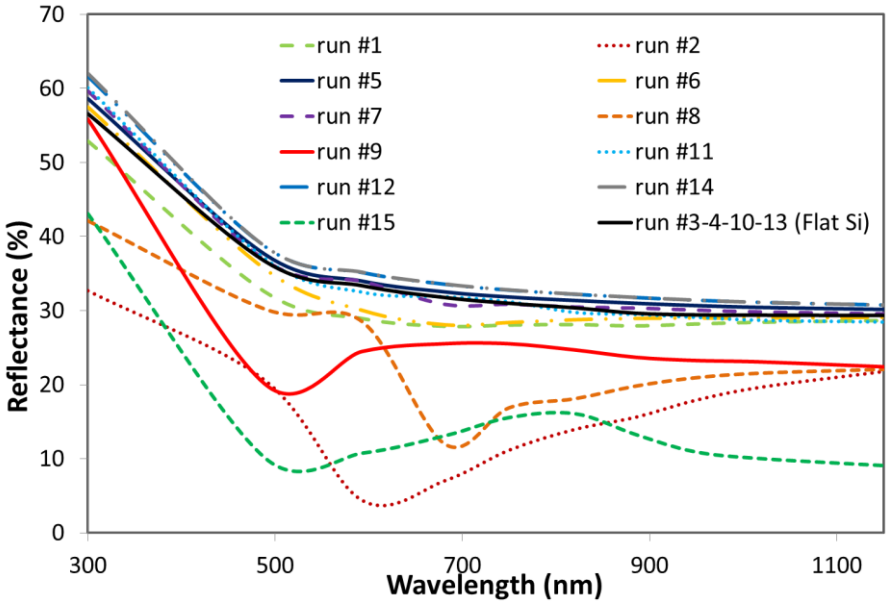

Fig.4.24. Simulated reflectance results for all the runs in the DOE for the structure of cones.

The parameters of the model obtained after the post-processing of the simulation data are summarized in *Table 4.20*. This model is plotted as a surface dependent on the period and the diameter for a constant value of height in *Fig.4.25*.

Model		
Factor	Coeff	P-value
Const	16.385	7.1E-15
p	1.484	2.5E-04
w	-0.765	2.1E-02
h	-3.72699	2.1E-08
pw	-1.360	3.6E-03
ph	1.22896	6.8E-03
hw	-0.53639	1.8E-01
pwh	-0.79650	5.6E-02
pp	1.036	2.2E-03
ww	1.153	1.0E-03
hh	-0.398	1.6E-01

Fitting Indicators	
R^2	9.6E-01
Adj R^2	9.2E-01
Std Error	1.1E+00
F	2.7E+01
Sig F	1.2E-06

Table 4.20. Model calculated for the reflectance of the structure of cones.

Once more, the absolute minimum is not observed in the surface of *Fig.4.25*. In contrast, the reflectance keeps decreasing when either the period decreases or the height increases. However, for the highest cones simulated there is an optimum value of diameter in the studied range at 135 nm. Therefore, the optimum structure in the considered range is the structure of cones with 100 nm of period and 300 nm of

height. The optimum of 135 nm of diameter is adjusted to 100 nm so it is not bigger than the period. For this structure, the AWR* is 5.1 %.

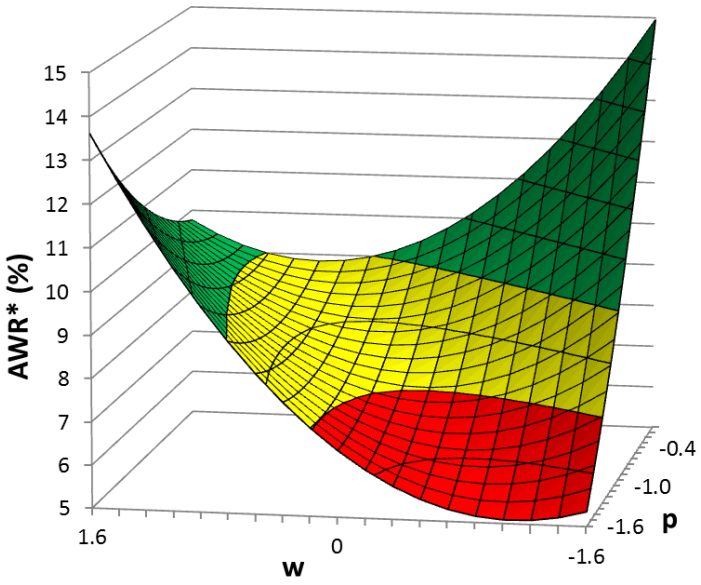

Fig.4.25. Response surface for the AWR of the structure of cones. The optimum structure has a normalized period of -1.6 (100 nm) and a normalized height of 1.6 (300 nm).

1.1.4. Comparison between different photonic crystals

The optimum structures obtained in each one of the DOEs explained in the previous section have been simulated and their AWR has been calculated in order to compare between them and to choose the optimum. The reflectance of the optimum models is presented in *Fig.4.26*. In the graph, the reflectance of a flat Si surface is also plotted for comparison. As expected, the flat Si reflectance is much higher than the reflectance of nanostructured Si. The curve of cones stand out among the others due to its low reflectance values along all the wavelength range considered. In fact, for wavelengths less than 500 nm is the only curve with reflectance under 5 %.

However, as explained in chapter 2, to compare between all the simulations taking into account the final application, the curves are multiplied by the weighting curve obtaining the curves of *Fig.4.27*. In this graph, there are other curves, apart from the cones, with low reflectance; particularly, the curves corresponding to the inverted pyramids and all kind of pillars (circular or square distributed in square or hexagonal lattices).

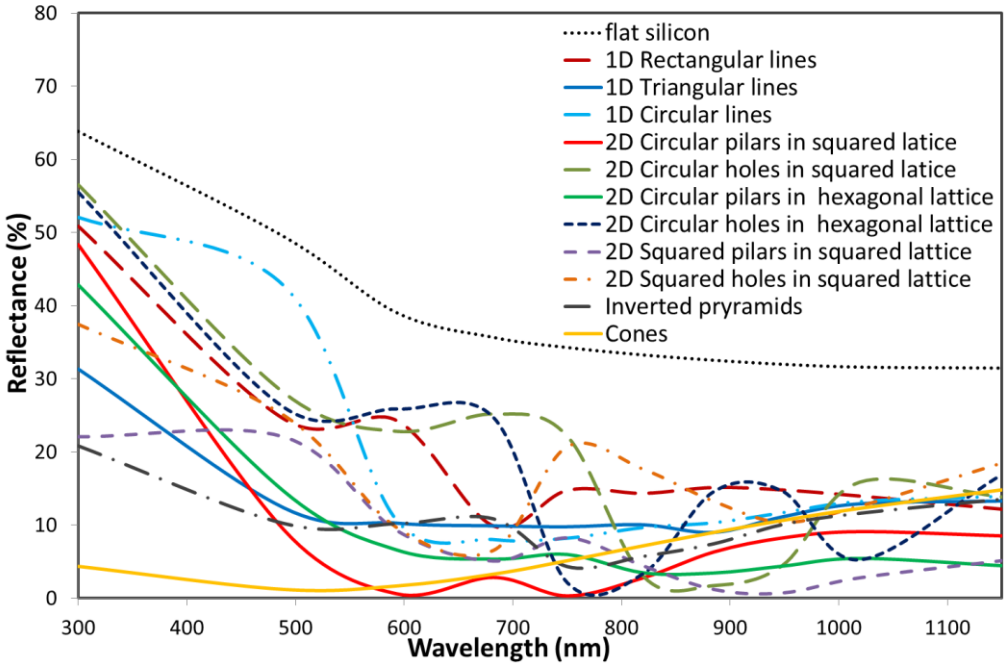

Fig.4.26. Reflectance vs wavelength for the optimum structure of each design of section 1.1.

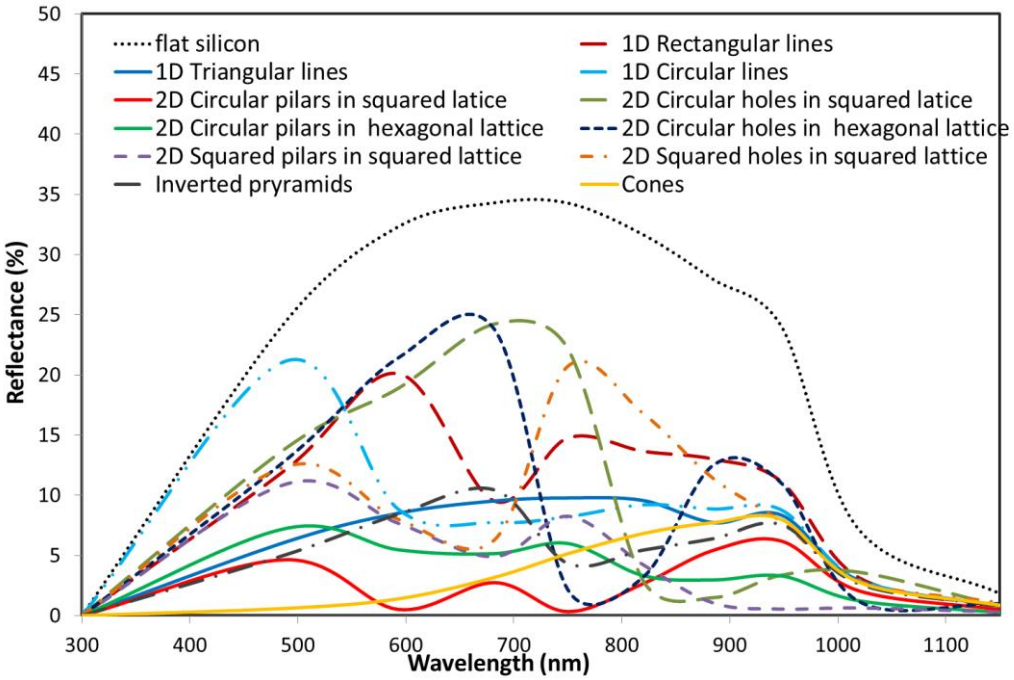

Fig.4.27. Reflectance vs wavelength for the optimum structures of each design of section 1.1.

To help with the comparison, the average reflectance and the AWR have been calculated for all the structures. The results are summarized in *Table 4.21*. In the column of average reflectance, the lowest value is, as expected, for the structure of cones with a value of 6.3 %. However, when the weighting curve is considered, the AWR of the cones is 3.13 %, which is slightly higher than the reflectance of the circular

pillars in circular lattice, which is 2.53 %. This small difference, together with the simpler and better-known fabrication process of this structure make the pillars to be chosen as the optimum design for Si solar cell application in this work.

Structure	Average reflectance (%)	Average weighted reflectance (%)
Flat silicon 	39.93	21.35
1D Rectangular lines 	20.80	9.83
1D Triangular lines 	13.41	6.10
1D Circular lines 	20.89	8.54
2D Circular pilars in squared latice 	10.44	2.53
2D Circular holes in squared latice 	21.53	9.68
2D Circular pilars in hexagonal lattice 	10.90	3.75
2D Circular holes in hexagonal lattice 	20.52	9.32
2D Squared pilars in squared lattice 	9.68	4.43
2D Squared holes in squared lattice 	18.00	8.54
Inverted pryramids 	10.83	5.03
Cones 	6.30	3.13

Table 4.21. Average reflectance and AWR for the optimum structures of each design of section 1.1.

1.2 FABRICATION OF PCs ON POLISHED SUBSTRATES.

The first fabrications of PCs in this work were done to validate the simulation method by comparison between calculated and measured reflectance. For this purpose, some structures were chosen, simulated and fabricated (see Chapter 3).

After that, we fabricated some of the optimized PCs presented in the previous section. To keep the fabrication as simple as possible, we first fabricated the two better 1D designed structures, which are the pattern of rectangular and triangular shaped lines and then we have fabricated the optimum structure, i.e. the PC of circular pillars in square lattice. The results and discussion are detailed in two scientific papers presented in the 1.2.2 subsection.

In the cases of the PC of rectangular lines and the PC of circular pillars, prior to the fabrication processes we have performed a second DOE centered in the previous optimums and reducing the variation range of the dimensions to avoid overlapping between the period and the linewidth. The PC of triangular lines has not the overlapping problem so we have trust the design obtained in the previous section.

1.2.1. Final designs for the 1D and 2D structures

In this section we present the new optimization processes developed for both the pattern of rectangular lines and the pattern of circular pillars in square lattice. In both cases, a DOE centered in the optimum obtained in the previous section has been carried out. The range of variation of the dimensions has been reduced to avoid the overlap between period and linewidth or diameter.

1.2.1.1. 1D Rectangular lines

The DOE obtained for this structure is summarized in *Table 4.22*. The period has been studied in the range from 350.67 nm to 499.33 nm, the linewidth from 98.65 nm to 241.35 nm and the height from 68.78 nm to 241.22 nm. The simulation curves for each combination of parameters of the DOE are represented in *Fig.4. 28*.

# run	Period (nm)	Linewidth (nm)	Heigth (nm)	AWR (%)
1	350.67	98.65	68.78	**12.79**
2	350.67	98.65	241.22	**15.11**
3	350.67	241.35	68.78	**23.12**
4	350.67	241.35	241.22	**23.12**
5	499.33	98.65	68.78	**17.36**
6	499.33	98.65	241.22	**14.66**
7	499.33	241.35	68.78	**16.76**
8	499.33	241.35	241.22	**16.72**
9	425.00	170.00	155	**12.93**
10	300.00	170.00	155	**23.12**
11	550.00	170.00	155	**12.16**
12	425.00	50.00	155	**14.70**
13	425.00	290.00	155	**23.12**
14	425.00	170.00	10	**22.76**
15	425.00	170.00	300	**14.92**

Table 4.22. Second DOE for the structure of lines with rectangular profile.

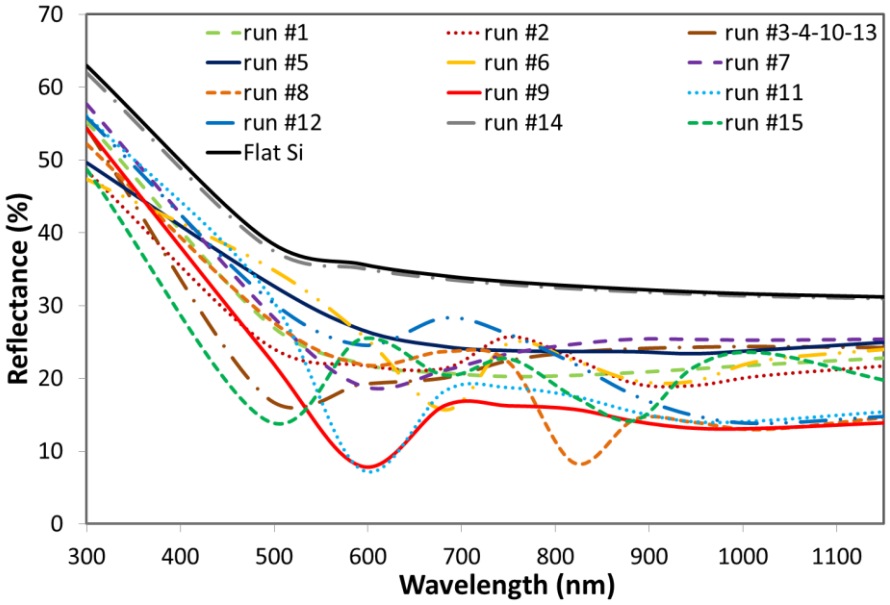

Fig.4. 28. Simulation curves for all the structures in the DOE.

The model obtained for the AWR is summarized in *Table 4.23*. The fit indicators show a better adjustment of the model to the simulation data that the previous DOE (see section 1.1.3.1) with a $R^2 = 0.92$, a $Adj\ R^2 = 0.84$, a $Std\ Error = 1.1$, a $F = 13$ and a $Sig\ F = 5.7 \cdot 10^{-5}$.

The response surface is presented in *Fig.4. 29*. This surface confirms that there is an optimum in the selected range. The dimensions of this optimum are slightly different than those obtained in the first DOE (section 1.1.3.1): a period of 430 nm, a linewidth of 190 nm and a height of 178 nm. The obtained AWR* is 8.57 %.

Model		
Factor	Coeff	P-value
Const	8.82	1.4E-11
p	0.22	4.7E-01
w	-0.64	5.2E-02
h	-1.23	1.3E-03
pw	-0.42	3.0E-01
ph	-0.57	1.7E-01
hw	-0.13	7.4E-01
pwh	-0.24	5.4E-01
pp	0.50	9.2E-02
ww	1.27	5.6E-04
hh	2.43	1.2E-06

Fit Indicators	
R^2	9.2E-01
Adj R^2	8.4E-01
Std Error	1.1E+00
F	1.3E+01
Sig F	5.7E-05

Table 4.23. Predictive model for the AWR of the structure of rectangular lines.

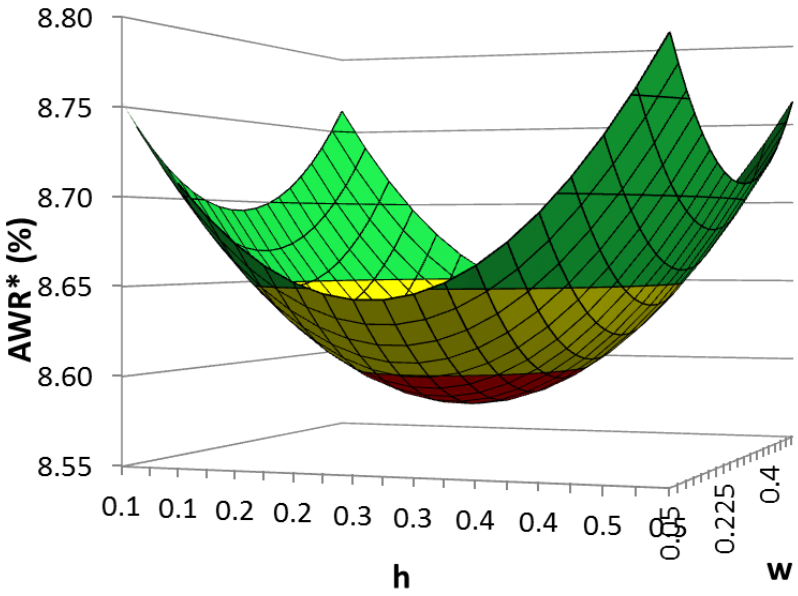

Fig.4. 29. Response surface for a constant value of period. The minimum corresponds with a period of 430 nm, a diameter of 190 nm and a height of 178 nm (normalized values of 0.064, 0.28 and 0.27 respectively).

1.2.1.2. 2D circular pillars in square lattice

The runs of the second DOE defined for this structure are summarized in *Table 4.24*. The period has studied between 430.4 nm and 502.63 nm, the diameter between 238.51 nm and 330 nm and the height between 130.4 nm and 202.63 nm.

# run	Period (nm)	Linewidth (nm)	Heigth (nm)	AWR (%)
1	430.40	238.51	130.40	**4.61**
2	430.40	238.51	202.63	**5.93**
3	430.40	330.00	130.40	**3.10**
4	430.40	330.00	202.63	**7.89**
5	502.63	238.51	130.40	**5.92**
6	502.63	238.51	202.63	**5.89**
7	502.63	330.00	130.40	**3.17**
8	502.63	330.00	202.63	**4.87**
9	475	295	175	**3.87**
10	400	295	175	**4.39**
11	550	295	175	**6.13**
12	475	200	175	**5.23**
13	475	390	175	**6.05**
14	475	295	100	**6.24**
15	475	295	250	**7.59**

Table 4.24. Second DOE developed for the structure of circular pillars on square lattice.

The simulated reflectance for all the runs in the DOE is represented in *Fig.4.30* and the AWR values in the last column of *Table 4.24*. The model obtained from these values is summarized in *Table 4.25* together with the fit indicators.

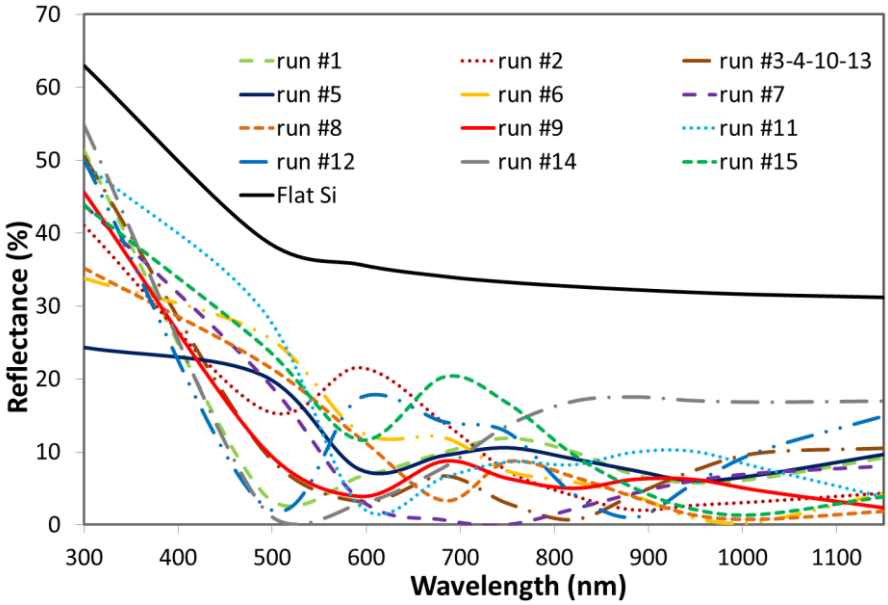

Fig.4.30. Simulation curves for all the runs of the second DOE for the structure of circular pillars in square lattice.

Model			Fit Indicators	
Factor	Coeff	P-value		
Const	3.88	2.7E-09	**R^2**	8.3E-01
p	0.09	6.6E-01	**Adj R^2**	6.9E-01
w	-0.14	5.0E-01	**Std Error**	7.5E-01
h	0.74	3.5E-03	**F**	5.9E+00
pw	-0.53	7.1E-02	**Sig F**	2.7E-03
ph	-0.55	6.0E-02		
hw	0.65	3.1E-02		
pwh	-0.22	4.4E-01		
pp	0.31	1.3E-01		
ww	0.44	3.8E-02		
hh	0.89	4.9E-04		

Table 4.25. Parameters of the model of the AWR of the circular pillars in square lattice.

The response surface of *Fig.4.31* has a minimum at a period of 448 nm, a diameter of 325 nm and a height of 138 nm. The corresponding structure is considered, in this work, as the optimum PC to absorb light in Si substrates in the wavelength range of performance of bulk solar cells.

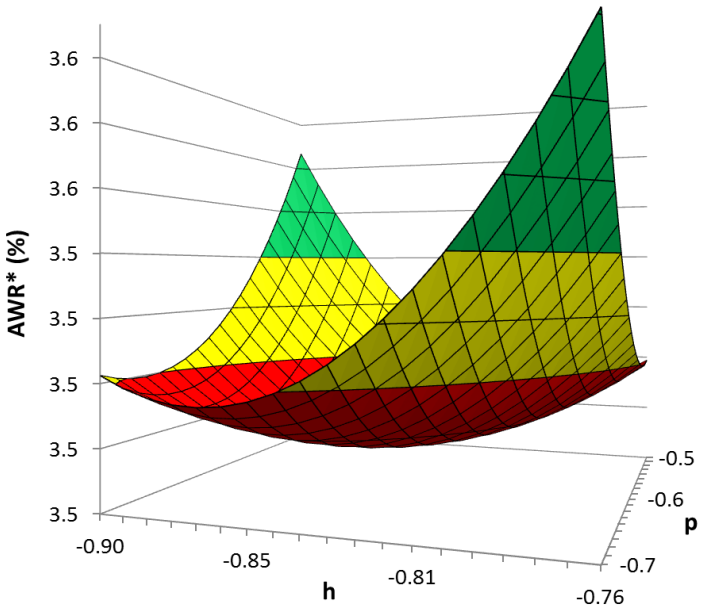

Fig.4.31. Response surface for the structure of circular pillars on square lattice. There is an absolute minimum at a period of 448 nm, a diameter of 325 nm and a height of 138 nm (Normalized values of -0.59, 0.54 and -0.83 respectively).

1.2.2. Fabrication and characterization processes

The results and discussion related to the ultimate designs, fabrication and characterization processes have been published in two articles in the journal *Photonic and Nanostructures – Fundamentals and Applications*. In the first one, we present the results correspond to the 1D structures and in the second one the results correspond to the 2D structures. These two publications are presented below.

PUBLICATION 1: Optimization of 1D photonic crystals to minimize the reflectance of silicon solar cells

PUBLICATION 2: Design, optimization and fabrication of 2D photonic crystals for solar cells

Domínguez, S., García, O., Ezquer, M., Rodríguez, M., Lagunas, A., Pérez-Conde, J., &… Bravo, J. (2012). Optimization of 1D photonic crystals to minimize the reflectance of silicon solar cells. *Photonics and Nanostructures – Fundamentals and Applications*, 1046-53. doi:10.1016/j.photonics.2011.07.001

Este artículo ha sido eliminado por restricciones de derechos de autor.

upna Universidad Pública de Navarra Nafarroako Unibertsitate Publikoa

Domínguez, S., Cornago, I., García, O., Ezquer, M., Rodríguez, M., Lagunas, A., &... Bravo, J. (2013). Design, optimization and fabrication of 2D photonic crystals for solar cells. *Photonics And Nanostructures - Fundamentals And Applications*, 1129-36. doi:10.1016/j.photonics.2012.07.002

Este artículo ha sido eliminado por restricciones de derechos de autor.

upna Universidad Pública de Navarra Nafarroako Unibertsitate Publikoa

2. INTEGRATION OF SOLAR CELLS WITH NANOSTRUCTURES

In this section we present the results related with the integration of solar cells on nanostructured c-Si substrates. There are two objectives: the fabrication of periodic nanostructures on the unpolished Si substrates (USS) typical of the PV industry and the integration of solar cells on these nanostructured USS.

To accomplish these objectives, first we have adjusted the PC design of the previous section taking into account some integration aspects. Then, we have integrated solar cells on Si substrates nanostructured with this adjusted design. We have used polished Si substrates at the beginning as a first approximation and USS like those used in the industry to conclude.

2.1. ADJUSTMENTS IN THE PC DESIGN.

The solar cell surface is the key of the light absorption in the device. Consequently, as explained in the previous chapter, we have developed a deep optimization of the front texturization. The optimum structure found is a pattern of circular pillars repeated in a square lattice with a period of 448 nm, a diameter of 325 nm and a height of 138 nm. Prior to the integration of this structure in a solar cell, we have adjusted its dimensions according to some integration processes.

First, the silicon nitride (SiN_x) passivation layer (see chapter 3) is a new optical interface so it affects the final surface reflectivity. Second, the solar cell area needs to be fully covered with nanostructures to minimize the surface reflection and, as explained in chapter 3; the nanostructured area depends on the period of the PC. However, typical substrates used in PV show areas as big as 15.6 cm x 15.6 cm, which is not covered with the optimum period of 448 nm.

Attending these two considerations, the optimum PC has been adjusted. To keep this redesign as simpler as possible, the geometry of the nanostructure has been maintained as circular pillars disposed in square lattice. Only the sizes, i.e. period, linewidth and height, have been modified.

2.1.1. Adjustment according to the passivation layer

Optical behavior of the nanostructures will depend on the thickness of SiNx passivation layer deposited on top. Therefore, a new optimization of the structure of circular pillars in square lattice considering this new parameter has been developed. Hence, we have defined a new DOE, this time a 3-level CCD with four input variables: the period, the diameter, the height and the SiNx layer thickness (t). With these parameters the DOE of 25 runs summarized in *Table 4.26* is obtained. The period has been varied between 300 nm and 500 nm, the diameter between 90 nm and 310 nm, the height between 65 nm and 155 nm and the SiNx thickness between 15 nm and 105 nm.

# run	Period (nm)	Diameter (nm)	Heigth (nm)	SiNx Thickness (nm)	AWR (%)
1	350.00	150.00	90.00	40.00	**4.38**
2	350.00	150.00	90.00	80.00	**0.83**
3	350.00	150.00	130.00	40.00	**2.02**
4	350.00	150.00	130.00	80.00	**0.68**
5	350.00	250.00	90.00	40.00	**3.21**
6	350.00	250.00	90.00	80.00	**1.38**
7	350.00	250.00	130.00	40.00	**2.16**
8	350.00	250.00	130.00	80.00	**1.70**
9	450.00	150.00	90.00	40.00	**6.74**
10	450.00	150.00	90.00	80.00	**1.36**
11	450.00	150.00	130.00	40.00	**4.16**
12	450.00	150.00	130.00	80.00	**0.78**
13	450.00	250.00	90.00	40.00	**4.29**
14	450.00	250.00	90.00	80.00	**0.87**
15	450.00	250.00	130.00	40.00	**1.81**
16	450.00	250.00	130.00	80.00	**0.52**
17	400.00	200.00	110.00	60.00	**0.74**
18	289.33	200.00	110.00	60.00	**1.61**
19	510.67	200.00	110.00	60.00	**2.15**
20	400.00	89.33	110.00	60.00	**3.19**
21	400.00	310.67	110.00	60.00	**1.96**
22	400.00	200.00	65.73	60.00	**2.94**
23	400.00	200.00	154.27	60.00	**0.36**
24	400.00	200.00	110.00	15.73	**4.99**
25	400.00	200.00	110.00	104.27	**0.81**

Table 4.26. DOE developed to optimize the structure of pillars considering the SiNx layer thickness.

All the combinations of parameters of the DOE have been simulated and the best reflectance curves obtained are shown in *Fig.4.32*. As expected, the passivation layer reduces the reflectance to very low values, in some cases under 2% from 500 nm to 1150 nm (runs #14, #23 and #25).

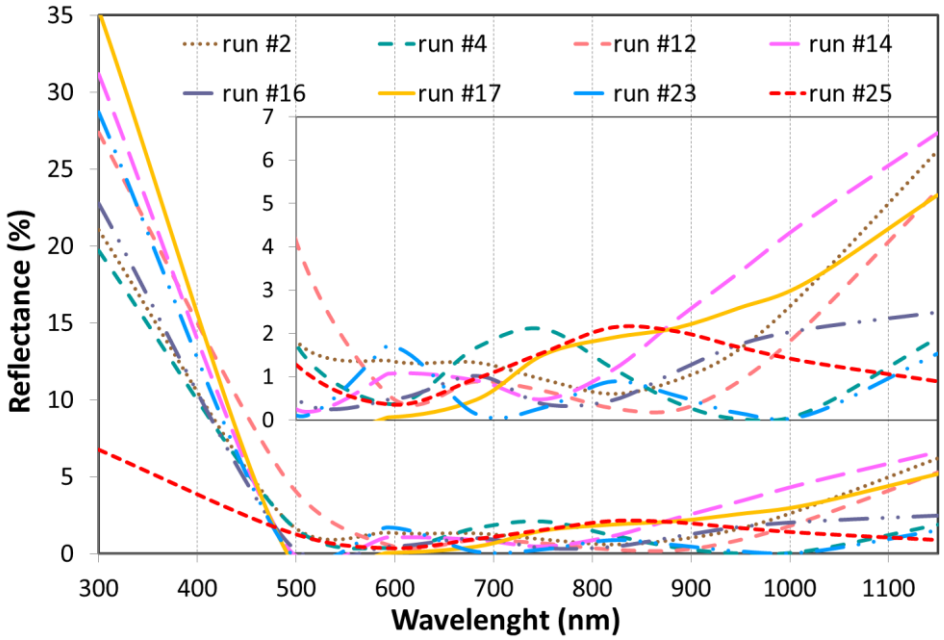

Fig.4.32. Reflectance simulations of the best structures of the DOE. There is a more detailed inset at the right part of the graph for wavelengths from 500 nm.

We have multiplied these curves by the weighting curve and then we have calculated the average of these curves obtaining the values of the last column of *Table 4.26*. Using this data as the output in the RSM, the model summarized in *Table 4.27* is obtained. The indicators of the table on the right show a good fit of the model, with an adjusted R^2 = 0.95, a F = 32 and a very low Sig F.

The partial derivatives of the polynomial model of *Table 4.27* have been calculated to find the minimum, which is found at p = 455.6 nm, w = 166.8 nm, h = 84.24 nm and t = 114.16 nm. This minimum can be seen in the surface of *Fig.33*, which corresponds to the representation of the model along the height and the SiNx thickness for the optimum values of period and diameter.

Model		
Factor	Coeff	P-value
Const	0.78	1.3E-05
A	0.21	1.0E-02
B	-0.30	8.2E-04
C	-0.58	1.4E-06
D	-1.16	3.5E-10
AB	-0.38	8.0E-04
AC	-0.17	7.2E-02
AD	-0.39	6.2E-04
BC	0.13	1.6E-01
BD	0.42	3.9E-04
CD	0.48	1.0E-04
ABC	-0.09	3.2E-01
ABD	0.09	3.3E-01
ACD	0.04	6.9E-01
BCD	-0.04	6.3E-01
ABCD	0.06	4.9E-01
AA	0.27	2.4E-04
BB	0.41	3.7E-06
CC	0.22	1.2E-03
DD	0.48	7.2E-07

Fit Indicators	
R^2	9.8E-01
Adj R^2	9.5E-01
Std Error	3.5E-01
F	3.2E+01
Sig F	5.6E-08

Table 4.27. Model obtained for the average weighted reflectance.

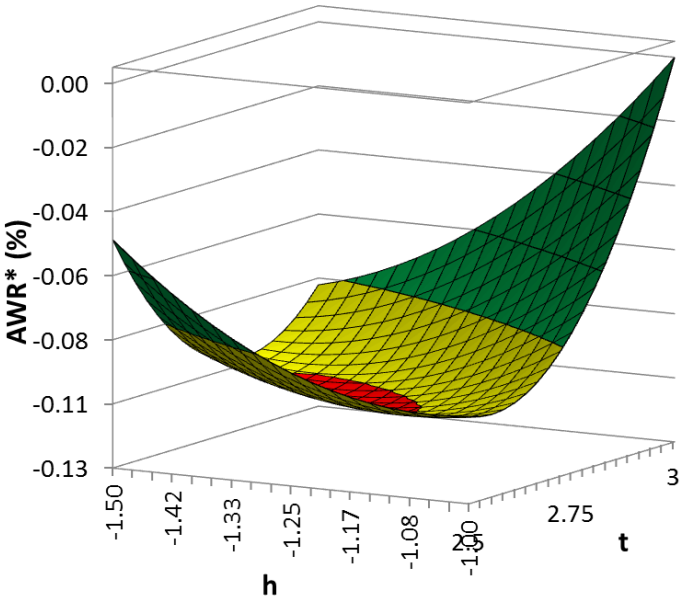

Fig.33. Response surface of the model along the height and the SiNx thickness for the optimum values of period and diameter. The optimum is at 456 nm of period, 167 nm of diameter, 84 nm of height and 114 nm of SIN_x thickness (The normalized values are 1.11, -0.66, -1.29 and 2.71 respectively).

2.1.2. Adjustment according to the substrate size

Typical substrates used in the PV industry are 180 µm thickness 15.6 cm x 15.6 cm substrates with 750 nm average RMS roughness and 4.44 µm average maximum peak to valley distance (MPTVD) on its front surface. In contrast, the fabrication processes in this work (see *chapter 3*) are optimized for 10 cm of diameter circular polished Si wafers. Therefore, an adaptation of the fabrication processes is required.

On the one hand, the deposition by spin coating is optimized for circular wafers. In the case of square substrates, the edge of the substrates is not well covered so there will not be nanostructures there. However this is not of great significance because the cell analysis is done in a square some millimeters smaller than the substrate.

On the other hand, the nanostructured area obtained with the LM is limited, as explained in chapter 2, by the length of the mirror, the wavelength of the laser and the period of the final structure. According to this, the maximum nanostructured area achievable with the wavelength of the laser (325 nm), the length of the mirror (15 cm) and the period of the optimum structure (456 nm) is 5.72 cm x 5.72 cm, which is really far from the objective of 15.6 cm x 15.6 cm. Ideally, we should go for a period of 225 nm to achieve a 15.6 cm x 15.6 cm nanostructured area.

However, the homogeneity in pillar diameters along such a large area is not good enough with our fabrication process. Besides, the simulation results obtained for a 225 nm period was not as good as the result for higher periods. Therefore, we have selected a compromise solution: a period of 375 nm, which allows a 7.2 cm x 7.2 cm nanostructured area so the cell can be almost fully covered in 4 steps.

This means that each quarter of the substrate are exposed to the LM light, as usual, in two orthogonal expositions while the other three quarters are covered preventing from light exposition. This process is repeated for the four quarters of the substrate covering a total area of 14.4 cm x 14.4 cm. The 0.6 cm width unexposed band at the edge of the 15.6 cm x 15.6 cm substrate is not a problem because this area is defective indeed due to the spin coating of square substrates.

Therefore, the optimum structure was forced to have a period of 375 nm. With this period, the optimization process of the other dimensions, i.e. diameter, height and

SiNx thickness has been repeated. Since the period is fixed, there are three input parameters so the DOE has 15 runs (*Table 4.28*). The diameter has been varied between 100 nm and 350 nm, the height between 10 nm and 300 nm and the SiNx thickness between 0 and 200 nm.

# run	Period (nm)	Diameter (nm)	Heigth (nm)	AWR (%)
1	150.67	68.78	40.54	**8.54**
2	150.67	68.78	111.89	**10.77**
3	150.67	172.24	40.54	**19.38**
4	150.67	172.24	111.89	**19.38**
5	239.87	68.78	40.54	**17.60**
6	239.87	68.78	111.89	**13.34**
7	239.87	172.24	40.54	**12.64**
8	239.87	172.24	111.89	**8.87**
9	225	155	100	**3.25**
10	100	155	100	**17.47**
11	350	155	100	**13.15**
12	225	10	100	**19.49**
13	225	300	100	**19.61**
14	225	155	0	**19.26**
15	225	155	200	**9.85**

Table 4.28. DOE for the structure of circular pillars in square lattice with 375 nm of period considering the SiNx passivation layer.

The simulation results obtained for each one of the runs of the DOE are shown in *Fig.4.34* for the bandwidth of performance of bulk Si solar cells (300 nm – 1150 nm). From these curves, the AWR has been calculated (*Table 4.28*) and with this, the model of *Table 4.29* is obtained. The fit indicators show a good agreement between the model and the simulation data.

The model of *Table 4.29* is represented as a surface dependent on the dimensions (diameter and height) in *Fig.4.35*. The minimum value of AWR* is 3.05 % and it corresponds to the new optimum dimensions: a diameter of 199 nm, a height of 171 nm and a SiNx thickness of 85.7 nm.

The simulated reflectance of this optimum is shown in *Fig.4.36*. The reflectance is under 10% along all the wavelength range and under 2.5% from 600 nm. Besides, there are two points of almost zero reflectance at 680 nm and 750 nm.

As a conclusion, the optimum structure considered for the integration process is a pattern of circular pillars, with 199 nm of diameter and 171 nm of height, arranged in a square lattice of period 375 nm.

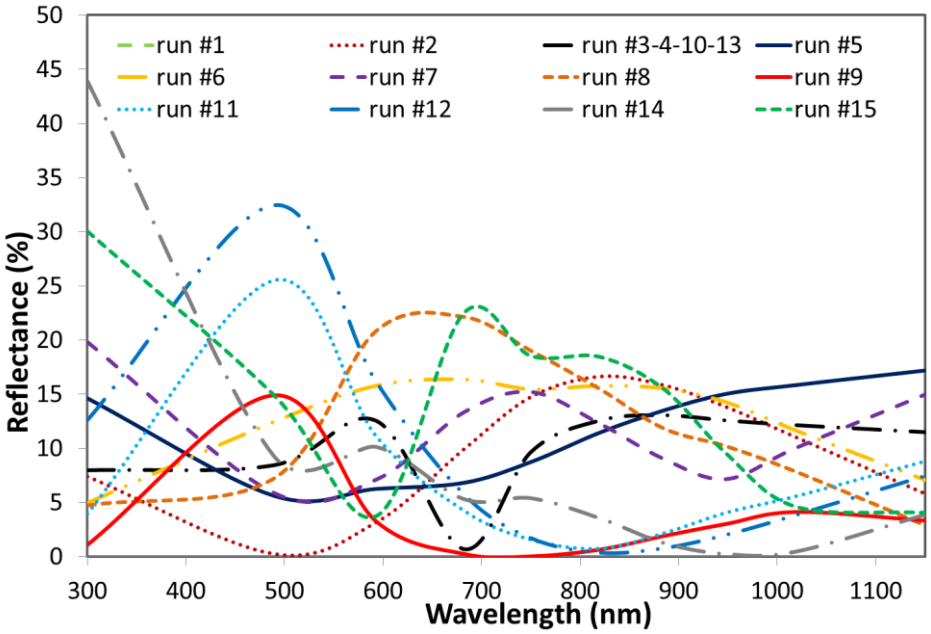

Fig.4.34. Simulated reflectance for all the structures of the DOE.

Model			Fit Indicators	
Factor	Coeff	P-value		
Const	2.033	4.6E-04	**R^2**	8.4E-01
p	0.746	5.3E-02	**Adj R^2**	7.0E-01
w	-0.373	3.0E-01	**Std Error**	1.3E+00
h	1.09386	8.3E-03	**F**	6.2E+00
pw	0.093	8.4E-01	**Sig F**	2.0E-03
ph	0.74734	1.2E-01		
hw	-0.07782	8.7E-01		
pwh	0.04228	9.3E-01		
pp	0.844	2.2E-02		
ww	0.995	9.3E-03		
hh	1.698	1.9E-04		

Table 4.29. Model constructed for the reflectance of the structure of circular pillars distributed in hexagonal lattice with 375 nm of period.

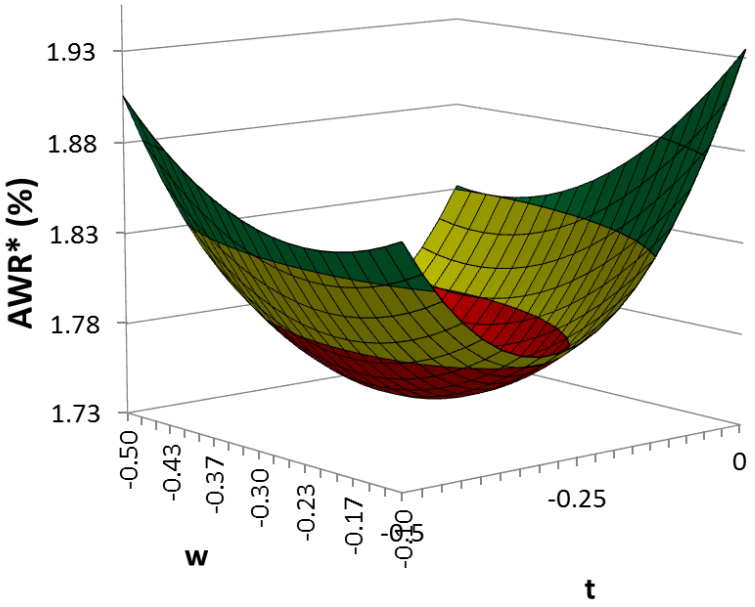

Fig.4.35. Surface model for the reflectance of the optimum structure with 375 nm of period as a function of its diameter and height. The optimum structure has a normalized diameter of -0.34 (199 nm) and a normalized height of -0.19 (171 nm) and a normalized SiNx thickness of -0.24 (85.7 nm).

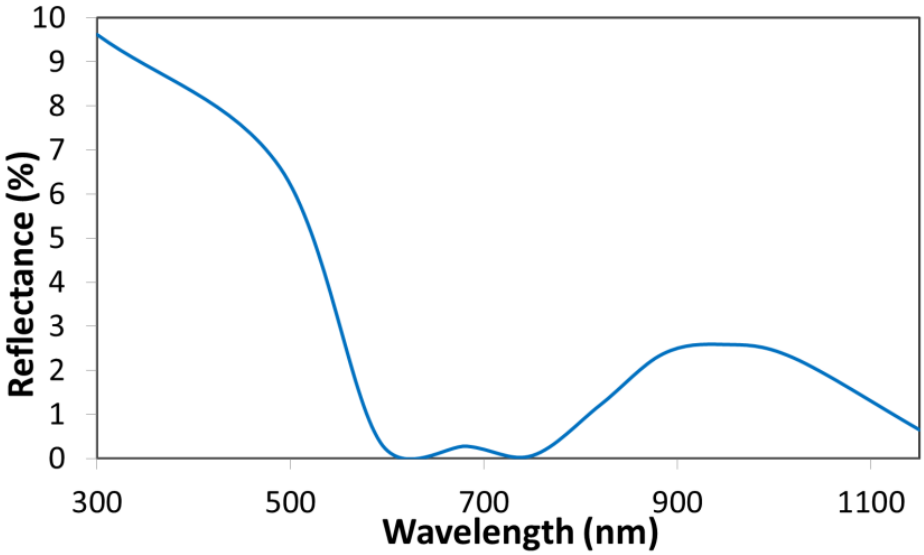

Fig.4.36. Reflectance curves for the optimum structure with p = 375 nm.

2.2. INTEGRATION OF SOLAR CELLS ON POLISHED SUBSTRATES.

The first integration of a nanostructured solar cell of this work has been done on 10.3 cm x 10.3 cm polished substrates as a first approximation to industrial substrates. The nanostructure has been fabricated as explained in the previous section with four series of expositions. As a result, a mark between the nanostructured quarters appears in the substrate as shown in *Fig.4.37*.

In the figure, the substrate is observed at three different moments of the process: after the nanostructures fabrication, after the SiNx deposition and at the end of the integration. After the SiNx deposition, the substrate is darker due to the antireflective effect of the layer. The reflectance at these three stages is shown in *Fig.4.38*. As expected, the lower reflectance is measured after the SiNx because the structure is optimized for this point. After the metallization, logically the reflectance slightly increases.

The measured reflectance is not as low as the simulated values obtained (*Fig.4.36*). This is due to defects inherent to the fabrication process and to the size decrease of the nanostructures during the integration due mainly to the phosphor-silicate glass (PSG) removal. Consequently, as it will be explained in the next section, the nanostructures have been oversized in both diameter and height in subsequent processes.

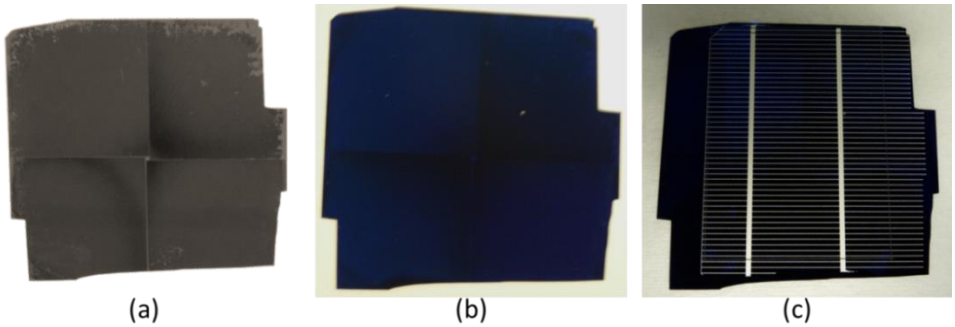

Fig.4.37. Si substrate after different stages of the process: after nanostructures fabrication (a), after SiNx deposition (b) and after final integration.

The electrical parameters obtained are summarized in *Table 4.30* and the I-V curve is shown in *Fig.4.39*. The measurements have been carried out at standard test conditions (STC): irradiation of 1000W/m^2, temperature of 25°C and AM1.5G sunlight spectrum. The results confirm that the solar cell has been successfully integrated. The high value of the fill factor (FF), 76.8% confirms the good series resistance and the final efficiency of 14.92 % confirms the compatibility between the nanostructures and the integration process.

Voc (mV)	Jsc (mA/cm^2)	Pmax (W)	Vmax (mV)	Jmax (mA/cm^2)	FF (%)	Sup (cm^2)	Ef (%)
609	31.9	0.84	508	29.30	76.8%	56.28	14.92

Table 4.30. Electrical parameters measured for one of the nanostructured cells fabricated.

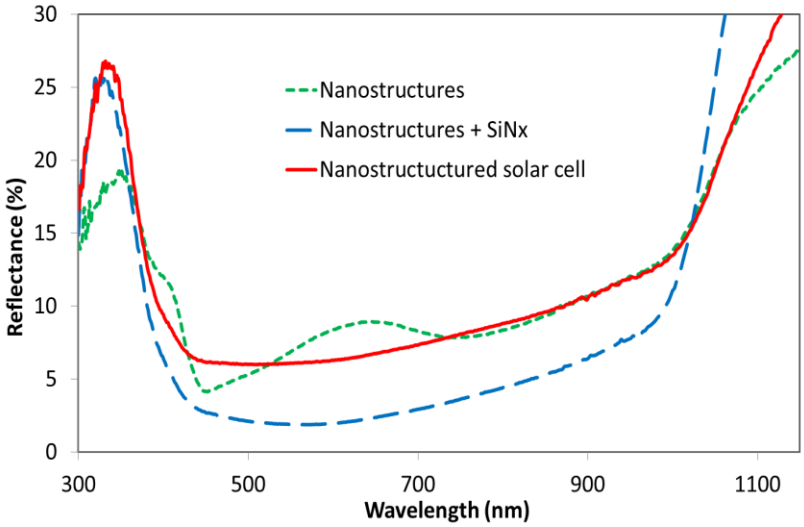

Fig.4.38. Measured reflectance of the nanostructures (green line), the nanostructures with the SiNx on top (blue line) and the final solar cell (red line).

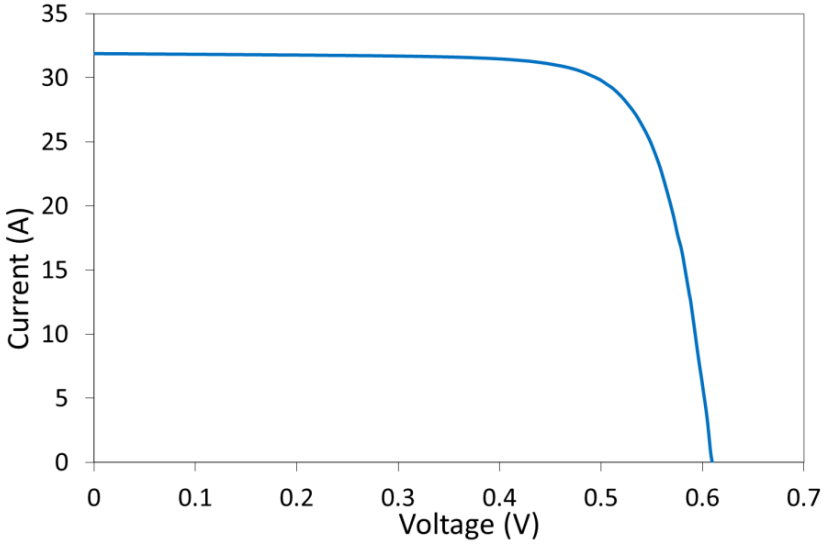

Fig.4.39. I-V curve of the final nanostructured solar cell.

2.3. INTEGRATION OF SOLAR CELLS ON UNPOLISHED SUBSTRATES.

The main result obtained in this section is the successful fabrication of nanostructures on USS typical of the PV industry and the subsequent integration of these nanostructured USS in solar cells following conventional processes. These results have been published in the journal *Nanotechnology* and the article is presented below.

PUBLICATION 3: Periodic nanostructures on unpolished substrates and their integration in solar cells

Cornago, I., Dominguez, S., Bravo, J., Ezquer, M., Rodríguez, M., Lagunas, A., & Rodriguez, R. (2015). Periodic nanostructures on unpolished substrates and their integration in solar cells. *Nanotechnology*, 26 (9), doi:10.1088/0957-4484/26/9/095301

Este artículo ha sido eliminado por restricciones de derechos de autor.

upna Universidad Pública de Navarra Nafarroako Unibertsitate Publikoa

3. NANOSTRUCTURES FOR BROADBAND ANTIREFLECTION

In this section we present the results of the design and fabrication of novel nanostructures to achieve broadband ultra-low reflection. The work was developed at the Massachusetts Institute of Technology and the results have been published in the *Journal of Vacuum Science and Technology B*. The corresponding manuscript is presented below.

PUBLICATION 4: Simple fabrication of ultrahigh aspect ratio nanostructures for enhanced antireflectivity.

Simple fabrication of ultrahigh aspect ratio nanostructures for enhanced antireflectivity

Sagrario Dominguez[a)]
CEMITEC, Noain 31110, Spain and Department of Mechanical Engineering, Massachusetts Institute of Technology, Cambridge, Massachusetts 02319

Ignacio Cornago and Javier Bravo
CEMITEC, Noain 31110, Spain

Jesus Pérez-Conde
Department of Physics, Universidad Pública de Navarra, 31006 Pamplona, Spain

Hyungryul J. Choi and Jeong-Gil Kim
Department of Mechanical Engineering, Massachusetts Institute of Technology, Cambridge, Massachusetts 02319

George Barbastathis
Department of Mechanical Engineering, Massachusetts Institute of Technology, Cambridge, Massachusetts 02319; Singapore-MIT Alliance for Research and Technology (SMART) Center, Singapore 117543; and Shanghai Jiao Tong University–University of Michigan Joint Institute, Shanghai 200240, China

(Received 31 January 2014; accepted 11 March 2014; published 26 March 2014)

In this work, the authors present a novel fabrication process to create periodic nanostructures with aspect ratio as high as 9.6. These nanostructures reduce spectral reflectance of silicon to less than 4% over the broad wavelength region from 200 to 2000 nm. At the visible range of the spectrum, from 200 to 650 nm, reflectivity is reduced to less than 0.1%. The aspect ratio and reflectance performance that the authors achieved have never been reported before for ordered tapered nanostructures, to our knowledge. © *2014 American Vacuum Society*. [http://dx.doi.org/10.1116/1.4869302]

I. INTRODUCTION

Nanostructured surfaces have been widely studied to improve the optical properties of both absorptive and transparent materials, such as Si, GaAs, and fused silica.[1–3] Due to the subwavelength feature size, nanostructures behave as an effective medium with a gradient refractive index, suppressing light reflection at material interfaces through adiabatic impedance matching.[1,2,4–6]

In the case of silicon, many efforts have been undertaken to improve light absorption by texturizing the surfaces. Previous reported solutions achieved reflectance under 1% in the visible wavelength region, but extending these properties to broader bands remained challenging.[7,8] Random distributions of tapered nanostructures are preferred to achieve broadband low reflectance. In fact, most of the black silicon fabrication reported in photovoltaic related literature is based on this kind of structures.[9,10] However, low reflectivity is also achievable using periodic nanostructures, which are more advantageous as they are more controllable, reproducible, and eliminate possibilities for scatter.[11,12]

The geometry of the nanostructures is the key to create surfaces with improved optical properties. To minimize light reflection, it is particularly important to gradually taper the structures with small diameter and large height so as to smoothen the refractive index profile: The higher aspect ratio of nanocone structures (i.e., the ratio of nanocone height to the base diameter) the surface has, the less reflectance it exhibits.[2,13,14] With this purpose, high aspect ratio periodic nanocones have been recently fabricated to increase light transmissivity of glass. Using a multiple shrinking mask etching process, nanocones with an aspect ratio as high as 7 have been successfully fabricated directly on top of a fused silica wafer.[15] Nanoimprint lithography has subsequently been used to replicate these structures in alternate materials to improve their reflectivity.[16,17]

In this work, we present a novel fabrication process based on a single shrinking mask etching step to create periodic nanocones with ultrahigh aspect ratios up to 9.6, in order to achieve ultimate antireflectivity on the surface of silicon in a simpler way compared to the previous works. These nanocones exhibit broadband antireflectivity in the wavelength range between 200 and 2000 nm. Besides, in the visible wavelength range, the reflectance is suppressed almost entirely, to less than 0.1%, thanks to the high aspect ratio. The tapered nature of periodic nanocone arrays makes them suitable for nanoimprint lithography for replication in alternate materials, as in our earlier work,[16,17] broadening the possible applications and promoting the scalability of the technology.[18]

II. EXPERIMENT

The optical behavior of different silicon nanocones has been simulated using the FDTD (i.e., finite-difference time-domain) based software OPTIFDTD. In the simulation model, the diameter of the cone base is fixed to be the same as the period and the top of the cone is reduced to a point. While the period of the structure is set to the minimum value achievable with our fabrication method, 170 nm, three

[a)]Electronic mail: sdominguez@cemitec.com

upna Universidad Pública de Navarra Nafarroako Unibertsitate Publikoa
Redistribution subject to AVS license or copyright; see http://scitation.aip.org/termsconditions. Download to IP: 18.7.29.240 On: Wed, 16 Apr 2014 10:49:39

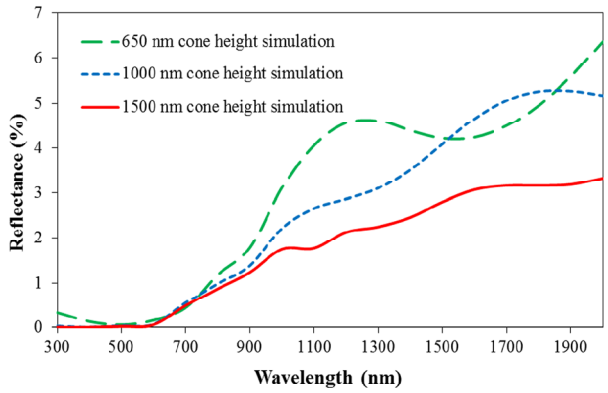

FIG. 1. (Color online) Simulated total reflectance for periodic nanocones with three different heights: 650, 1000, and 1500 nm.

different cone heights are considered. As the height of the cone increases, the change of the effective reflective index between air and silicon becomes smoother and the reflectance occurred at the optical interface decreases, as expected. Figure 1 shows the simulated reflectance for three different heights: 650, 1000, and 1500 nm. The three structures have reflectance lower than 1% between 300 and 800 nm and lower than 7% in the whole studied spectral range from 300 to 2000 nm. Besides, the reflectance is less than 0.1% over the wavelength region from 300 to 600 nm for the nanocones of 1000 nm and 1500 nm height. As expected, minimum reflectance is obtained from the 1500 nm height nanocones, totaling reflected energy of less than 3.5% in the entire simulated range from 300 to 2000 nm.

The height of the nanocone should be chosen according to the desired application. In the case of the photovoltaic field, very high aspect ratio structures are not necessarily required as they can negatively affect the charges collection and recombination.[19,20] Besides, as the silicon band gap is at 1150 nm, it is not necessary to reduce reflectance for higher wavelengths. Therefore, the silicon nanocones of 650 nm or 1000 nm height could be enough for solar cell applications. However, higher aspect ratio is still desirable for applications with more broadband antireflection requirements, such as wide-band detector or microwave absorber.[21,22]

The fabrication process for ultrahigh aspect ratio nanocone arrays is shown in Fig. 2. First, a trilayer for interference lithography is deposited on top of a silicon wafer: an antireflective coating (ARC, XHRiC-16, Brewer Science, Inc.) to minimize the reflection of light during laser exposure, a thin SiO_2 layer for improving the pattern transfer to the ARC, and a negative photoresist layer (THMR-iN PS4 MG, TOKYO OHKA KOGYO CO., LTD) where the pattern is initially recorded. Then, the sample is illuminated with a laser light source at 325 nm wavelength by using a Lloyd's Mirror interferometer lithographic setup, and after that, the exposed photoresist is developed to obtain a periodic array of holes (Fig. 2.1). In the second step (Fig. 2.2), this pattern is transferred to the SiO_2 interlayer and subsequently to the ARC with CF_4 and O_2 reactive ion etching (RIE), respectively. Subsequently, hydrogen silsesquioxane (HSQ14, Dow Corning) is spun on the ARC holes and baked at 200 °C (Fig. 2.3). Part of this layer fills the ARC holes, while the rest remains on top surface of ARC. The HSQ excess layer on top of the ARC is first removed by CF_4 RIE (Fig. 2.4), and then, the remaining ARC is removed by O_2 RIE obtaining a pattern of HSQ posts over the silicon (Fig. 2.5). This pattern is used as a shrinking mask to create the silicon nanocones during HBr RIE (Fig. 2.6). HSQ posts are a good mask since the HSQ etch rate is slower than that of Si

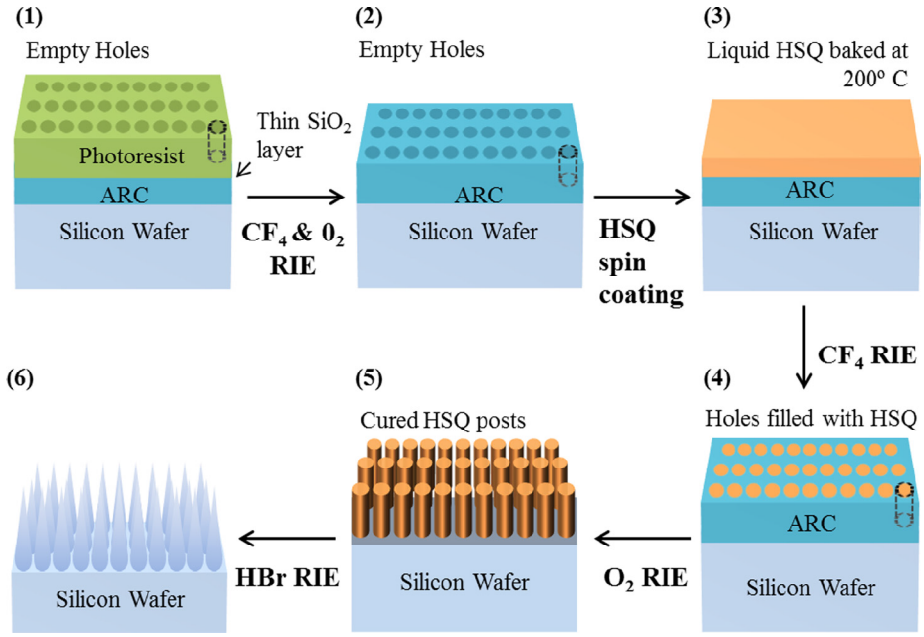

FIG. 2. (Color online) Fabrication process followed to fabricate nanocones with aspect ratios as high as 9.6. The process is based in laser interference lithography (LIL) and RIE.

upna Universidad Pública de Navarra Nafarroako Unibertsitate Publikoa
Redistribution subject to AVS license or copyright; see http://scitation.aip.org/termsconditions. Download to IP: 18.7.29.240 On: Wed, 16 Apr 2014 10:49:39

in HBr plasma, and it also shrinks laterally while Si is etched deeper, enabling conical shaping of the nanostructures.

Depending on the HSQ mask dimensions and HBr RIE conditions, different aspect ratio nanocones can be fabricated. To obtain high aspect ratio, the dimensions of the HSQ posts have to be large enough to resist a deep-transfer process. To maximize the diameter, we use a negative photoresist and the HSQ image reverse process explained before due to the limitation on feature sizes of positive photoresists.[15] The HSQ posts height is limited by the ARC thickness used in the interference lithography process.

Etching conditions have to be optimized to obtain the optimal shrinking speed of the HSQ mask, to reach the desired structure. 9.6 aspect ratio nanocones with a period of 170 nm and a height of 1640 nm have been fabricated during 25 min of 20 sccm HBr etching process with a chamber pressure of 20 mTorr and a power of 150 W.

III. RESULTS AND DISCUSSION

Cross-sectional scanning electron micrographs of three different patterns of HSQ posts on silicon substrates are shown in Figs. 3(a)–3(c). The nanocones obtained by using each of these patterns as the mask during the HBr RIE are shown in Figs. 3(d)–3(f). All the structures have a period of 170 nm, which is the minimum value achievable with laser interferometer lithography at 325 nm of wavelength. Starting with a 100 nm height HSQ posts mask, nanocones of 650 nm height are created. When the mask height is increased to 140 and 200 nm, the height of nanocones can be increased up to 1000 nm and 1640 nm, respectively. In all cases, the cones were fabricated so as to have a linear graded profile, because the etch rates of HSQ posts and silicon during RIE process were optimized to be constant. The diameter of the structures ranges from 170 nm at the bottom, where adjacent cones are touching each other, to less than 20 nm at the sharp tip at the top. Thus, we achieve a gradual and slow variation of the effective refractive index from the index of air on the tip of the cone to the index of silicon on the base.

Reflectance measurements of the nanostructured surface with 1640 nm height nanocones over a wavelength range from 200 to 2000 nm are presented in Fig. 4. A spectrophotometer (JASCO V-670) with an integrating sphere (JASCO ISN-723) was used to measure the total reflectance which is the sum of the specular and the diffuse components. Specular reflectance corresponds to the light coming back from the surface at the normal direction of the surface (0°), and it is under 4% between 200 and 2000 nm. This means a drastic reduction of silicon reflectance, whose general value is around 30% in the same spectral range with polished surface.

To separate specular from diffuse reflectance, we tilted the sample by a small angle relative to the tangential orientation with respect to the integrating sphere's entrance aperture. Thus, the light is normally incident so specular reflection goes backward toward the source and is rejected by the sphere. Due to the tilt of the sample, a small part of the diffuse light misses the entrance to the integrating sphere, while most of it finds its way in. Since the tilt required for the sample in our apparatus is small (∼5°), the solid angle subtended that misses the integrating sphere's entrance is approximately 1% of 4π. Further, assuming the diffuse light to be quasi-isotropically distributed, the same estimate of 1% should correspond to the loss of diffuse light in our approach.

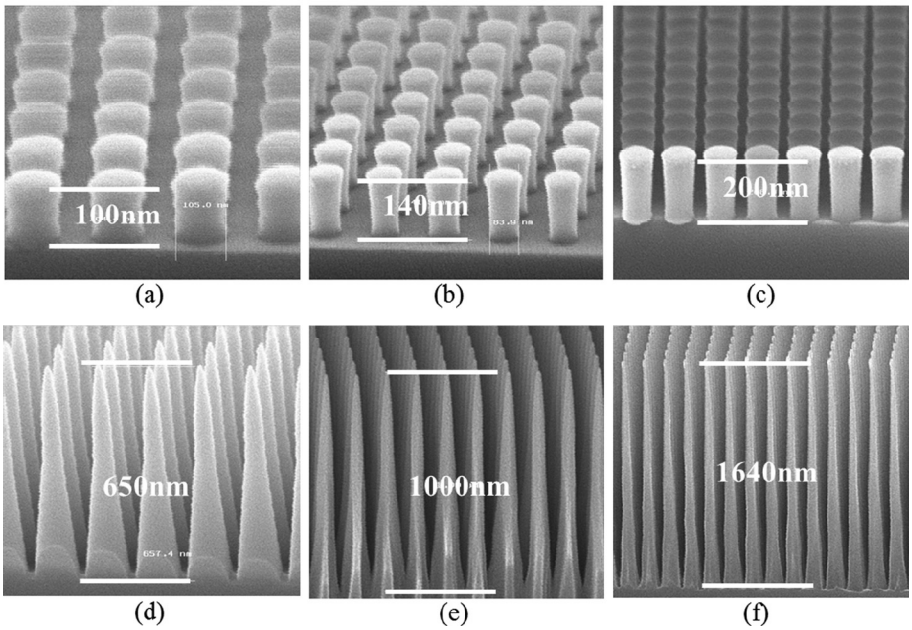

FIG. 3. Cross-sectional scanning electron micrographs of three HSQ posts masks used in the HBr RIE process and of the three different final nanocone patterns. Three different heights of HSQ posts have been used: (a) 100 nm, (b) 140 nm, and (c) 200 nm and three different heights have been obtained: (d) 650 nm, (e) 1000 nm and (f) 1640 nm, respectively. All nanostructures have a period of 170 nm.

upna Universidad Pública de Navarra Nafarroako Unibertsitate Publikoa
Redistribution subject to AVS license or copyright; see http://scitation.aip.org/termsconditions. Download to IP: 18.7.29.240 On: Wed, 16 Apr 2014 10:49:39

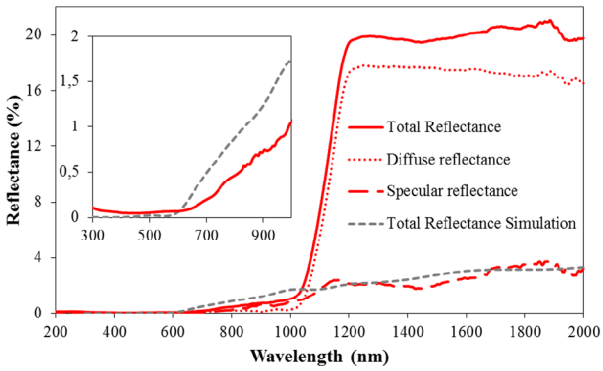

FIG. 4. (Color online) Summed specular and diffuse reflectance measurements for periodic patterns of 9.6 aspect ratio nanocones with a period of 170 nm and a height of 1640 nm. Simulation results of the total front-side reflectance are also shown for comparison. In the left inset, a more detailed graph for both the measurements and the simulation of the total reflectance between 300 and 1000 nm is shown.

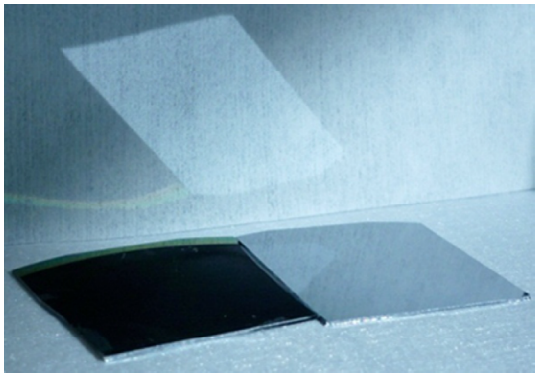

FIG. 5. (Color online) Comparison between samples of silicon patterned with a periodic array of cones with a period of 170 nm and a height of 1640 nm (aspect ratio of 9.6) on the left and an untreated polished crystalline silicon on the right. At the back, the reflected image of the samples can also be observed when the sample is illuminated by sunlight.

With these caveats, the result of the integrating sphere measurement for diffuse reflectance (i.e., light backscattered at all angles from −90° to 90° except the specular reflection direction) is less than 0.5% at wavelengths from 200 nm to 1050 nm, where it abruptly increases to approximately 18%.This steplike behavior of the curve is due to nonabsorbed light reflecting on the backside of the silicon wafer. For wavelengths higher than 1050 nm, light is not absorbed in the silicon, so it goes through the wafer reflecting again at the optical interface between the backside of the silicon wafer and the air.[23,24] The silicon wafers used for sample fabrication are single side polished, and they have a rough back surface. The light reflected from the back is diffused so that there is no abrupt rise around 1050 nm of wavelength in the specular reflectance measurements. If the goal is to have broadband antireflection, nanocones could be patterned at both sides of the wafer to let the light pass through the substrate.[6] Total reflectance corresponds to the light coming back at any angle, and it is the sum of both the specular and the diffuse components. Therefore, it also exhibits the same sharp rise at around 1050 nm due to diffuse backside reflection. Simulation data of the total reflectance are also shown in Fig. 4 for comparison. In the simulation, only the reflectance from the front surface was considered, so as to avoid the diffuse backside reflection effect. Therefore, the simulation is only comparable with the experimental total reflectance until 1050 nm. In the left inset of Fig. 4, both curves are shown in detail between 300 and 1000 nm. Reflectance is under 1% in that region being depicted and under 0.2% between 300 and 700 nm. The slight differences between simulation and measurements in this wavelength range could be due to the defects introduced in the fabrication process that are not considered in the simulation model. For longer wavelengths, the good agreement between the simulation and the specular measurements give us confidence that the diffuse component coming from the front surface is very low and the total reflectance from the front surface is also less than 4% until 2000 nm. This is one of the best antireflection results for silicon in the literature, to our knowledge.

The almost complete suppression of reflectivity in the range of visible wavelengths leads to the black appearance of the silicon sample shown in Fig. 5. A piece of the sample with 1640 nm height nanocones, in the left, is shown together with a flat silicon surface, in the right, for comparison. In the back of the image, the reflection of the samples illuminated by sunlight can also be observed. While there is a bright reflection coming from the polished surface, no reflection can be seen from the nanocone-patterned silicon.

IV. SUMMARY AND CONCLUSIONS

As a conclusion, periodic nanocone patterns have been fabricated following a simple method which allows to create slender nanostructures with aspect ratios as high as 9.6. These nanocones drastically reduce reflectance to values under 4% in the broadband wavelength range between 200 and 2000 nm and under 0.2% in the visible range of light. Both the aspect ratio and the reflectance results have never before been reported for ordered structures, to our knowledge. The fabricated high aspect ratio nanocone arrays are superior in terms of antireflectivity, and the simple fabrication process implemented here is promising for applications such as photovoltaic cells and wide-band sensors or absorbers.

ACKNOWLEDGMENTS

The authors would like to thank the staff and facility support from the Nano Structures Laboratory at MIT, especially T. A. Savas for his continuous help during the processing and for contributions in the HSQ masking process, and J. Daley for all his help in the lab. This work was supported in part by Department of Innovation, Enterprise and Employment of Gobierno de Navarra research Grant 1858/2012, by the MIT Institute for Soldier Nanotechnologies (ISN) under Contract DAAD-19-02D-0002 with the U.S. Army Research Office, and by the Singapore National Research Foundation (NRF) through the Singapore-MIT Alliance for Research and Technology (SMART) Centre.

[1]J. Zhao, A. Wang, M. A. Green, and F. Ferrazza, Appl. Phys. Lett. **73**, 1991 (1998).

upna Universidad Pública de Navarra Nafarroako Unibertsitate Publikoa
Redistribution subject to AVS license or copyright; see http://scitation.aip.org/termsconditions. Download to IP: 18.7.29.240 On: Wed, 16 Apr 2014 10:49:39

[2]K.-C. Park, H. J. Choi, C.-H. Chang, R. E. Cohen, G. H. McKinley, and G. Barbastathis, ACS Nano. **6**, 3789 (2012).
[3]P. L. Gourley, J. R. Wendt, G. A. Vawter, T. M. Brennan, and B. E. Hammons, Appl. Phys. Lett. **64**, 687 (1994).
[4]S. Domínguez, I. Cornago, O. García, M. Ezquer, M. J. Rodríguez, A. R. Lagunas, J. Pérez-Conde, and J. Bravo, Photonics Nanostruct. **11**, 29 (2013).
[5]S. Domínguez, O. García, M. Ezquer, M. J. Rodríguez, A. R. Lagunas, J. Pérez-Conde, and J. Bravo, Photonics Nanostruct. **10**, 46 (2012).
[6]I. Cornago, H. J. Choi, J.-G. Kim, and G. Barbastathis, 38th International Conference on Micro and Nano Engineering, Toulouse, France, 16–20 September 2012.
[7]S. Chattopadhyay, Y. F. Huang, Y. J. Jen, A. Ganguly, K. H. Chen, and L. C. Chen, Mater. Sci. Eng., R **69**, 1 (2010).
[8]L. L. Ma, Y. C. Zhou, N. Jiang, X. Lu, J. Shao, W. Lu, J. Ge, X. M. Ding, and X. Y. Hou, Appl. Phys. Lett. **88**, 171907 (2006).
[9]H. M. Branz, V. E. Yost, S. Ward, K. M. Jones, B. To, and P. Stradins, Appl. Phys. Lett. **94**, 231121 (2009).
[10]S. H. Tan, C. B. Soh, W. Wang, S.-J. Chua, and D. Chi, Appl. Phys. Lett. **101**, 133906 (2012).
[11]K. N. Nguyen, D. Abi-Saab, P. Basset, E. Richalot, F. Marty, D. Angelescu, Y. Leprince-Wang, and T. Bourouina, Microsyst. Technol. **18**, 1807 (2012).
[12]Y. Liu and M. Hong, J. Mater. Sci. **47**, 1594 (2012).
[13]F. Llopis and I. Tobias, J. Appl. Phys. **100**, 124504 (2006).
[14]Y. Li, J. Zhang, and B. Yang, *9th IEEE Conference on Nanotechnology, 2009, IEEE-NANO 2009*, 26–30 July 2009, pp. 1–3.
[15]H. J. Choi, I. Cornago, J.-G. Kim, T. Savas, and G. Barbastathis, *2012 International Conference on Optical MEMS and Nanophotonics (OMN)*, 6–9 Aug. 2012, pp. 1–2.
[16]J.-G. Kim, H. J. Choi, H. Gao, I. Cornago, C.-H. Chang, and G. Barbastathis, *2012 International Conference on Optical MEMS and Nanophotonics (OMN)*, 6–9 Aug. 2012, pp. 71–72.
[17]H. Hauser, B. Michl, S. Schwarzkopf, V. Kübler, C. Müller, M. Hermle, and B. Bläsi, IEEE J. Photovolt. **2**, 114 (2012).
[18]A. A. Letailleur, K. Nomenyo, S. M. Murtry, E. Barthel, E. Søndergård, and G. Lérondel, J. Appl. Phys. **109**, 016104 (2011).
[19]K. Xiong, S. Lu, D. Jiang, J. Dong, and H. Yang, Appl. Phys. Lett. **96**, 193107 (2010).
[20]J. Oh, H.-C. Yuan, and H. M. Branz, Nat. Nanotechnol. **7**, 743 (2012).
[21]D. Rossberg, Sens. Actuators, A **47**, 413 (1995).
[22]X. Liu, Z. Zhang, and Y. Wu, Composites, Part B **42**, 326 (2011).
[23]Y. Kanamori, M. Sasaki, and K. Hane, Opt. Lett. **24**, 1422 (1999).
[24]M.-L. Kuo, D. J. Poxson, Y. S. Kim, F. W. Mont, J. K. Kim, E. F. Schubert, and S.-Y. Lin, Opt. Lett. **33**, 2527 (2008).

upna Universidad Pública de Navarra Nafarroako Unibertsitate Publikoa
Redistribution subject to AVS license or copyright; see http://scitation.aip.org/termsconditions. Download to IP: 18.7.29.240 On: Wed, 16 Apr 2014 10:49:39

CHAPTER 5. CONCLUSIONS

1. CONCLUSIONS

1.1. NANOSTRUCTURES FOR SOLAR CELLS

The first part of the work is focused on the application of nanostructures to solar cells. For this application, we have developed different processes to simulate, optimize and fabricate periodic nanostructures. The main two goals were the improvement of the light absorption of silicon (Si) in the range of performance of Si solar cells and the successful integration of solar cells with nanostructured Si substrates.

There were three different phases in the work: first, an initial study developed on polished Si wafers, second, the adaptation of the processes to the rough Si substrates frequently used in the photovoltaic industry and finally the solar cell integration work. The corresponding conclusions of these different parts are summarized in the following subsections.

1.1.1. Work on polished Si wafers

We have optimized 11 different structures selected according to our fabrication capabilities. These structures consist in either 1D or 2D periodic patterns with periods ranging between 100 and 800 nm. The repeated motifs are lines, pillars or holes with different profiles. The height of the motifs has been ranged between 10 and 300 nm and their sizes between 20 % and 80 % of the lattice period.

We have used computer simulation to calculate the reflectance of the above mentioned periodic nanostructures under light illumination in the range of performance of Si solar cells, i.e. from 300 nm to 1150 nm. The simulation process has been validated by comparison with experimental measurements.

We have developed a process to optimize the dimensions of any designed nanostructure according to the desired optical behavior. In our case, the optimization is done looking at the sunlight radiation spectra and the Si spectral response, weighting more the most energetic wavelength bands in the solar cell conversion. However, the weighting criteria could be changed to optimize nanostructures for other optical application. The optimization process is based on design of experiments (DOE) techniques and computer simulation.

We have obtained optimum dimensions for the 11 structures under study and we have chosen the best one comparing their optical performance for the solar cell application. This optimum structure is a periodic pattern of cylinders ordered in a squared lattice of 448 nm of period. The cylinders have a diameter of 325 nm and a height of 138 nm.

We have fabricated some of the optimized structures on polished Si wafers of 10 cm of diameter. The fabrication processes are based on Laser Interference Lithography (LIL), Reactive Ion Etching (RIE) and wet etching. We have obtained high fidelity between the fabricated structures and the ideal designs. The optimum structure mentioned before reduces the reflectance of the standard texture used in c-Si wafer photovoltaic devices in more than 77%.

1.1.2. Adaptation to industrial substrates

The adaptation of the previous developed processes to the industrial substrates includes the increase of the nanostructured area up to 15.6 cm x 15.6 cm and the fabrication on surfaces with a RMS roughness of 4 µm. On the one hand, we have increased the nanostructured area using a sequence of four Lloyd´s Mirror expositions for each sample. That way, we have fabricated periodic nanostructures with 375 nm of period in areas as big as 14.4 cm x 14.4 cm.

On the other hand, we have changed the fabrication process adding some crucial steps to achieve the fabrication of nanostructures on unpolished substrates with 4 µm of RMS roughness. We have fabricated 375 nm period patterns of nanoposts with diameters of 300 nm and heights of 220 nm. This is the first time to our knowledge that periodic nanopatterns are fabricated on such a rough surface. With these

structures, we have achieved a reflectance under 10 % at normal incidence in the broad wavelength range between 500 and 1000 nm.

1.1.3. Solar cell integration

In the last stage of the present work, we have successfully integrated solar cell on nanostructured substrates. First, we have integrated polished substrates with nanostructures obtaining and efficiency of 14.92 %. Finally, as the culmination of this part of the work, we have integrated nanostructured industrial rough photovoltaic substrates in solar cells. The electrical parameters obtained confirm that the cells have been successfully integrated. The nanostructured cell presents a fill factor of 77.2 %, which confirms the good series resistance and the absence of important shunts; and the final efficiency is 15.56 %. This efficiency value is very promising when it is compared with the results in the nanostructured solar cells recent literature.

1.2. NANOSTRUCTURES FOR BROADBAND ANTIREFLECTION

The second part of the work is focused in the fabrication of ultra-high aspect ratio nanostructures on Si to obtain the lowest possible reflectance in the broadest wavelength band.

To achieve the objective, we have developed a simple fabrication process based on LIL and RIE, which allows the fabrication of periodic nanocones with a reduced period of 170 nm and a height that can be controlled by adjusting the fabrication parameters.

With this process, we have fabricated slender nanocones with aspect ratios as high as 9.6. These nanocones drastically reduce reflectance to values smaller than 4% in the broadband wavelength range between 200 and 2000 nm and under 0.2% in the visible range of light. Both the aspect ratio and the reflectance results have never before been reported for ordered structures, to our knowledge.

2. SIGNIFICANCE AND FUTURE WORK

In the present work we have developed a very useful methodology for the study of nanostructures for a particular application. It includes the design of optimum geometry and dimensions, the simulation of the optical performance and the fabrication and characterization of the structure.

This process could be adapted to study periodic nanostructures for any other application. The optimization process would be equivalent just adjusting the simulation ranges and materials and defining a new criteria to choose between structures, i.e. a new weighting curve for the simulation data post-processing. For example, an obvious application is the thin film based novel solar cells, where light management is the key for a successful performance.

In our case, the work is developed for bulk Si solar cells because we wanted to do a first proof of concept on this well-known technology. Besides, this is the most widespread kind of solar cells in the industry and to improve its efficiency deserves to be investigated. For this application, the next step is the combination of the processes developed in this work. The nanocones that we have fabricated in the second part, with a very good broadband anti-reflection, could be created on unpolished Si substrates by changing some parameters in the last RIE of the process. In this way, the ultimate reflectance would be lower and the final efficiency higher than the one reported in this thesis.

An important step forward in this investigation in the near future is the modification of the fabrication processes to achieve competitiveness in the photovoltaic industry. In this direction, we are now widening our expertise onto roll to roll and nanoimprint technologies, which are more industry oriented.

ACRONYMS, SYMBOLS, FIGURES AND TABLES

1. ACRONYMS AND SYMBOLS

0D - zero dimensional

1D - one dimensional

2D - two dimensional

3D - three dimensional

Adj R^2 - Adjusted coefficient of determination

AlGaAs - aluminum gallium arsenide

APML - anisotropic perfectly matched layer

AR - Antireflective

ARC - antireflective coating

a-Si - amorphous silicon

AWR - average weighted reflectance

AWR* - estimated average weighted reflectance

B - boron

CCD - central composite design

CdS - cadmium sulfide

CdTe - cadmium telluride

CEMITEC - Multidisciplinary center of technologies for the industry

CENER - National renewable energy center

CF_4 - Tetrafluoromethane

Cr - Chromium

c-Si - crystalline silicon

CW - continuous wave

DOE - design of experiments

e-beam - electron beam

EL - electroluminescence image

EM - electromagnetic

EMT - effective medium theory

EQE - external quantum efficiency

FDTD - finite difference time domain

FF - fill factor

FideNa - Foundation for the research and development in Nanotechnology

GaAs - gallium arsenide

Ge - germanium

h - height

HBr - hydrogen bromide

HF - hydrofluoric acid

HSQ - hydrogen silesquioxane

InP - indium phosphide

IQE - internal quantum efficiency

IR - infrared

KOH - potassium hydroxide

LIL - laser interference lithography

LM - lloyd´s mirror

MIT - Massachusetts Institute of technology

MPTVD - maximum peak to valley distance

MZ - mach zehnder

N - number of variables in a design of experiments

n - refractive index

NaOH - sodium hydroxide

$\mathbf{n_{eff}}$ - effective refractive index

NSL - nanostructures laboratory

p - period

P - phosphorus

PBC - periodic boundary condition

PC - photonic crystal

PEC - perfect electric conductor

PECVD - plasma enhanced chemical vapor deposition

PERL - passivated emitter rear locally diffused

PL - Planarization layer

PMC - perfect magnetic conductor

PML - perfectly matched layer

PR - photoresist

PRL - photoresist layer

PSG - phosphor silicate glass

PV - photovoltaic

R^2 - coefficient of determination

RIE - reactive ion etching

RMS - root mean square

RSM - response surface methodology

SEM - scanning electron microcope

Si - silicon

SiNx - silicon nitride

SiO_x - silicon oxide

STC - standard test conditions

Std Error - standard error

SWS - subwavelength structure

TMAH - tetramethylammonium hydroxide

USS - unpolished silicon substrates

UV - ultraviolet

w - width

ε - dielectric permittivity

ε_r - relative permittivity

λ – wavelength

2. INDEX OF FIGURES

upna Universidad Pública de Navarra Nafarroako Unibertsitate Publikoa

3. INDEX OF TABLES

Nanostructures are being widely studied in the scientific community for many different applications because they present novel properties different from those observed in matter at the macroscale. For example, electromagnetic waves interact in an unusual way with periodic nanostructures with sizes in the order of magnitude of the wavelength. Structures with periods in the nanoscale can indeed manage light in the ultraviolet, visible and near infrared regions of the electromagnetic spectrum.

In this work, we use periodic nanostructures to control the optical properties of Si, since it is one of the most common elements in the world and also one of the most used materials in the industry. We focus on the light reflection at Si surface, which is an important limitation in optoelectronic devices nowadays.

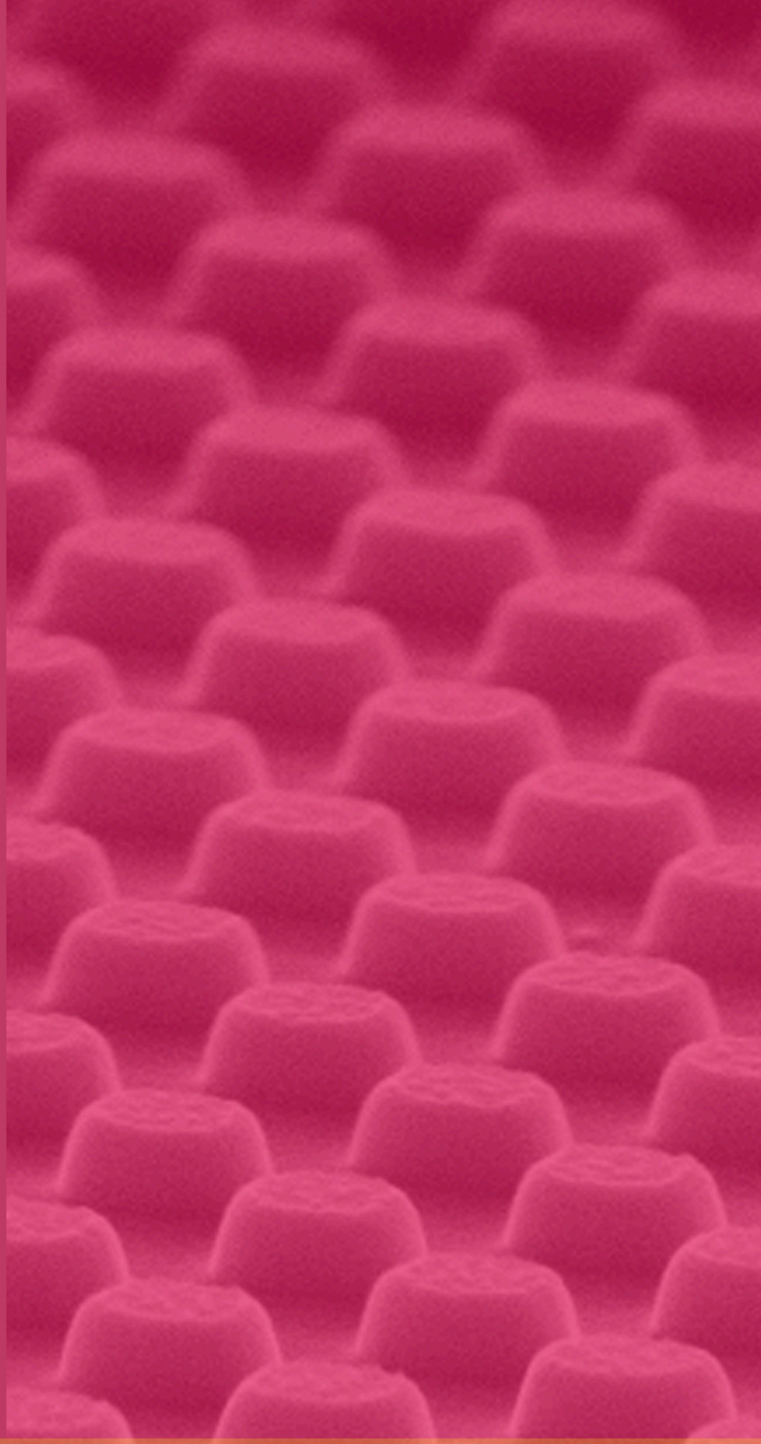

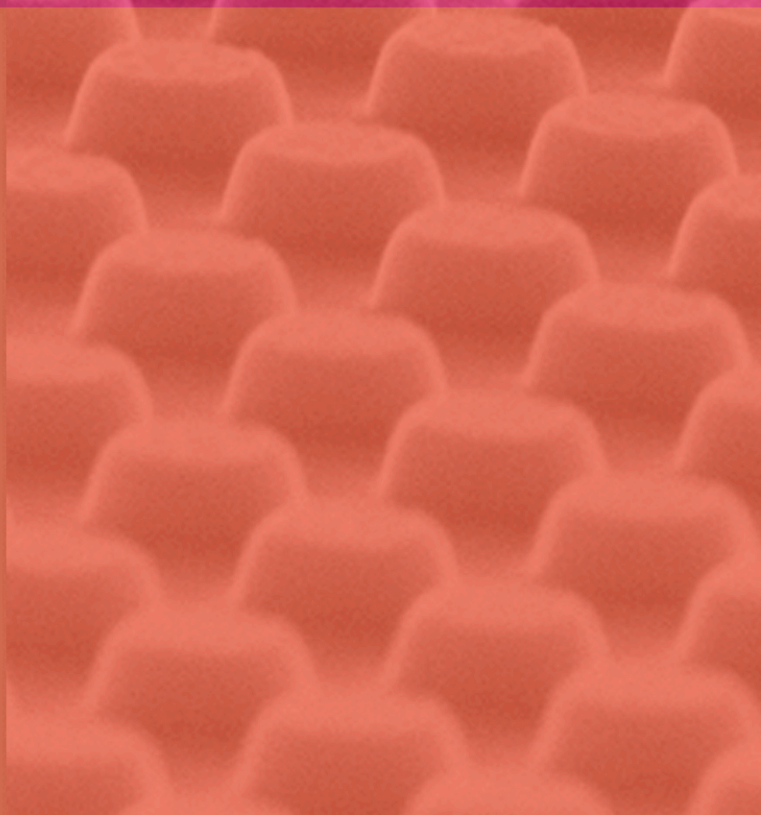

upna Universidad Pública de Navarra Nafarroako Unibertsitate Publikoa